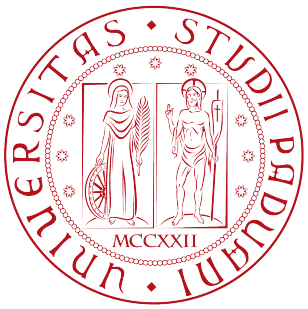

Università degli Studi di Padova

Dipartimento di Ingegneria Industriale

Master Degree in Aerospace Engineering

Preliminary design of a nitromethane MEMS thruster

Author:

Stefano Venturini
1234053

Supervisor:

Prof. Francesco Barato

Academic Year 2021/2022

Ringraziamenti

Un primo e profondo ringraziamento va al professor Barato per la sua continua disponibilità, il suo grande aiuto e la sua pazienza. Senza di lui, realizzare questa tesi non sarebbe stato possibile.

A Fede, Luca, Biondi e Marco non devo solo un grazie, ma proprio tutta la laurea (probabilmente due lauree). Non penso di riuscire ad esprimere a parole quanto questi anni insieme siano stati importanti, e come senza il loro aiuto, dagli appunti al supporto, questo traguardo non sarebbe stato raggiunto. Da ultimo del gruppo ad aver ottenuto la laurea magistrale dico solo: beviamo a noi e, soprattutto, a voi.

Questo traguardo è dedicato anche ai miei genitori e a mio fratello, che non hanno mai smesso di aiutarmi in ogni momento. In un modo o nell'altro, da vicino e da lontano, il loro affetto e supporto è stato sempre presente, e per questo non li ringrazierò mai abbastanza.

Last but not least, Giulia. Mi sopporta da più di due anni e non è mai passato un giorno senza che io non sentissi il suo sostegno. Anche in questo caso le parole scritte non bastano, ma questo risultato è anche merito suo: grazie di tutto, sempre.

Abstract

The advent of a new generation of miniaturized spacecraft with masses in the range of 1-100 kg, commonly referred as 'nano/microsats', led to the need of developing new micro-propulsion concepts. These micro-propulsion systems must be able to satisfy reduced thrust and impulse requirements for purposes of spacecraft attitude control and maneuvering, while also meet the stringent constraints on size, mass, power consumption and costs.

In this work is proposed a preliminary design of a MEMS thruster operating with nitromethane as mono-propellant, capable of delivering a 0.1 N thrust with a 25 bar operative pressure. Microelectromechanical systems (MEMS) techniques offer great potential in satisfying the mission requirements for micro and nano satellites.

The present work features also an overview on microelectromechanical system technology and its characteristics, with the presentation of various examples of devices and thrusters developed for space and terrestrial applications. Following a panoramic on various propellants considered, an introduction on the propellant chosen for the project (i.e., nitromethane) is discussed.

Finally, this paper submits the equations used and the considerations made to achieve the preliminary design of the thruster, the results, 3-D models and the technical drawings.

Sommario

L'avvento di una nuova generazione di satelliti miniaturizzati con masse nel range di 1-100 kg, comunemente chiamati nano/micro-satelliti, ha portato alla necessità di sviluppare nuovi concetti sulla micro-propulsione. Questi sistemi di micro-propulsione devono essere contemporaneamente in grado di soddisfare la richiesta di spinte e impulsi di bassa intensità finalizzati al controllo d'assetto e delle manovre dei suddetti satelliti, e di incontrare gli stringenti vincoli sulla dimensione, la massa, il consumo di potenza e i costi.
In questo lavoro viene proposto un design preliminare di un sistema propulsivo MEMS operante con nitrometano come monopropellente, in grado di erogare una spinta di 0.1 N con una pressione operativa di 25 bar. I sistemi micro-elettro-meccanici offrono un gran potenziale nel soddisfare i requisiti di missione di micro/nano-satelliti.
Il presente lavoro contiene inoltre una panoramica sulla tecnologia dei sistemi micro-elettro-meccanici e le loro caratteristiche, con la presentazione di vari esempi di dispositivi ad uso spaziale e terrestre. Dopo una panoramica sui vari propellenti considerati, viene introdotto il propellente scelto per questo progetto, vale a dire il nitrometano.
Infine, sono presenti le equazioni usate e le considerazioni fatte per ottenere il design preliminare del propulsore, i risultati, i modelli 3-D e i disegni tecnici.

Contents

List of Tables

List of Figures

1. MEMS: an overview

Micro Electromechanical System, or MEMS, is a process technology used to create integrated devices or systems that combine mechanical, electrical, and other (optical, thermal, magnetic, fluidic etc.) elements. They are fabricated using the techniques of microfabrication, like integrated circuit batch processing techniques, and their size can range from a few micrometers to millimeters. These systems can sense, control, and operate on the micro scale, generating effects on the macro scale.

In its widest terms, MEMS consist of mechanical microstructures, microsensors, microactuators and microelectronics, all onto the same silicon chip. Like its counterparts in the macroscale, microsensors detect changes in the environment through the measurement of optical, thermal, magnetic, electromagnetic, or chemical informations. Then, microelectronics process this information and the micro-actuators produce a change in the system's environment.

Even though MEMS is commonly associated with microscopic silicon components, MEMS is not just about the miniaturization of mechanical systems or the use of silicon as primary material but is a manufacturing technology. Its main aim is to design and create complex mechanical devices and systems combined with their integrated electronics using microfabrication techniques.[1][2]

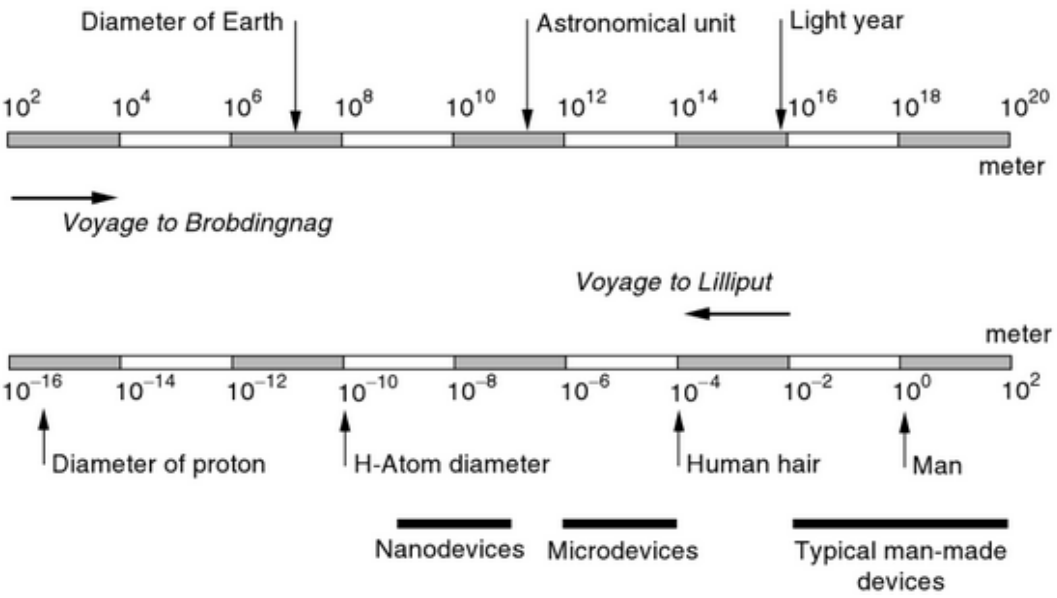

Figure 1: Scale of micro devices

MEMS has several advantages, for example [3]:

- MEMS technology is interdisciplinary. Thanks to its diversity of applications is possible to create an unparalled range of devices and synergies across multiple fields.
- With MEMS technology and batch fabrication techniques is possible to achieve high performances and reliability, that lead to advantages like small size, light weight and low cost.
- MEMS provides the basis for manufacturing products that can not be made by other methods. Scaling effects at microscopic levels can be leveraged to achieve designs and dynamic mechanisms otherwise not possible at macro-scale.
- In MEMS, it's easier to alter the part of a device as compared to its macro counterparts

However, there are also disadvantages, like:

- MEMS technology is very expensive during the research and development stage for new designs, and also in the upfront setup cost for fabrication cleanrooms and foundry facilities.
- MEMS are not suitable for niche applications because of the high unit costs of fabrication and assembly for low quantities.
- High costs also for the equipment used to characterize the quality and the performances of the systems.

1.1 Materials in MEMS

A deep understanding of the MEMS technology requires a knowledge of the materials used in the process and that compose the devices. Since the fabrication of MEMS systems depends on how sacrificial, structural and masking materials are combined, for design considerations are crucial the knowledge of structural, thermal, etc. properties, and the understanding of issues related to etch selectivity, adhesion, microstructure. MEMS fabrication technology often utilizes a collection of material to produce a device, so it is important not only the properties of the single material, but also how they interact with each other. In this section is presented a selection of materials commonly used in MEMS fabrication, and their properties. [4][5][6]

1.1.1 Single-crystal Silicon

Si is the most widely known semiconductor material used in these days and one of the most abundant elements on Earth. Single-crystal dislocation-free silicon is used for more than 90 percent of semiconductor device and is also used for half of the silicon in solar cells. Single-crystal Si is monolithic but not isotropic, so its properties are different in different crystallographic directions. One method to manufacture single-crystalline silicon is by forming mono-crystalline silicon in a quartz crucible. This method is known as Czochralski growth, and it involves placing a seed crystal into a molten silicon bath. The atoms of silicon in the silicon melt attach to the seed crystal. The silicon melt is then drawn upward from the crucible, forming a boule. Once the boule has grown to the required size, it is cut [7]. For semiconductor device, the crystals are sawed into round, flat disks called "wafer" for later device processing, an example is in figure 2 [8]

For MEMS applications, this material is used for varying key functions. Single-crystal Si is maybe the most versatile material for bulk micromachining, thanks to the availability of anisotropic etches and etch-mask materials. In the surface micromachining process, this material is used as mechanical base on which the system structure is fabricated. Single-crystal Si is also the main electronic material from which the IC devices are fabricated, in Si-based integrated MEMS.

Single-crystal Si has a diamond (cubic) crystal structure, with an electronic band gap of 1.1 eV. It can be doped to alter its conductivity with, for example, Phosphorus (P), in case of n-type Si, or Boron (B), for p-type Si. Its Young's module is comparable with steel, being 190 GPa (in the <111> direction), and it is a brittle material. Its Poisson's Ratio varies from 0.22 to 0.28, and its thermal conductivity is 149 W/m°C.

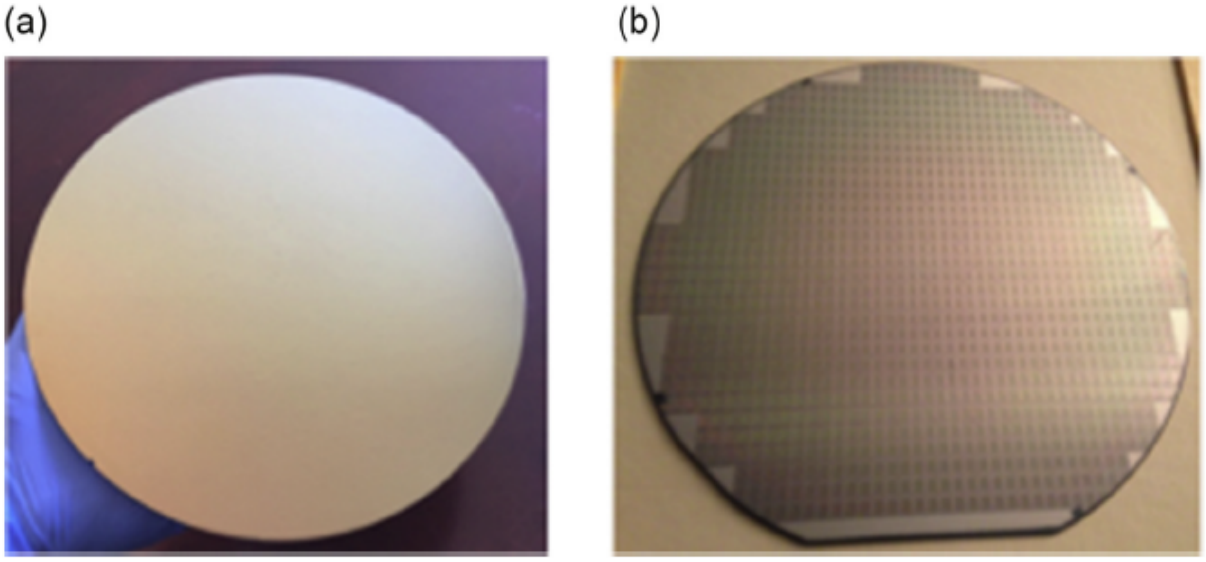

Figure 2: (a) finished polished wafer, (b) computer chips in wafer

1.1.2 Polysilicon

Polysilicon is the most widely used structural material for surface micromachined MEMS. Is often used in form of thin films typically fabricated by low-pressure chemical vapor deposition (LPCVD) using thermal decomposition of silane SiH_4. The mechanical properties of polysilicon are strongly influenced by its microstructure, which is dependent on the deposition conditions. For typical LPCVD processes, the amorphous-to-polycrystalline transition temperature is about 570 °C. Below that temperature the films display fine (circa 0.1 micrometers diameter) ellipsoidal-shaped grains. As the deposition temperature increase, the grain structure changes significantly (figure 3 and 4). During the fabrication of micromechanical device, polysilicon films go under some high-temperature steps after deposition, which they can cause recrystallization of the grains, that can lead to an increase of the size of the grains. The polysilicon can therefore increase its surface roughness. To deal with this problem, can be used chemical-mechanical polishing process.

Process like LPCVD produces films with high residual stresses, ad residual stress gradients through the film thickness, both of which can be harmful to MEMS device. Near-zero stress polysilicon can be achieved by high-temperature annealing in inert atmospheres. Another technique is the CVD at very high deposition temperatures (>1000 °C), but high deposition temperatures lead to an increase of surface roughness. A solution is the process involving multiple layers of polysilicon deposited at temperatures below 615 °C[9].

Polysilicon is expected to show different elastic properties due to fact that its mi-

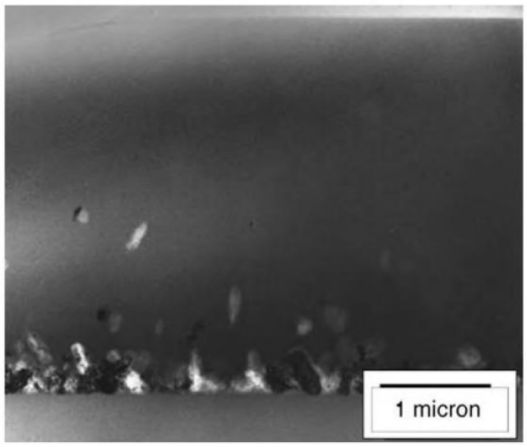

Figure 3: Amorphous Si deposited at 570°C

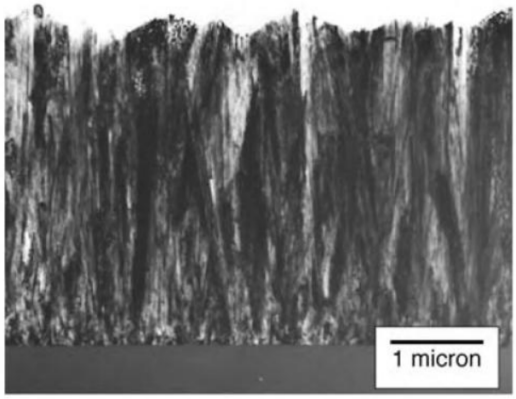

Figure 4: Polysilicon deposited at 620 °C

crostructure varies with the deposition conditions. Comparing various measurements [10], is found that the Young's moduli range from 130 GPa to 176 GPa for undoped and doped samples, with uncertainties of the order of 10 GPa. The Poisson's ratio is found to be 0.20 ± 0.03 for in-plane deformation of columnar films with <110> textures. Comparing several investigations [11], is found that the tensile strengths range from 0.7 GPa to 3.4 GPa. The fracture toughness[12] is 1.4 MPa$m^{1/2}$ for a notch radius of 1.0 μm, and 1.9-4.5 MPa$m^{1/2}$ for a notch radius of 0.23 micrometers. Thermal conductivity and coefficient of thermal expansion are obtained to be (29.96 ± 0.92) Wm/K and (2.65 ± 0.03)x10^{-6} K^{-1}, respectively, with temperature ranging from 300-400 K.

In conclusion, the microstructure and residual stress of polysilicon thin films deposited by LPCVD are strongly dependent on the deposition and subsequent conditions. Young's module and Poisson's ratio are relatively independent of deposition conditions or microstructure. The tensile and bend strengths are dependent on surface morphology and are affected by processing conditions

1.1.3 Silicon Dioxide

Silicon dioxide (SiO_2) can be grown thermally on Si substrates as well as deposited using a variety of process to satisfy a wide range of different requirements. Is a natural compound of oxygen and silicon, found mostly in the sand, and it is also known as Silica. There are various forms of Silica, they are all identical in chemical composition but show different atom arrangements. SiO_2 can be used as a blocking material for ion implantation or diffusion of many unwanted impurities. Its interface with silicon has relatively few mechanical and electrical defects. Has a high dielectric strength (10e7 V/cm) and a relatively wide band gap (8.9 eV), making it an excellent insulator. Has a high temperature stability up

to 1600 °C.

It is used commonly in polysilicon surface micromachining as sacrificial layer because is dissolved easily with etchants that don't attack polysilicon. In a rarer way, it can be used as etch mask for dry etching of polysilicon films, as it is resistant to many chemicals used during etching. Its growth and deposition in polysilicon surface micromachining is commonly made by thermal oxidation and LPCVD. Thermal oxidation of Si is performed at high temperatures (900-1000 °C) in the present of oxygen and steam and because the oxide growth rate decreases with increasing film thickness, the maximum film thickness obtainable is 2 μm. For MEMS applications, is possible to deposit SiO_2 films by an LPCVD process called low-temperature oxidation (LTO), which provides a deposition at lower temperatures of thermal oxidation (circa 425-450 °C), and with a higher etch rate than thermal oxides. During the LPCVD process is also possible to include dopant gases to dope the SiO_2 films. A process to deposit low-stress, very thick (10-20 μm) SiO_2 films was documented for MEMS applications, called plasma-enhanced chemical vapor deposition (PECVD)[13].

Silica has three primary crystalline varieties: quartz, tridymite and cristobalite. Quartz can be used by MEMS fabricators because is electrically insulating, can be bulk micromachined using anisotropic ethcants and is available as high-quality large-area wafers.

1.1.4 Silicon Nitride

In MEMS, Silicon nitride (Si_3N_4) is largely used as surface passivation, etch masking, electrical isolation and mechanical material. Silicon nitride based ceramics are polycrystalline, composite materials, which consist of minimum two phases: silicon nitride grains and grain boundary phases. The silicon nitride grains are single crystals with three possible crystallographic modifications, while the grain boundary phases are either amorphous or partially crystalline. Because of this, the properties of Si_3N_4 based ceramics depend on the intrinsic properties of the single crystals and the size, orientation, and volume fractions of the grains. So, its properties can be improved by tailoring the microstructure. Two commonly deposition methods for Si_3N_4 are LPCVD and PECVD. Even though PECVD in micromachined applications can be limited by the high etch rate, it can offers the potential to deposit nearly stress-free films, very useful for MEMS applications. On the contrary LPCVD Si_3N_4 is used in many Si bulk, surface micromachined applications, and as an insulating layer to isolate device structures. Typical deposition temperatures and pressure range between 700 and 900 °C and 200 to 500 mtorr.

Hardness of silicon nitride depends on the phase of its transformation. Generally, the hardness of beta-Si_3N_4 is circa 12 GPa for a material with coarse grained microstructure and/or high additive content, and is circa 20 GPa for the material with a fine grained microstructure and/or low additive content[14]. The flexural strength of fully dense Si_3N_4 range from 800 to 1400 MPa, depending on the presence of processing defects. The strength decreases as the grain size increases, for example Si_3N_4 with a fine, submicrometer grained microstructure reaches a fracture strength of more than 1000 MPa. By developing the textured Si_3N_4, the strength can be maximized in one direction (usually the perpendicular direction to the grain alignment). The fracture toughness of Si_3N_4 depends on the composition of the grain boundary phases and on the size and shape of the grains. Si_3N_4 with a microstructure having a high volume fraction of grains (with aspect ratio >4) have a fracture toughness of 8 MPa$m^{0.5}$. Like the strength of silicon nitride, is it possible to improve the fracture toughness by the texturing of the microstructure, reaching a value of circa 14 MPa$m^{0.5}$. Regarding of the thermal conductivity, experimental measuring show values around 60-90 W/mK for sintered polycrystalline Si_3N_4.

1.1.5 Silicon Carbide

Silicon carbide (SiC) is a combination of silicon and carbide in a crystalline structure. SiO_2 is a good semiconductor with potential for use in high-temperature and high-power electronics. It's polymorphic, so it exists in multiple crystalline structures, which means that its properties change. It can take on many different forms, for example individual grains can be sintered together to made strong ceramics, fiber of SiC can be added to a polymer matrix to form a composite material, or individual crystals can be used as semiconductor. Polycrystalline SiC is a very versatile material for MEMS: first, it can be deposited on various substrate types, including polysilicon (which is a common surface micromachined material), SiO_2 and Si_3N_4. Secondly, it can be deposited using a wide set of process like LPCVD, APCVD and PECVD. Its deposition requires a substrate temperature ranging between 500 to 1200 °C. Its microstructure depends on the temperature and the substrate. Commonly, the grain size increases with increasing temperature, but for amorphous substrates like Si_3N_4 and SiO_2, poly-SiC films tend to be randomly oriented with equiaxed grains, with larger grains deposited on SiO_2. For oriented substrates such as polysilicon, the texture of the poly-SiC film matches that of the substrate as a result of grain-to-grain epitaxy[15], so it is possible to select the proper substrate and deposition conditions in order to achieve the desired performances.

Conventional wet chemical techniques are not effective on SiC because of its high chemical durability, that makes hard its direct bulk micromachining. This problem af-

fects the geometric complexity of the fabricated devices that is possible to achieve. A solution to fabricate thick, three-dimensional, high-aspect-ratio structure made of SiC was developed[16], which use molds fabricated in Si substrate using DRIE (deep reactive ion etching), and a combination of process to, in the end, fabricate a SiC structure that could otherwise not be fabricated with other technologies.

Regarding its physical properties, SiC has a Young's Modulus that range from 350 to 650 GPa, and a Poisson's ratio of 0.21. Its thermal conductivity and its bandgap ranges from 3.3 to 4.9 W/cmK and from 2.36 to 3.26 eV respectively. Its melting point is 3100 K, which makes it a good material for high-temperature applications.

1.1.6 Metals

In MEMS applications, metals are used in a variety of ways, like hard etch masks, thin film conducting interconnects and structural elements. The most commonly deposition processes for metals are CVD, evaporation, sputtering and electroplating. The most used metal in MEMS is Aluminum (Al), which can be used with other materials like polymers thanks to its low temperature of deposition. Al is commonly used as structural layer, but it can be used also as sacrificial layer. One effective combination as structural and sacrificial materials is the polymide/aluminum[17]. This combination offers good properties thanks to polymide being more compliant than polysilicon and capable of withstand large strains before fracture. Furthermore, both materials can be processed at low temperatures ($<$400°C), and can be used for the fabrication of ICs on the wafer. Another combination of structural and sacrificial layers is the Tungsten/silicon dioxide[18]. It is used also a combination of nickel and copper as structural layers, and polymide or other metals as sacrificial. One of the most important behavior of metals used in MEMS applications is the shape-memory effect, which can be used as an actuation mechanism. This behavior relies on the reversible transformation form a ductile martensite phase to a stiff austenite phase with the application of heat.

1.2 Routes of Fabrication

The fabrication of MEMS devices share some fabrication techniques and tools with IC (integrated circuits) fabrication. However, MEMS has improved some of these processes, and added new steps.
This section provides an explanation about the three major routes of fabrication actually on the market:

- Bulk Micromachining
- Surface Micromachining
- High-aspect Ratio Micromachining

1.2.1 Bulk Micromachining

Bulk micromachining is a process that enable the fabrication of small structures for MEMS devices, using various materials. It's a subtractive process based on wet anisotropic etching or dry etching method to form micro mechanical structures. For wet etching, the materials commonly used are silicon and quartz, while dry etching is used with silicon, metals, plastic, and ceramics.

Wet etching

Wet etching uses chemical etchants (isotropic or anisotropic, see figure 5) to remove material from, typically, a silicon wafer. Isotropic means that the material is etched at the same rate in every directions, so it removes material under the mask at the same rate as they etch through the material. This technique is called undercutting[1]. The most commonly used etch in isotropic wet etching for silicon is HNA, which is a mixture of hydrofluoric acird (HF), nitric acid (HNO_3), and acetic acid (CH_3COOH). The overall reaction is[19]:

$$18HF + 4HNO_3 + 3Si \longrightarrow 3H_2SiF_6 + 4NO_{(g)} + 8H_2O \tag{1.1}$$

When it is used at room temperature, the etch rate achievable is circa 4-20 μm/min, which is increasable with agitation 5. It is possible to dope some regions to slow down the HNA etch by circa 150 times.

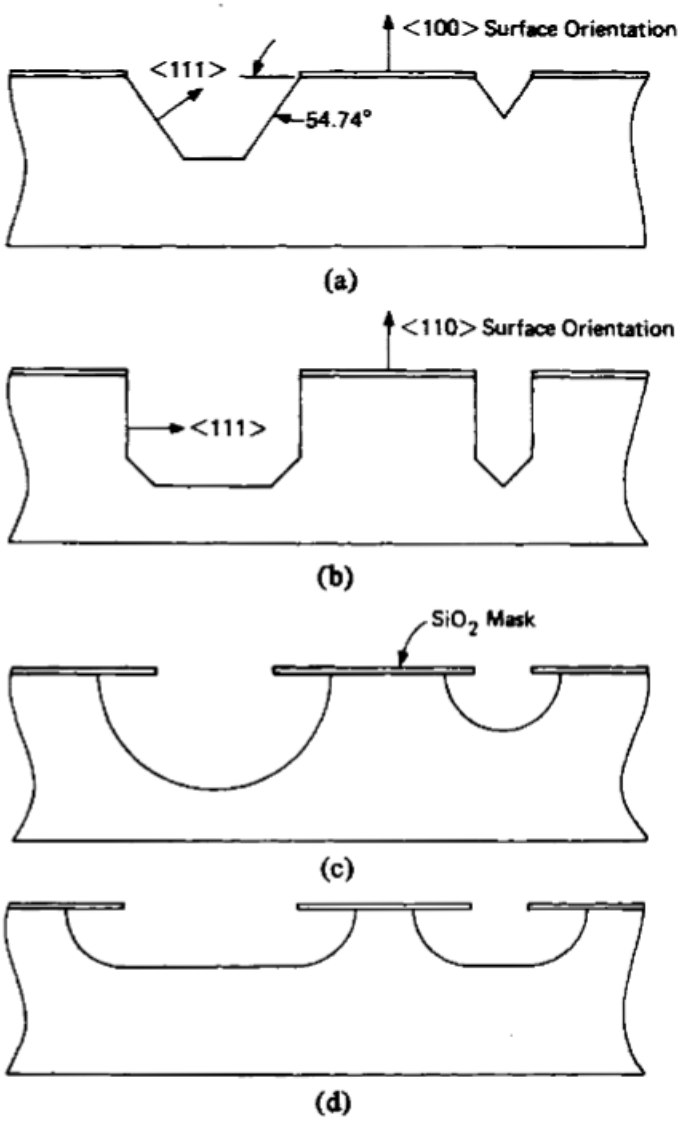

Figure 5: (a) Anisotropic etching. (b) Anisotropic etching. (c) Isotropic etching with agitation. (d) Isotropic etching without agitation[20]

Anisotropic means that the material is etched faster in one direction than the other. The commonly used etchant for anisotropic etching is Potassium hydroxide (KOH). The crystal orientation of the substrate or wafer influence the structure formed in the material. One of the main feature of the anisotropic etch in silicon is that the <111> plane is attacked at slower rate than all other crystallographic planes. This behavior could be explained by the higher density of atoms per square centimeter in the <111> silicon surfaces. In figure 5 are shown some examples of anisotropic etching in <100> and <110> silicon. It is possible to affect and even stop the etch rate of KOH by doping the substrate, for example by doping with Boron, and can be useful for etching only the non-doped regions, leaving the doped regions unattacked.

Dry Etching

Dry etching is achievable by using reactive vapor/gases at, usually, high temperatures. One commonly used form of dry etching for MEMS applications is Reactive Ion Etching (RIE) which don't need complex equipment. RIE uses energy in form of radio frequency power to activate the chemical reaction. This process is based on energetic ions that are accelerated towards the material within a plasma phase supplying the additional energy that is needed for the reaction. With RIE is possible to achieve an etch at lower temperatures (150-200 °C) than usual (>1000 °C) and this process is not limited by the crystal planes in the material etched, so it is possible to form shapes with vertical walls.

Dry etching is achievable by using reactive vapor/gases at, usually, high temperatures. One commonly used form of dry etching for MEMS applications is Reactive Ion Etching (RIE) which don't need complex equipment. RIE uses energy in form of radio frequency power to activate the chemical reaction. This process is based on energetic ions that are accelerated towards the material within a plasma phase supplying the additional energy that is needed for the reaction. With RIE is possible to achieve an etch at lower temperatures (150-200 °C) than usual (>1000 °C) and this process is not limited by the crystal planes in the material etched, so it is possible to form shapes with vertical walls.

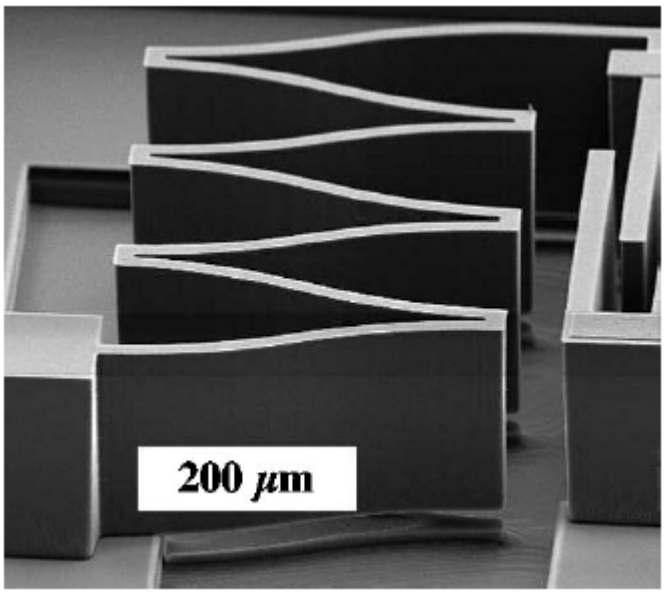

Figure 6: Microflexure created by vertical etching through a wafer with DRIE

Another form of dry etching is Deep Reactive Ion Etching (DRIE), which provides fast, high-aspect-ratio silicon micromachining with a good profile control and precise feature definition. It is possible to achieve deep cavity and trench etches with clean sidewalls.

DRIE involves a process of high-density plasma etching similar to RIE, and deposition of protective polymer to obtain great aspect-ratio.6[21]

1.2.2 Surface Micromachining

Surface micromachining [1][22] is a fabrication technique for MEMS which consists of depositing and structuring a sequence of thin layers (usually 1-100 μm thick) on a silicon wafer. These layers can be structural layers or sacrificial layers. The main difference between surface micromachining and bulk micromachining is that the last one use the silicon substrate itself to form the device by etching technologies, while surface micromachining uses thin film layers deposited on a functional material. Another difference is that in bulk micromachining are often required some process steps from the backside of the wafer, while in surface micromachining all steps are performed on the front of the substrate. Commonly, in surface micromachining for MEMS applications the material used are polycrystalline silicon (or, in some specific applications, metal) as functional layer and silicon dioxide as sacrificial layer.

An example of surface micromachining process is illustrated in figure 7. Uppermost, a silicon dioxide layer is used as electrical insulator for a high conductive polysilicon. The polysilicon serves as buried wiring layer for the interconnection of the other layers. On the top, there is a silicon-based functional layer and a metal layer, that are deposited and structured individually. The most important step of process is the removal of the sacrificial layers without attacking the structural layers, in fact the success of the operation is based on the ability to free the structural elements from the sacrificial elements so that they can be activated. Common deposition techniques are low-pressure chemical vapor deposition (LPCVD) and plasma-enhanced chemical vapor deposition (PECVD). To metallize the electrical contact is used a technique called sputter deposition process. To define the lateral geometries of the wafer structure is used a process known as lithography. At the end of the process, is possible to patterned anisotropically the mechanical silicon element by DRIE. As last step, the structure is freed form the sacrificial layers by etching them.

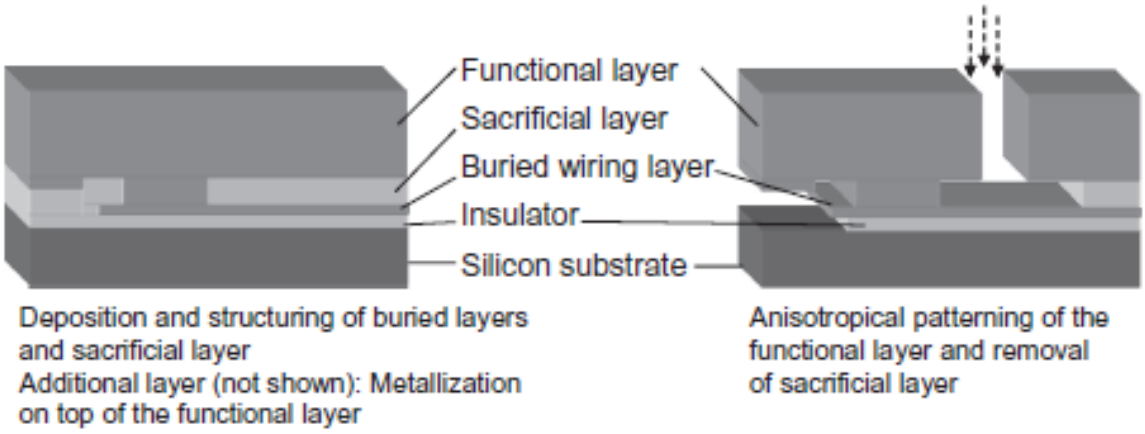

Figure 7: Schematic cross-section of the layer sequence[22]

Some advantages and disadvantages of surface micromachining are:

- Good dimensional control
- Good mechanical properties
- Less material loss
- Is expensive due to more fabrication steps involved
- Difficult to implement to large structures

Fusion Bonding

Fusion bonding is a process that allows to fabricate complex and large MEMS structures by combining two or more patterned wafer [23]. The process can be used to create membranes of thickness varying from few to several micrometers, or complicated three-dimensional structures, multilayered device structures (e.g., micropumps), high aspect ratio structures. It is based on the creation of atomic bonds between the layers, directly or through a thin film of material (e.g., silicon dioxide). Commonly is realized by mating a wafer pair at room temperature and then annealing at temperatures between 700-1100 °C. The areas that can cause major concerns are the non-contacting areas. These voids can be caused by a lot of things, like organic residues, surface defects or inadequate mating. To avoid this problem, both surfaces of the wafers must be smooth and clean, so wafer surface inspection and pretreatment are necessary. The structure resulting after the bonding has very low residual stress and a high mechanical strength. The main disadvantage is the high process temperatures, which require preprocessed wafers.

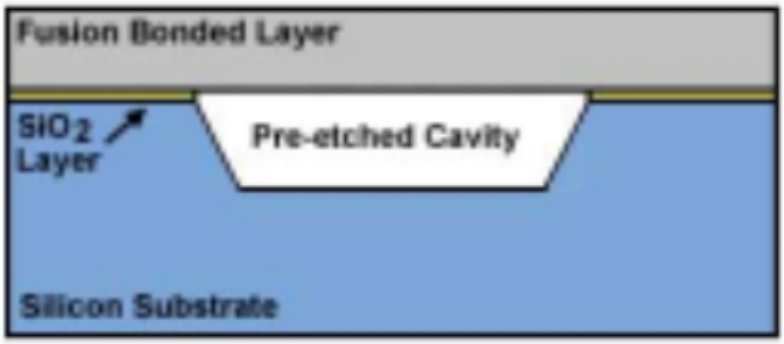

Figure 8: Example of fusion bonding[1]

1.2.3 High-aspect Ratio Micromachining

High-aspect ratio micromachining (HARM) is a process that allow to obtain structures with a larger vertical dimension compared to the lateral dimension. HARM processes are generally characterized by x-ray lithography and/or micromachining methods followed by injection moulding or embossing and by electroforming [1].

LIGA

LIGA is a german acronym for "Lithographie, galvanic und Abformung" (lithography, electroplating and moulding) and is used to manufacture microstructures by deep X-ray lithography [24]. LIGA process is based on the deposition of a relatively thick layer of a polymer sensitive to X-rays on top of a conductive substrate. After exposure through an appropriate X-ray mask, the exposed or the unexposed (positive or negative photoresist) are removed and metal layers are grown by electroplating in the spaces. Now that the unwanted areas of the polymer are removed, the metallic structure resulting can be used. LIGA can create very finely defined microstructures up to 1000 μm high. The main problem for LIGA is that an access to X-rays facility is needed. To avoid this problem, a new technology has been developed called SLIGA (Sacrificial LIGA) [25]. It consists in the replacement of the thick layer of polymer sensitive with polymide as the electroplating mould, thus enabling compatible conventional IC batch processing. SLIGA permits the production of MEMS with less manufacturing infrastructures in terms of facilities, investments and access to advanced materials and technology.

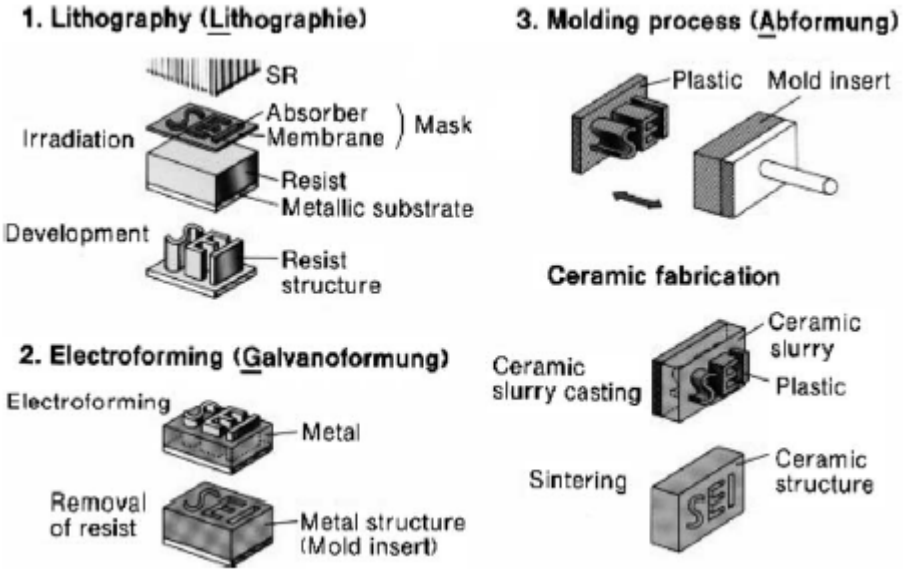

Figure 9: Schematic view of the LIGA process[24]

Laser Micromachining

Laser micromachining found little applications in MEMS because is can be not fast enough. Still, is possible to use it for, e.g., laser drilling, laser annealing and etching [1]. These processes require rapid heating, melting and evaporation of the material. Currently, laser micromachining is achieve using two technologies[26]:

- Direct laser writing (DLW), which use a solid state laser with a 2D galvanometer scan head (figure 10).
- Mask projection technique (MP), which use Excimer lasers and conventional fixed masks (figure 11).

The lasers system in micromachining commonly use pulsed beams with an average power below 1 kW.

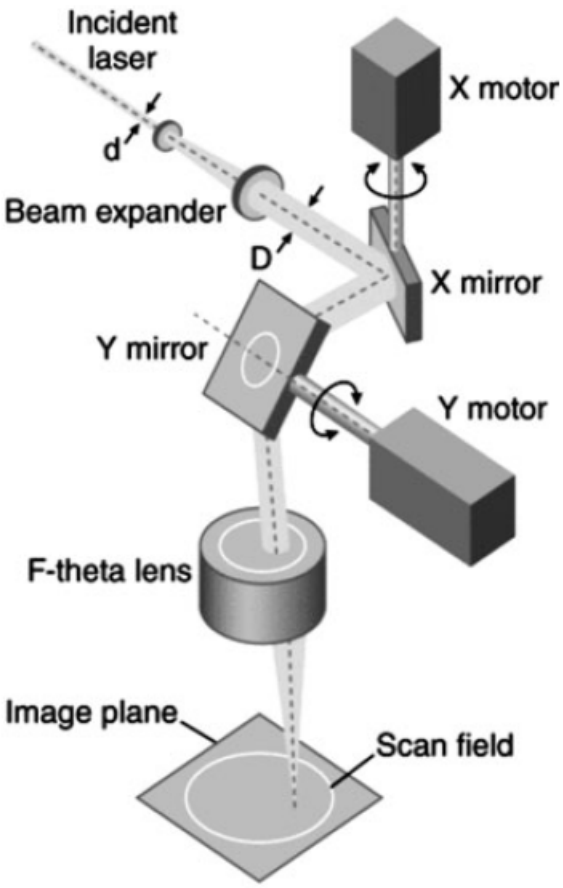

Figure 10: Direct laser writing method with scan-head

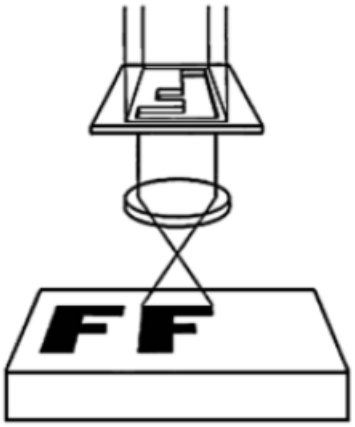

Figure 11: Mask projection technique

2. MEMS in Space

One of the growing interest in the space community is the reduction of size and weight in order to replace large satellites with smaller ones, and to reduce costs. This goal can be achieved thanks to MEMS devices, which are capable of substitute large components, and replace entire subsystems. Using MEMS technology not only can save mass and volume of single components, but it can also allow increased redundancy, reliability, performances, functionality, and reduced fabrication costs.
MEMS technology has a big interdisciplinary nature, so MEMS devices in space found a great number of uses, for example [27]:

- Inertial navigation
- Switches and capacitors
- Bio and microfluidics
- Pressure and various sensors
- Optical instrumentation, switching and communication
- Thermal control
- Micropropulsion

The advantages of MEMS technology for space applications does not stop with the benefits listed above, it can also enable new applications or missions. For example, micropropulsion can allow improved formation flights or precision control of small/medium satellites, that possess low masses and low power budget.[28] [29].

With MEMS fabrication technology it will also be possible to fabricate entire spacecraft on silicon wafers. These nanosatellites could be used to create a dense low Earth orbit constellation, or in local clusters for various communications and Earth-observation

missions. [30]

In this chapter, MEMS applications for space are presented and discussed divided into two different classes:

- Actuators and sensors (which include microvalves, micropumps, sensors etc.)
- Thrusters (which include micro combustion chambers, micronozzles etc.)

2.1 Actuators and sensors

Valves

The necessity of achieving precise control of fluid flow has brought the development of micromachined valves using MEMS technology. These devices found their applications in various areas, from biomedical and biochemical, to micro propulsion systems, the main interest of this chapter.

The first example of valve presented is a micro-valve array for fluid low control [31]. Flow rate through a microvalve array is different than the one through a single channel flow control valve, where is controlled by varying the size of a single channel. In an array, the flow rate scales linearly with the number of microvalves open. One big advantage of using an array is that is possible to achieve a precise flow rate through multiple simple low precision elements, instead of using a single complex high precision element. This difference allows to reduce costs and a simpler microfabrication.

In this array, every valve is an independently controlled actuator consisting of a diaphragm fixed along two side [32]. The diaphragm is placed over an inlet port, and it functions as a moving electrode, while the microvalve functions as a parallel plate electrostatic actuator. The silicon substrate is the ground electrode. If, between the substrate and the diaphragm, a voltage is applied, an electrostatic force develops causing the diaphragm to deflect towards the substrate. When the voltage increases, the diaphragm goes under electromechanical instability and collapses onto the substrate, closing the inlet port and reducing the flow. In figure 12 is presented a schematic design of the array.

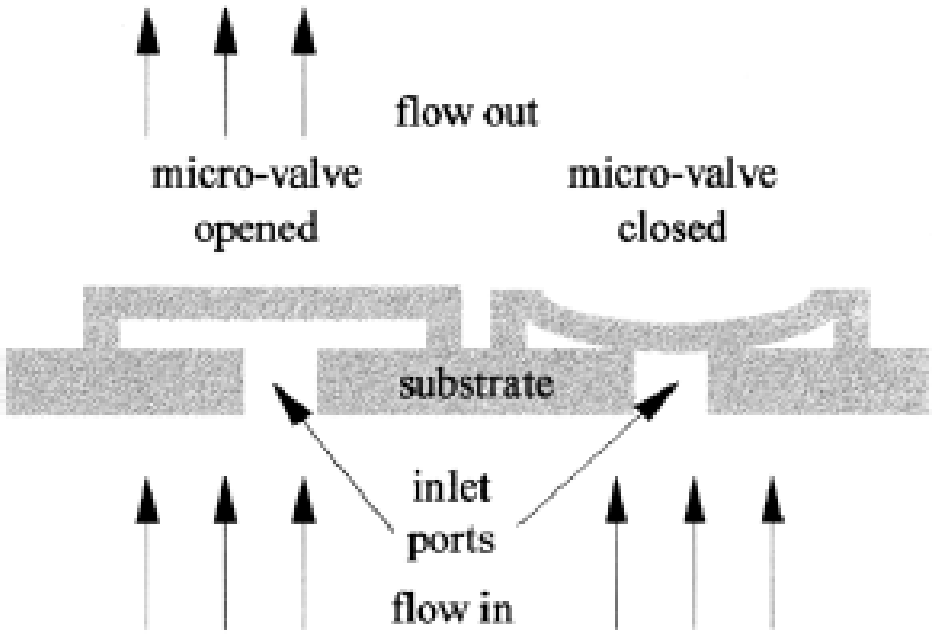

Figure 12: Schematic design of the microvalve array

The design from another perspective can be seen in figure 13. It presents a 5x5 array on a silicon wafer. All microvalves on the wafer are identical. The diaphragms are composed of a layer of 0.5 micrometers of silicon nitride between two 0.5 micrometers layers of polycrystalline silicon. The dimension of the gap between the microvalve diaphragm and substrate is a compromise between fluidic and electrostatic, because increasing the gap means increasing the flow rate achievable, but it requires larger closing voltages. The flow rate scales with the third power of the gap, while the closing voltage scales with the square root of the gap cubed [33][34]. There is a limit on the required voltage that makes electrostatic operation impossible, so it is not possible to increase the nominal gap beyond a certain value. In this example, the gap is 5 micrometers. While the microvalve is in function, the air flows across the inlet port and the gap to the outlet. There is found to be a pressure differential across the inlet port and the gap, so the dimension of the inlet port is chosen to ensure that the pressure differential across the port is smaller than one tenth of that across the gap. The final dimension of the port is 80 x 80 micrometers.

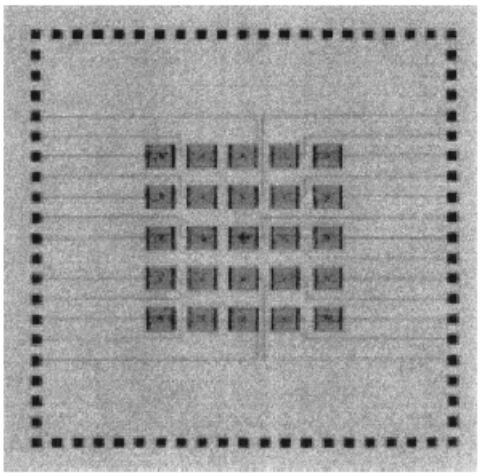

Figure 13: Microvalve array design showing the actuator array, wiring, and wire bonding pads

In regard to the fabrication, the entire system is composed of 7 layers: one 0.5 micron thick layer of silicon nitride for electrical insulation between the diaphragm and the substrate, one 0.5 micron thick layer of polycrystalline silicon for micro-valve sealing ring, one 5 micrometers thick layer of silicon dioxide for sacrificial layer, three 0.5 micron thick layers of polycrystalline silicon, silicon nitride and polycrystalline silicon for micro-valve diaphragm and wiring, and one last 0.5 micron thick layer of metal for bonding pads.

Another example of MEMS micro-valve presented is the one developed by JPL [35]. This device is supposed to meet the typical requirements for NASA deep space micro spacecraft propulsion, which are[36]:

- Leak rate: < 0.3 sec/h Helium
- Actuation speed: < 10 ms
- Inlet pressure: 0 - 400 psia
- Shock: 3000 G at 10 kHz
- Vibration: 31.5 G_{rms} for 3 min
- Temperature: -120 °C to 200 °C
- Radiation: 50 krad/year
- Particulates: 1.0 micron

A schematic cross-section view of the valve is shown in figure 14. The valve is closed in normal position. The piezoelectric stack is contracted during process, in order to apply a great sealing force on the openings. The device has a square footprint of 1.6 cm and a height of 3mm. The valve is composed of three parts: the seat, the diaphragm, and the actuator.

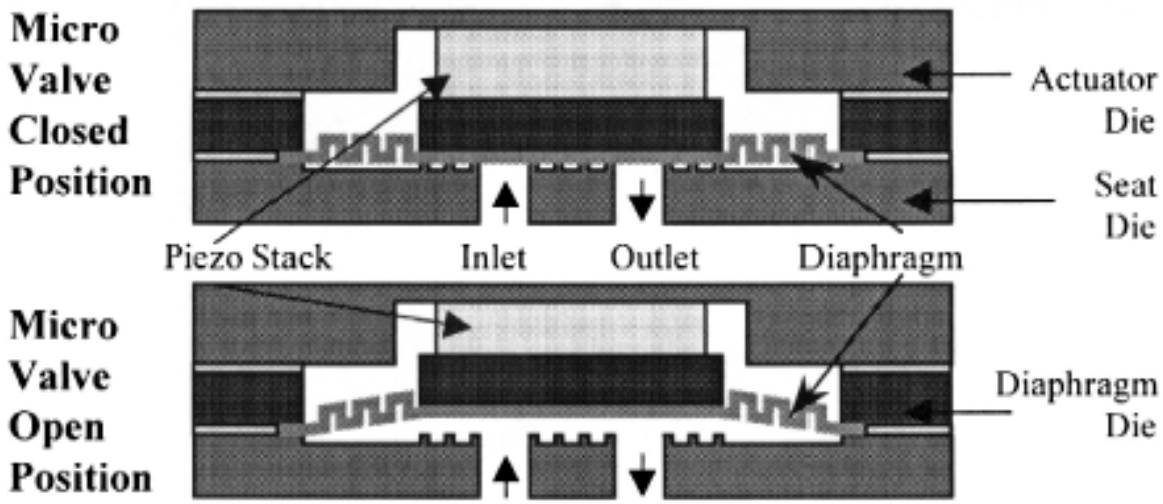

Figure 14: Cross section of the device in close and open position

The seat is the base of the valve and is the part that interface with the rest of the micro-fluidic system. It also contains the inlet, the outlet, and a set of seal rings around the openings. To achieve the requested performances, a larger sealing area between the inlet and the outlet is been designed. Moreover, the sealing force is applied to both the inlet and the outlet, and there is a large sealing area around the openings, to prevent leaks. The seat is defined "hard" because the sealing surfaces will not deform thanks to their high elastic moduli. To achieve immunity to particulates, the sealing area has a unique geometry based on a series of closely spaced 20 micrometers high rings, that expand outward from the inlet and the outlet. An advantage of this configuration is the ability to withstand small particles that may be in the flow. Unfortunately, some particules may be embedded into the sealing surface, so it is important that the surfaces of the rings are coated with a hard, resistant material (e.g., silicon nitride or diamond).

The diaphragm is in the central section of the valve, and it is circular, corrugated and has a circular boss in the center, so it can cover the openings in the seat. The actuator is a laminated piezoelectric disk. A laminated piezoelectric stack is one where electrodes are interlaced with thin (100 microns) layers of piezoelectric material, so it is possible to apply a small voltage to many layers and achieve the same deflection than a large voltage

applied to one thicker piezoelectric layer.

Some of the results obtained by testing the valve are presented in figure 15

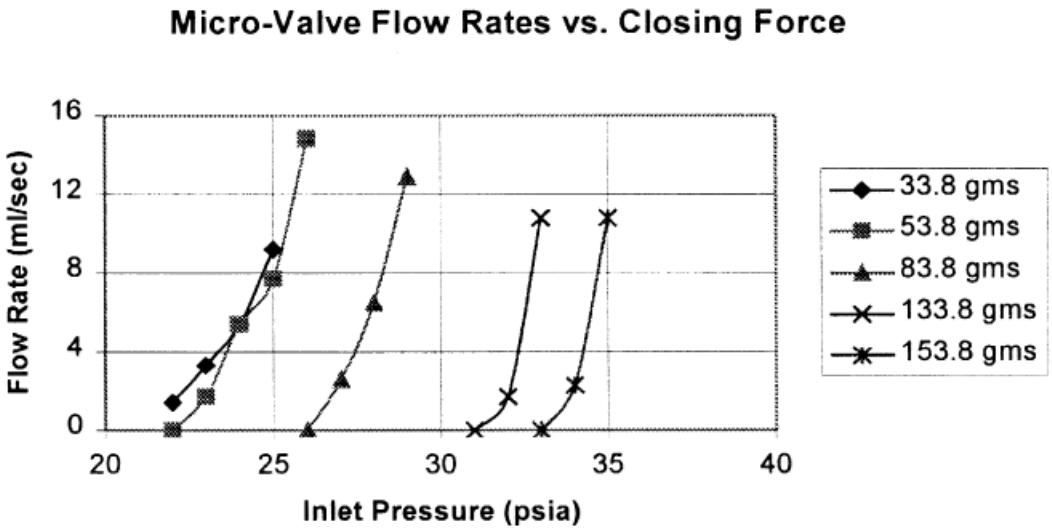

Figure 15: Flow rates vs. closing force in the microvalve developed by JPL

The last example reported of a microvalve is the one developed by Collier, Wroblewski and Bifano [37]. They developed a system of 61 synchronized microvalves operating in parallel. In figure 16 is shown a cross-sectional view of a single valve.

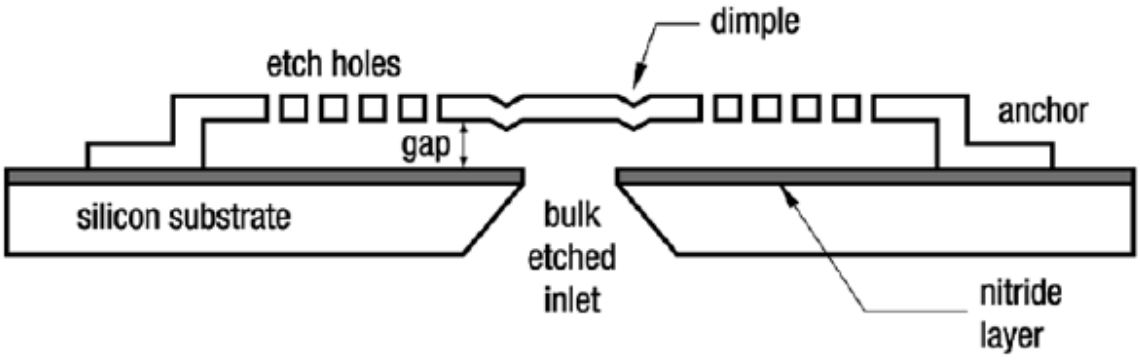

Figure 16: Microvalve cross section

The device is composed of a 300 – 400 micron polysilicon plate anchored on a hole in a silicon substrate. Between the plate and the substrate there is a 2 micron gap. The gas flows through the substrate inlet (250 microns square) and exits through the side of the valve (perpendicular to the figure 16) and through the etch holes. The closing of the valve is achieved by electrostatic attraction, which means that the plate deflects down when a voltage is applied, sealing the hole. The voltage is delivered by an external driver

circuitry, which is linked to the valve plate through a polysilicon routing wire. To avoid short circuit, a layer of silicon nitride is placed between the plate and the substrate, preventing direct contact. The gap is really small, so there is a risk that some particulate could block the valves. To avoid this problem, is possible to use a filter upstream of the valves.

In figure 17 is shown a layout of the 61 valve array. The array is placed on a 1 cm^2 chip. For control is used a pulsewidth modulation (PWM) system, that involves actuating the valves with a high frequency square wave and varying the duty cycle to regulate flow rate [37]. The combination of PWM and microvalves with a fast actuation times (order of 10 microseconds) for close loop control achieves a high dynamic range and great precision.

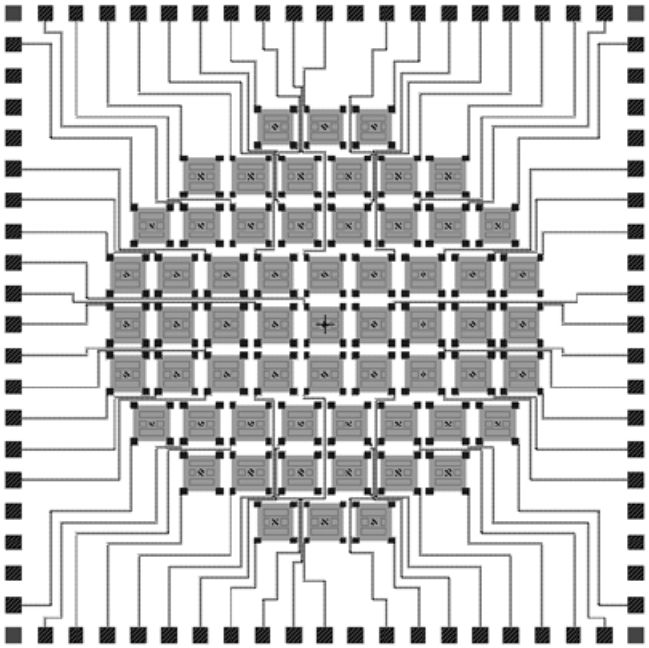

Figure 17: Layout of 61-Valve array

Pressure sensors

The first pressure sensor presented is a MEMS based capacitive pressure sensor for harsh environment [38]. Its schematic design is illustrated in figure 18.

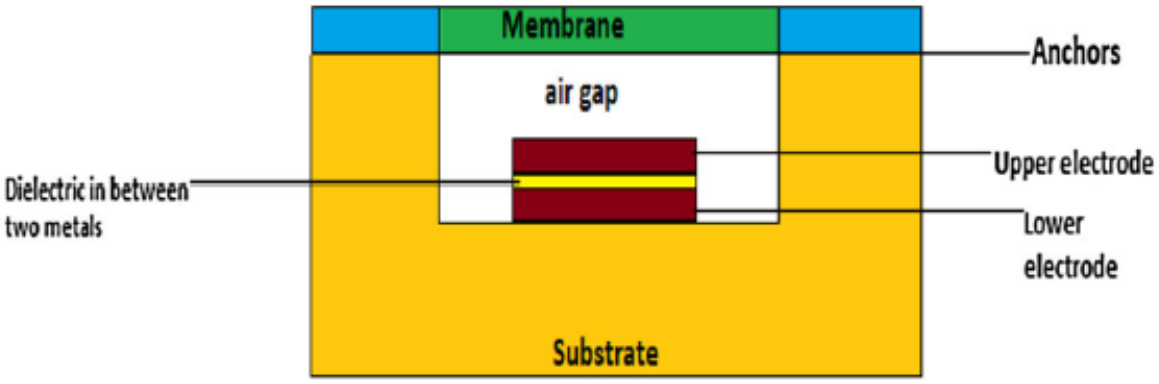

Figure 18: Cross-sectional view of the MIM pressure sensor

This sensor is a MIM type capacitive pressure sensor, where MIM stands for metal-insulator-metal. It consists in one substrate of silicon and, on top of that, four layers in circular shape, three of which are connected to one another, and the last one is placed with a gap over it. As we can see in figure 18, upper electrode and lower electrode, which are made of gold, are separated by a dielectric material.

When the air pressure is applied, the membrane will be diverted into the cavity, altering the capacitance. The capacitance decreases if the effective electrode area is lowered, and it's calculated dividing it in two parts: the first is measured between the two metal terminals, and it varies with the dielectric material properties and thickness; the second is measured between the upper electrode and the membrane. This MEMS pressure sensor has a dimension of 400 x 400 micrometers, and an air gap from 0.15 to 2 micrometers with pressure ranging from 200 to 1500 MPa.

Another pressure sensor presented is an ultra-thin MEMS capacitive pressure sensor, with a sensitivity better than 150 aF/Pa, and able to detect a change in pressure with a resolution of 0.025% in a pressure range of $\pm$ 3.5 kPa [39]. In figure 19 is illustrated the design of this capacitive sensor. The sensor has an overall dimension of 1.0 mm $\times$ 1.0 mm $\times$ 60 μm

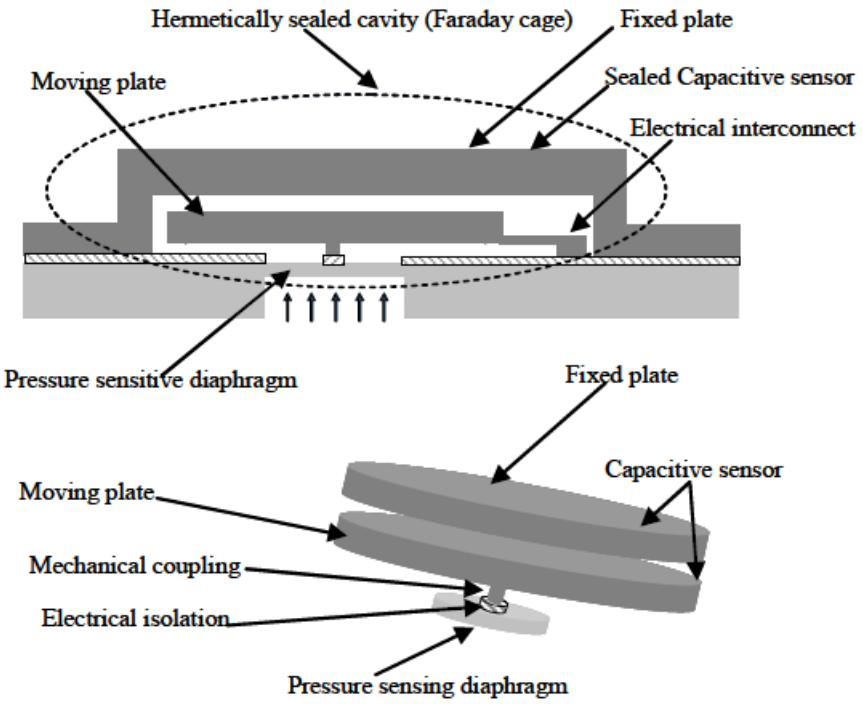

Figure 19: Schematic drawing of the ultra-thin MEMS capacitive pressure sensor

This capacitive sensor has a separate capacitor for capacitance sensing and an additional thin diaphragm for pressure sensing. It is formed by three main components: a diaphragm, a capacitor made of two plates (one is fixed, and the other one is moving), and a mechanical coupling element. All elements are in circular shape to have symmetry for the stresses at the edges where the diaphragm is blocked.

The moving plate of the capacitor is connected to the center of the diaphragm but is electrically isolated from the pressure sensing diaphragm. The fixed plate is placed in parallel with the moving plate to form a parallel plate capacitor, and also it covers the moving plate inside of a sealed cavity. When the diaphragm deflects under a pressure, the moving plates deflects as well, so the diaphragm deflection is converted to a capacitance change. The capacitive sensitivity and dynamic range can be increased independently, because the first scales with increasing the area of the mobile plate and reducing the sensing gap between the moving plate and the fixed plate, while the second scales with the diminishing of the pressure sensing diaphragm. The pressure sensing diaphragm is electrically insulated from the capacitive sensor, while is still mechanically coupled and hermetically sealed in a cavity, so it is protected from the environment. A Faraday cage is formed around the capacitive sensor thanks to a conductive layer that hold at a fixed potential the pressure sensitive diaphragm. These two precautions make the capacitive sensor immune to measure media and resistant to EMI effects.

Some results are presented in figure 20 and 21 for sensors having a 90 and 100 micrometer radius diaphragm respectively, and a 150 micrometers-radius moving plate

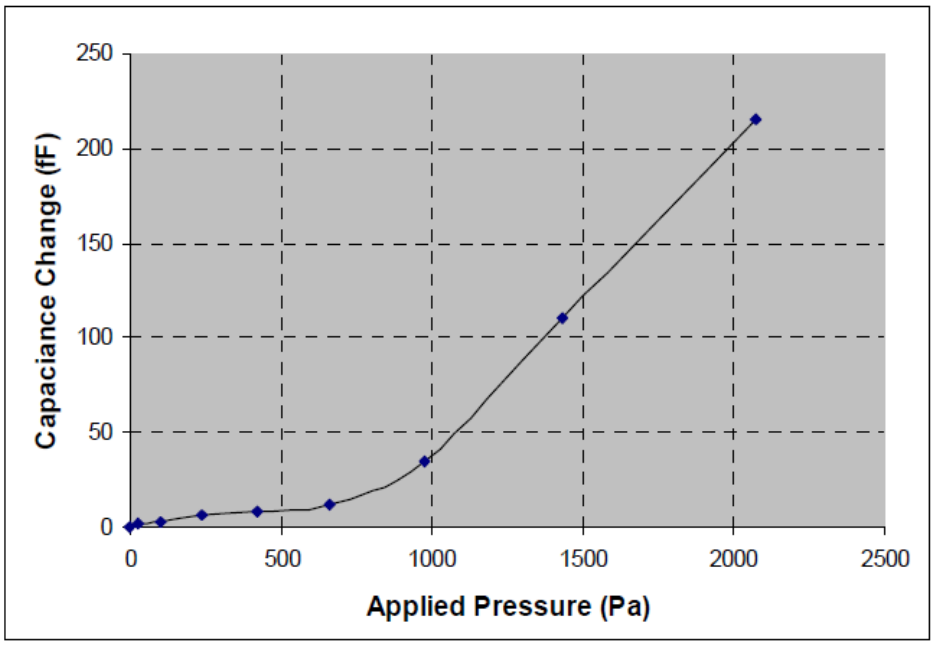

Figure 20: Capacitive pressure sensor performance for a pressure sensor having a 90μm-radius diaphragm and a 150μm-radius moving plate

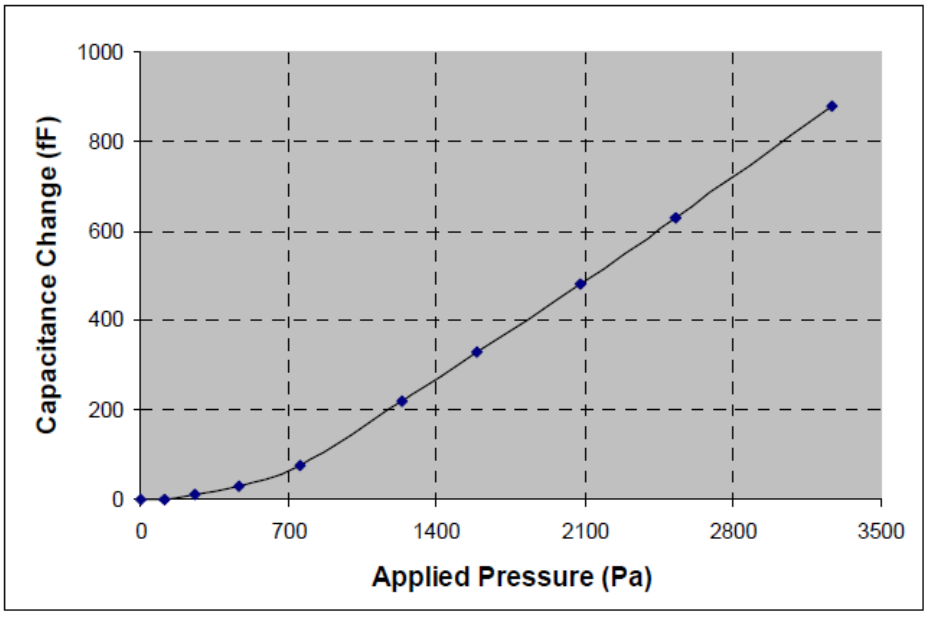

Figure 21: Capacitive pressure sensor performance for a pressure sensor having a 100μm-radius diaphragm and a 150μm-radius moving plate

The last example of a pressure sensor presented is a MEMS high dose radiation resistant SOI (Silicon on insulator) pressure sensor [40]. The die size of the pressure sensors is 3x3 mm. In figure 22 is shown the cross-sectional view and the top view of the sensor.

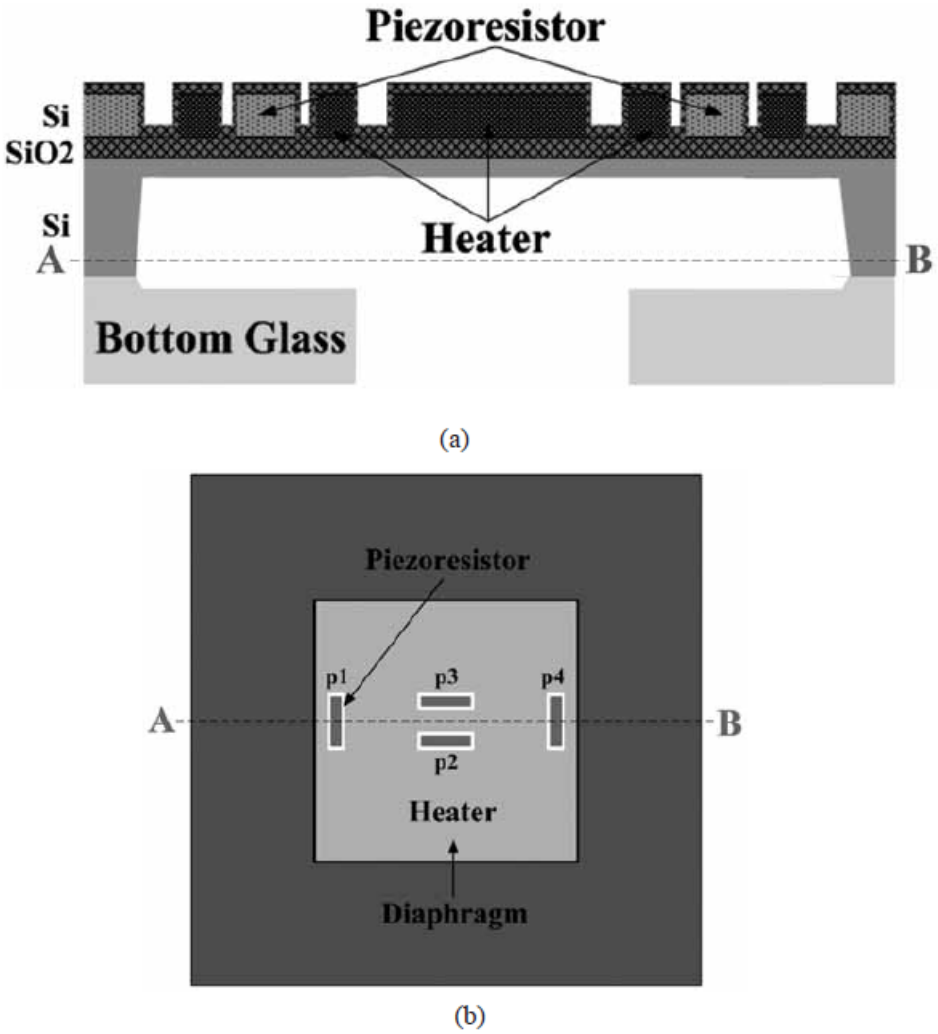

Figure 22: (a) cross-sectional view and (b) top view of the pressure sensor

The piezoresistors that detect the pressure are at the edges and in the center of the diaphragm, and are placed within the microheaters. Both the piezoresistors and the microheaters are made by SOI active layers. When the diaphragm undergoes a deflection, the resistance of the piezoresistors p1 and p4 increase. Those are connected in a Wheatstone bridge configuration, and because of a change in resistance of the piezoresistors, the output voltages of the bridges increases or decreases from the balanced condition. To control the maximum temperature of the sensor, it is used a constant temperature control systems using integrated microheaters. It is controlled for reduction of thermal drift at 200 °C.

In order to test the performance of the sensor under radiations and under a certain temperature, a radiation high as 100 krad is been subjected to it, and the sensor has been kept at 70 °C for 3h.
Figure 23 shows the output voltage variation and pressure for different case: before subjecting the sensor to gamma radiation doses as high as 100 krad, after radiation and after subjecting the sensor to 70 °C for 3h.

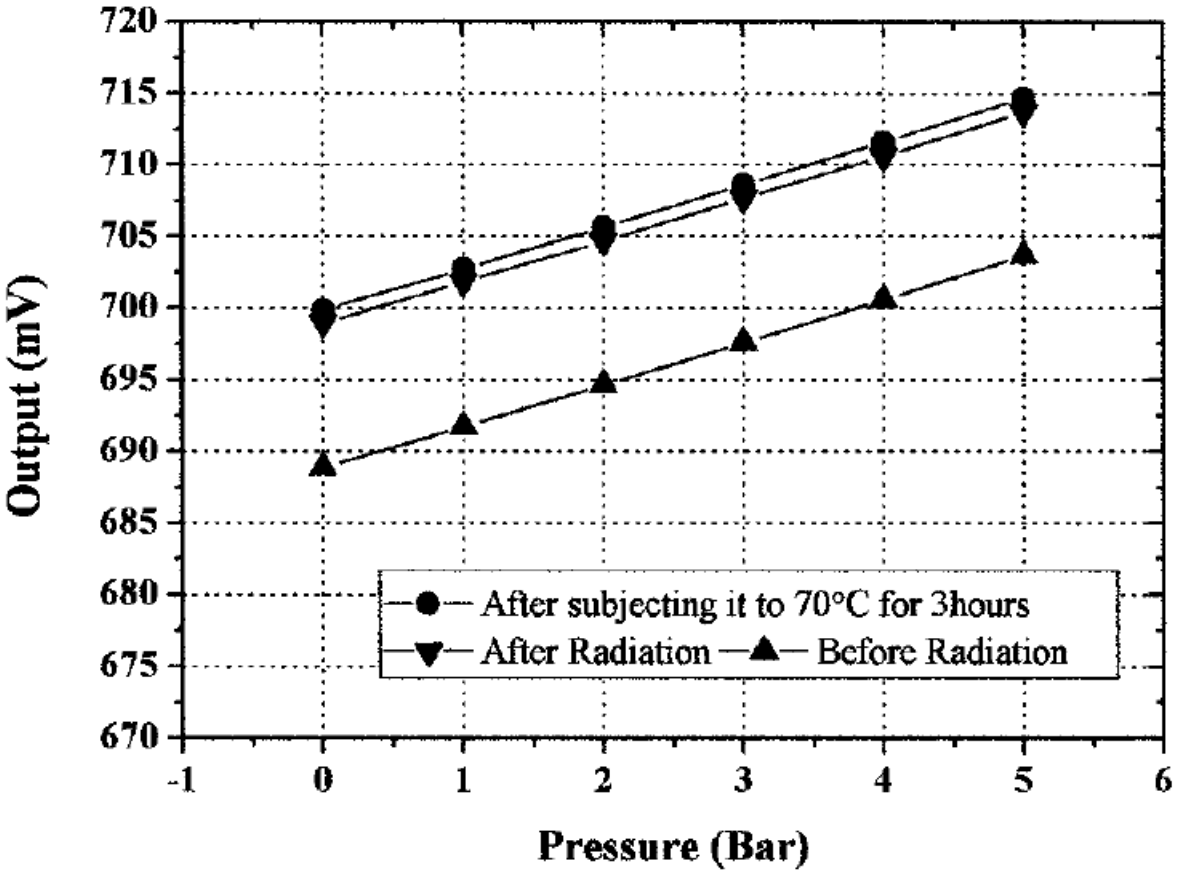

Figure 23: Performance results

Micropump and microregulator

The first example of MEMS micropump reported is a PZT-driven micropump [41] developed at Tsinghua University, China. It's composed by a chamber, a membrane, two microvalves and a driving mechanism. The design is shown in figure 24.

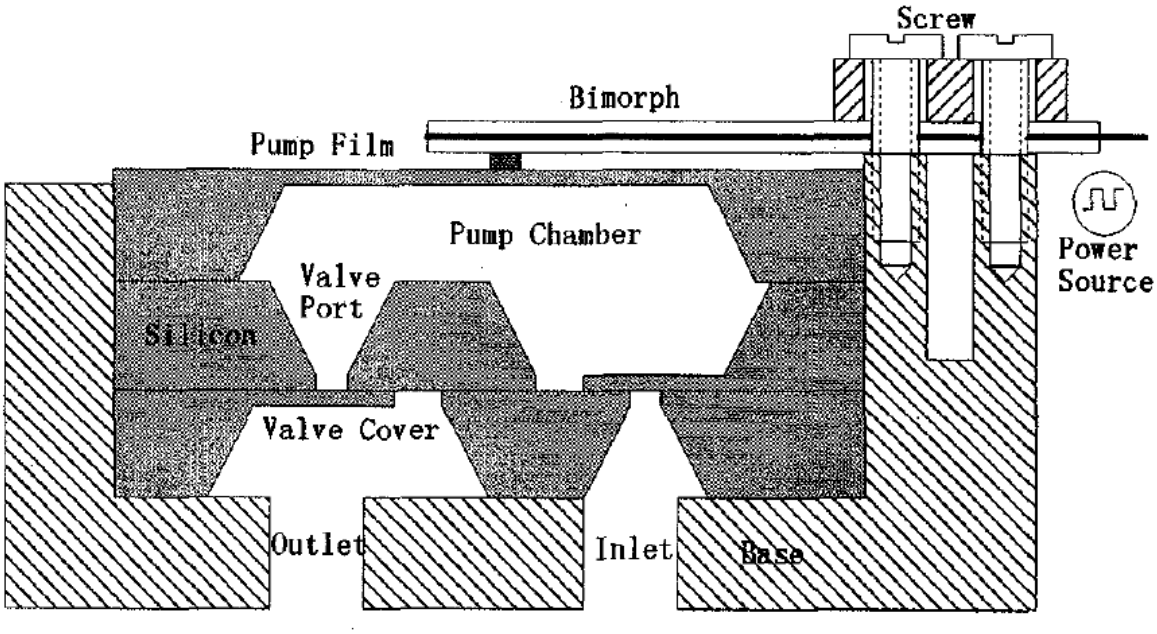

Figure 24: Scheme of the bimorph cantilever actuated micropump

Both the valve cover and the micropump membrane are fabricated using single crystallite silicon. The micropump chamber is round with a 5 mm diameter and a 0.4 mm depth. The choice of the round shape is guided by the advantage of having lower stress concentration in the membrane, and less air bulbs in the chamber when it's filled with fluid. The membrane is 11 micrometers thick. The valve cover is cantilever and its dimension are 1.5 mm x 1.0 mm x 7.4 μm. The valve opening is 200 x 200 μm. The capability of flow is >10 ml/min at a pressure of 10 kPa.

The micropump has an actuation based on inverse piezoelectric effect, and it is made by PZT bimorph cantilever formed by two piezoelectric ceramic cantilevers. One of the bimorph cantilever's end is stuck at the center of the membrane, the other end is instead fixed on the metallic base. When power is applied, the bimorph cantilever is able to bend and vibrate on the tangential direction. Advantages of this actuation is the bidirectional actuation, simpler structure than other mechanism, and short response time.

In figure 25 are shown the experimental results of the flow rate of the micropump, with a driving voltage of 100 V square wave. The precision of this micropump is 1

microliter/min

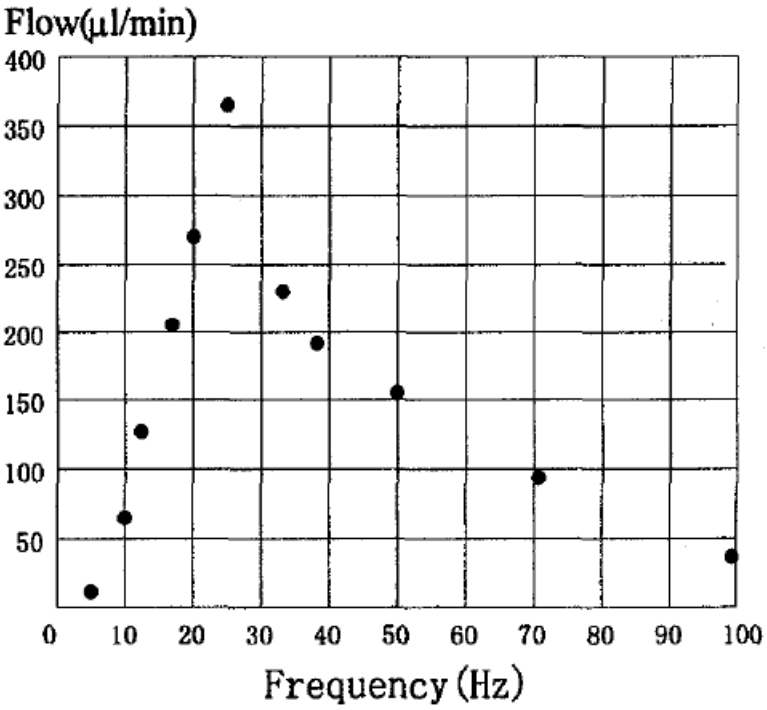

Figure 25: Flow rate of the micropump

An example of a microregulator for space application is the one developed by Pramanick, Das and Bhattacharyya [42] presented here. It's a MEMS based normally closed silicon piezoelectric microregulator for gas and fluid, and it can be integrated with a miniaturized feed system or used as a standalone component for an existing feed system. The cross-sectional view of the device is shown in figure 26.

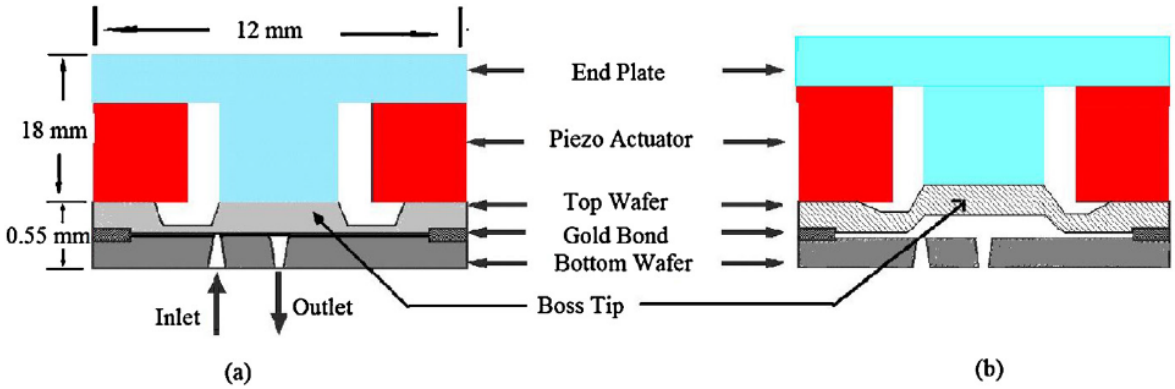

Figure 26: Cross-sectional view of the microregulator in (a) OFF and (b) ON condition

It is composed of a wafer on the bottom, which contains the inlet and the outlet passages, and a wafer on the top which is compressed at the center to obtain the sealing

force, and that functions as a valve. On the top wafer with a central support frame is placed the diaphragm. The piezoelectric actuator is bounded to the top wafer and an end plate. The actuator is made by two zones, one inactive (the end plate) and one active (the piezoelectric actuator itself). The valve is normally closed, so when a voltage is applied, the active zone of the actuator expands, pulling the inactive zone upwards. The inactive zone is bounded to the top wafer, so when it goes upwards, the top wafer follows it, lifting the diaphragm away from the seat. Once the diaphragm is up, a passage between the inlet and the outlet is opened, allowing fluid flow.

In figure 27 and 28 are presented the results of the flow rates using Nitrogen and Water respectively. It is possible to see that the flow rate increases with increasing the voltage and the inlet pressure. Since the flow rate increases with increase in voltage, the valve can also be used as proportional valve. The maximum flow rate for nitrogen (172 sccm) is achieved at 160 V with 6 bar applied pressure.

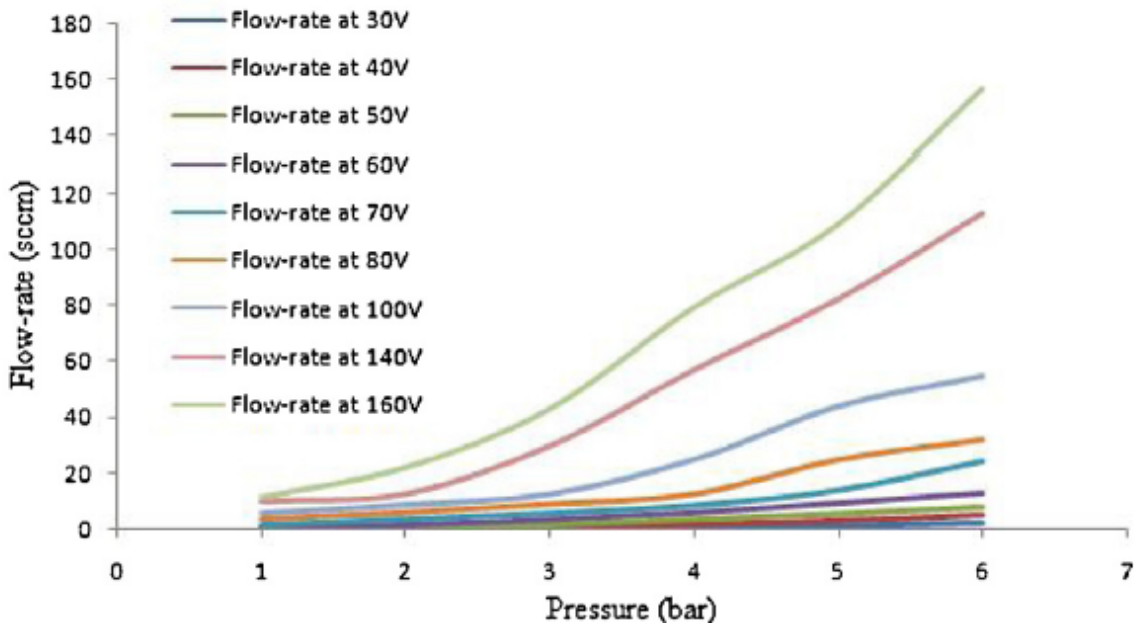

Figure 27: Variation of flow rates with varying voltage and applied pressure in case of Nitrogen.

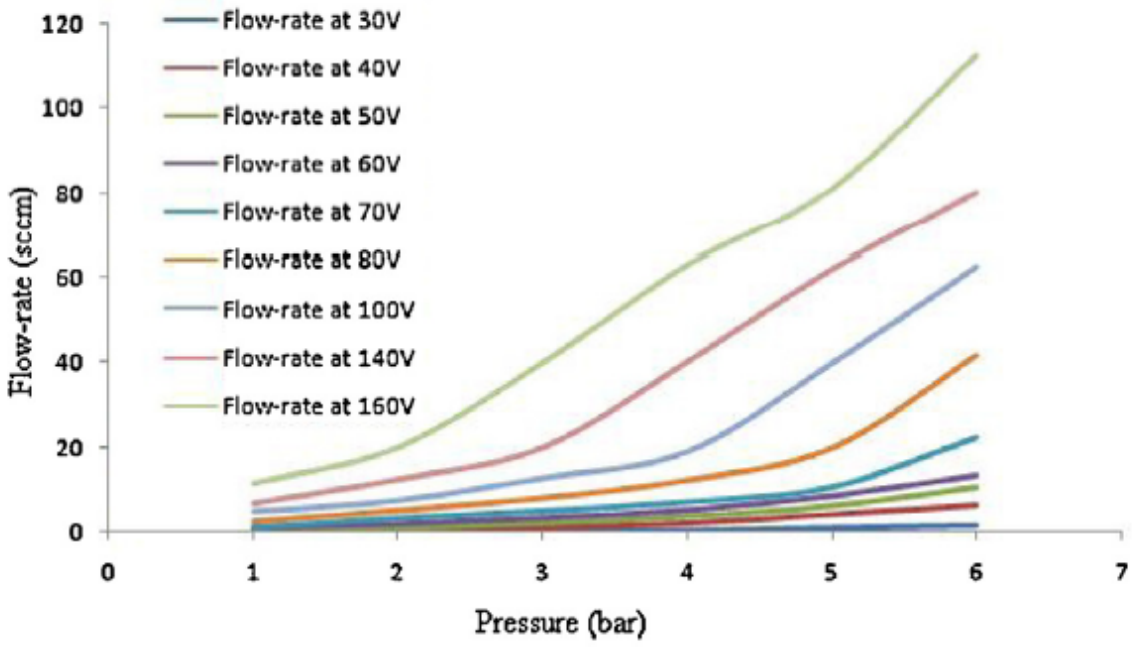

Figure 28: Variation of flow rates with varying voltage and applied pressure in case of water.

2.2 Thrusters

The development of microspacecraft, constellations and formation flying has introduced the need for micropropulsion concepts for orbit maintenance, station keeping and special attitude control. The necessary impulse for these tasks is very small, just enough to overcome the drag, perturbation, error on navigation and control in constellation or formation. A micropropulsion system with small volume, weight and without reducing the reliability of the entire system is therefore required. The requested thrust forces are very precise, and in the order of micro or milli Newton, to provide a high manoeuvrability and capability of the spacecraft.

In this section will be presented three different kinds of micropropulsion systems, in order to cover various needs:

- Solid propellant thruster
- Gas thruster
- Liquid monopropellant thruster

Solid propellant thruster

LAAS-CNRS with the expertise of CNES proposes an array of 16 MEMS solid propellant microthruster individually controlled [43]. The design is shown in figure 29.

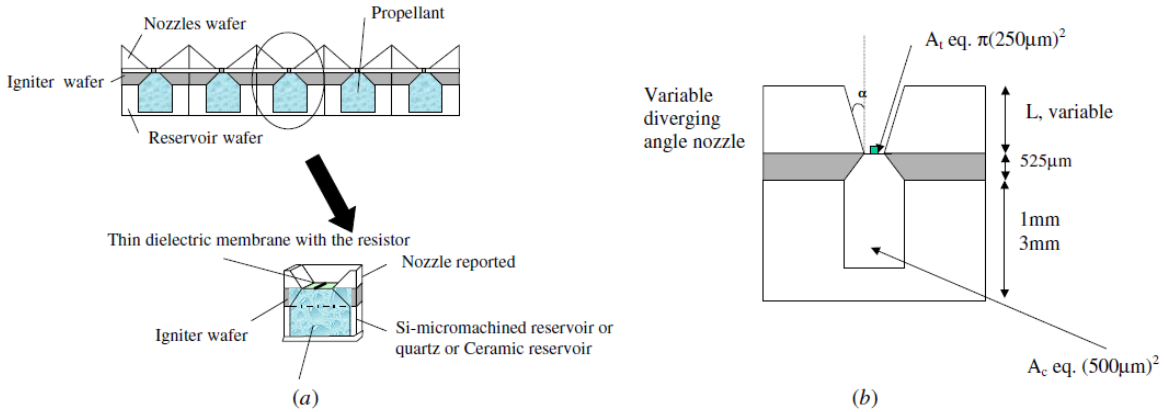

Figure 29: (a) Schematic illustration of the solid propellant microthruster array and (b) geometrical features of a single micothruster

The thrusters are composed of three parts:

- An array of micromachined igniters.
- An array of propellant tanks.
- An array of micronozzle.

The igniter is fabricated starting from a silicon wafer oxidized. The second step is to coat the thermal oxide with a layer of silicon-rich nitride, resulting in a 0.7 micrometers thickness. The third step consists of depositing a 0.5 micrometers thick layer of polysilicon by LPCVD (Low-Pressure Chemical Vapour Deposition) at 605 °C, and patterning using RIE (Reactive Ion Etching) in order to design the resistor. The fourth step is to realize the electrical pads and supply lined in gold. A square window pattern is then opened in the dielectric layer on the back side of the wafer using photolithography and RIE, and lastly, the silicon is etched away with anisotropic etchant.

The propellant tank can be fabricated using low thermal conductive ceramic, or a quartz wafer or a thick silicon substrate. The use of ceramic or quartz allows the minimization of the thermal losses that leads to an optimization of the resulting thrust, and the fabrication of a thrust chamber longer than one millimetre, if needed. In the end, the tank is formed by 1 mm diameter holes micromachined in a 3 mm thick substrate.

The fuel chosen is a GAP (Glycidyle Azide Polymer) mixture formulated for this application. It has three main advantages:

- Is available in paste form, so it suited well to fill very small holes.
- The propellant and combustion gases are non-toxic.
- It requires low electrical power to be ignited. In figure 30 is plotted the electrical power needed to ignite the propellant at different temperatures.

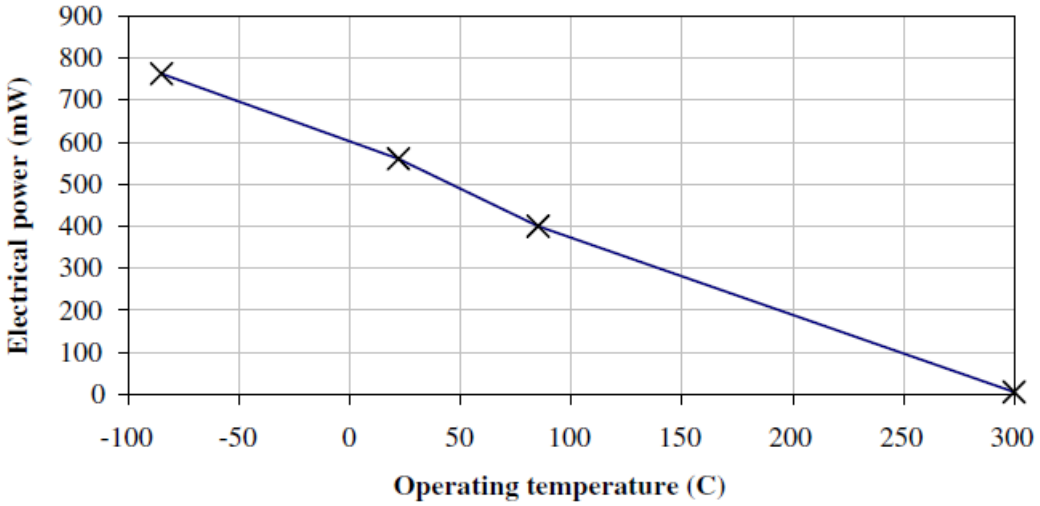

Figure 30: Ignition power

The geometric features of the converging part of the nozzle are fixed by the silicon micromachining, but the diverging part can be varied because is made from ceramic material and then bonded on top of the structure. The diverging length and the semi-divergence angle will be playing a fundamental role in the thrust performance. In the following table 1 are presented the parameters and variables of the nozzle and the propellant:

Table 1: Parameters and variables of the nozzle and the propellant

Combustion temperature	1800 °C
Specific heat at constant pressure	1835 J $kg^{-1}K^{-1}$
Thermal capacity ratio	1.3
Solid propellant density	1528 kg m^{-3}
Molecular weight	19.68 g mol^{-1}
Chamber section	$\pi(0.5\ mm)^2$
Throat section	$\pi(250\ \mu m)^2$
Semi divergence angle	Variable
Chamber length	3 mm
Diverging length	Variable

In conclusion, the thruster can deliver force ranges from 40 to 51 mN, depending on the geometrical features of the diverging part of the nozzle. Figure 31 shows this range, with the diverging length of the nozzle in the x axis, and the diverging angle in the y axis. The best performances are achieved with a 120 micrometers long nozzle and 20° diverging angle, or 500 micrometers long and 5° diverging.

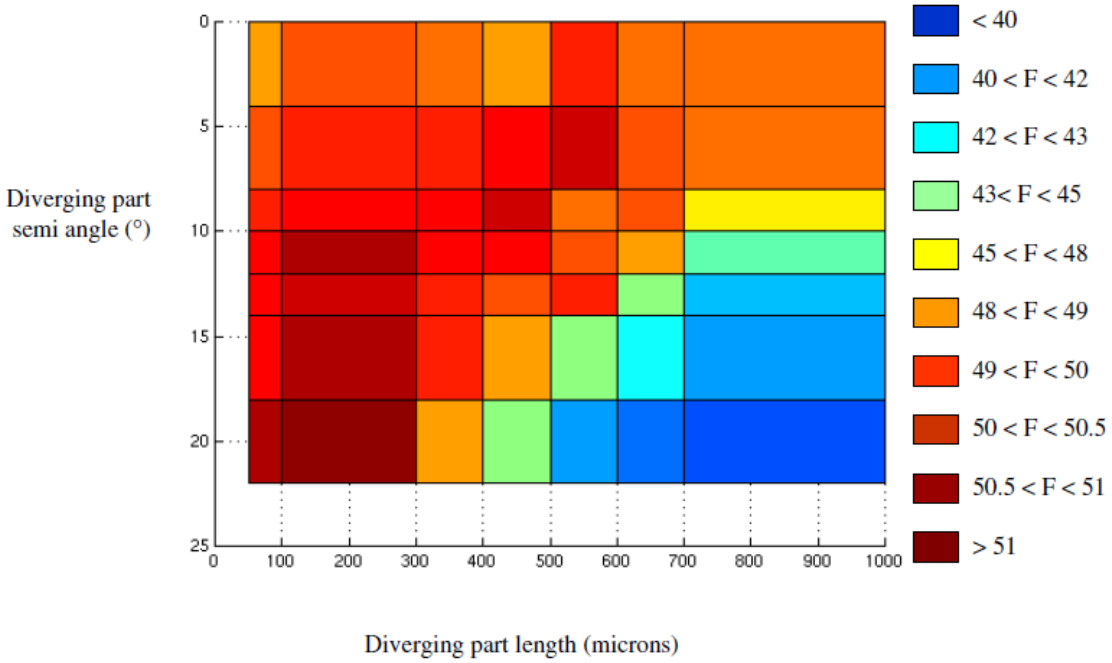

Figure 31: Force (F) as a function of the diverging geometrical features.

Gas thruster

A miniaturized resistojet thruster with an integrated thin-film heater developed by Delf University of Technology is presented below [44]. This device is capable of producing low thrusts in the microNewton – milliNewton range with small size and small weight. The design is shown in figure 32.

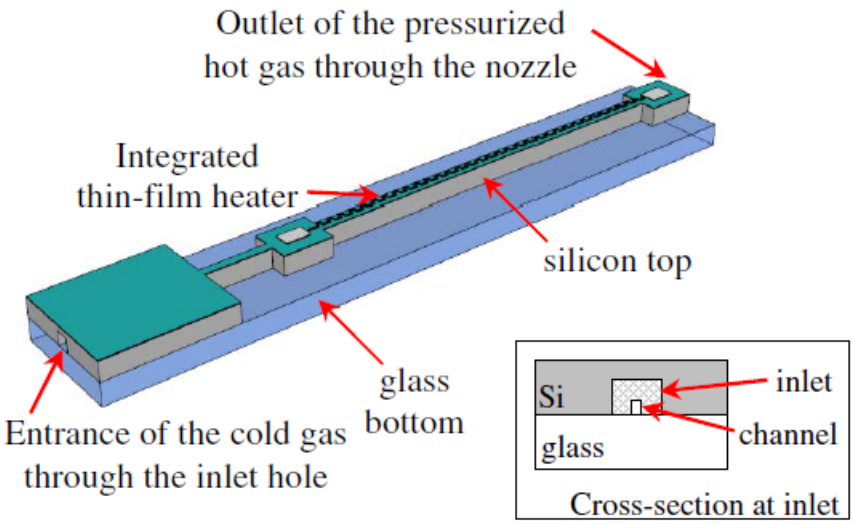

Figure 32: Schematic drawing of the MEMS resistojet

The design is very simple, it consists of one heater to heat up the propellant, and a converging-diverging nozzle to expand the hot gas and achieve thrust. Pressurized cold nitrogen is used as propellant. The nitrogen enters the device through an inlet and the integrated thin-film heater warms it up. The device is made by bulk silicon, which has good thermal conduction properties and spreads the heat. In figure 33 is presented another view of the design, and also an alternate geometry, where three parallel channels are considered in order to reduce pressure drop.

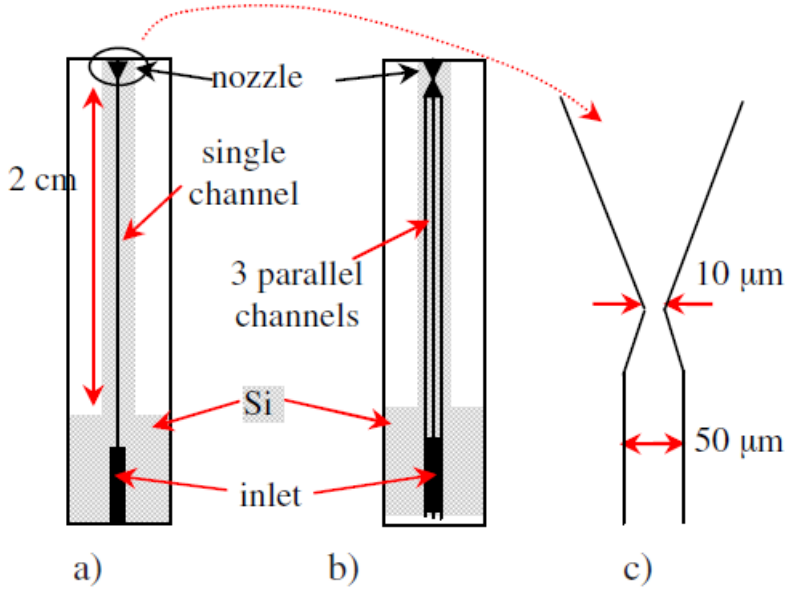

Figure 33: (a) Schematic top view of the channel geometry. (b) Alternative geometry with three parallel channels. (c) Close-up sketch of the nozzle throat

The channel is 50 μm wide, 150 μm deep, and 2 cm long. The expansion ratio of the nozzle is 25:1. The first design considered has a nozzle throat width of 10 or 5 μm, the second design (the one with three channels instead of one) has a nozzle throat width of 10 μm.

The fabrication of the thruster consisted in a four-mask process that started with a double side polished silicon wafer later anodically bonded to a glass wafer. The wafers were 550 μm thick and with a diameter of 100 mm. The first step was to grow a 360 nm thick wet thermal oxide layer to protect the bonding surface and function as insulating layer between silicon substrate and the heater film. Then, a 675 nm thick aluminum layer was deposited and patterned in order to define the film heater. The third step was to deposit a 6 μm thick PECVD (plasma enhanced vapour chemical deposition) silicon oxide layer on both sides of the silicon wafer. The last step was to etch with DRIE process the three different depths, one for the channel and the nozzle, one for the inlet, and the last one to define the resistojet. In figure 34 is illustrated a summary of the fabrication process.

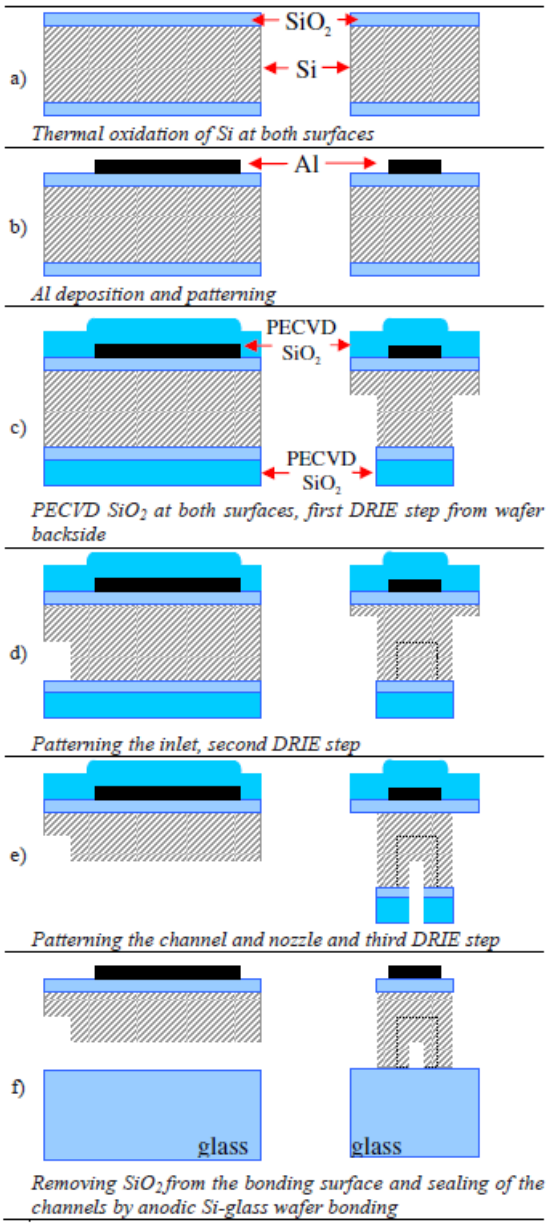

Figure 34: Schematic fabrication sequence along longitudinal (left) and lateral (right) cross-section

The final dimension of the device was 25 x 5 x 1 mm, with a weight of 162 mg. In figure 35 is shown the expected thrust for the device with the 10 μm wide nozzle throat, with and without heating (up to 350 °C). The thrust range varies from 20 microN (with a flow of 0.15 mg/s) to 960 microN (flow of 1.5 mg/s, a value that causes the system pressure to reach its maximum value of 6 bar). In order to heat up the flow to the working temperature, is required additional power heating, in order of circa 1 mW/K for mass flow rates of 1 mg/s.

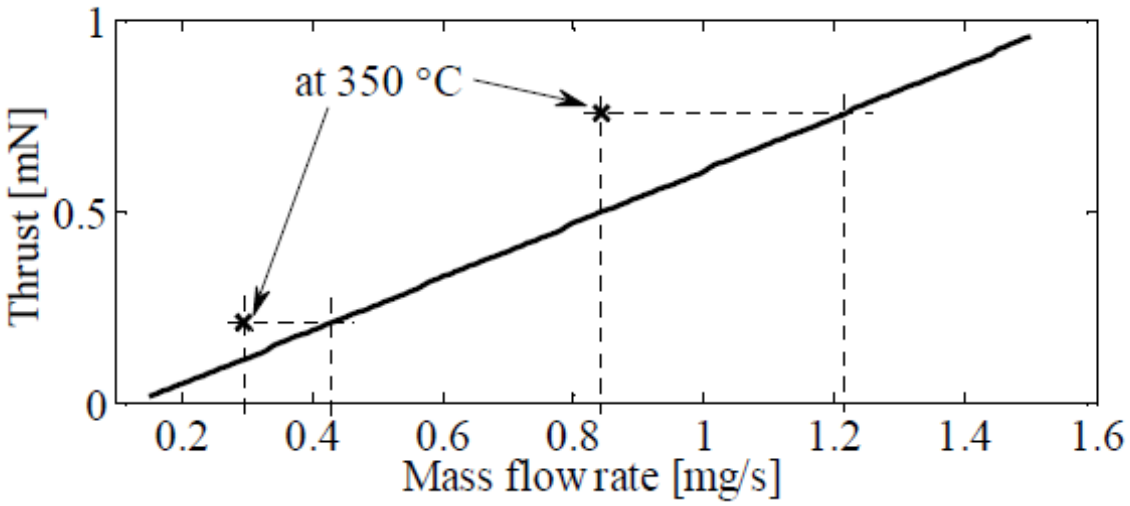

Figure 35: Thrust calculated for gas flow without heating. Increase of the thrust by heating is also shown.

Liquid monopropellant thruster

The last thruster presented is a monopropellant MEMS-based microthruster that use catalyzed hydrogen peroxide decomposition as propulsion mechanism, developed by NASA Goddard Space Flight Center [45]. The operating principle of this device consists in liquid hydrogen peroxide of high purity (90%) fed into an injector that produces the desired pressure drop. Then, the liquid is fed into a catalytic chamber where undergoes a chemical decomposition and produce high-velocity gaseous products. The gases finally are fed into a converging-diverging nozzle, where the flow reach a supersonic velocity producing thrust. In figure 36 is shown the design of the thruster.

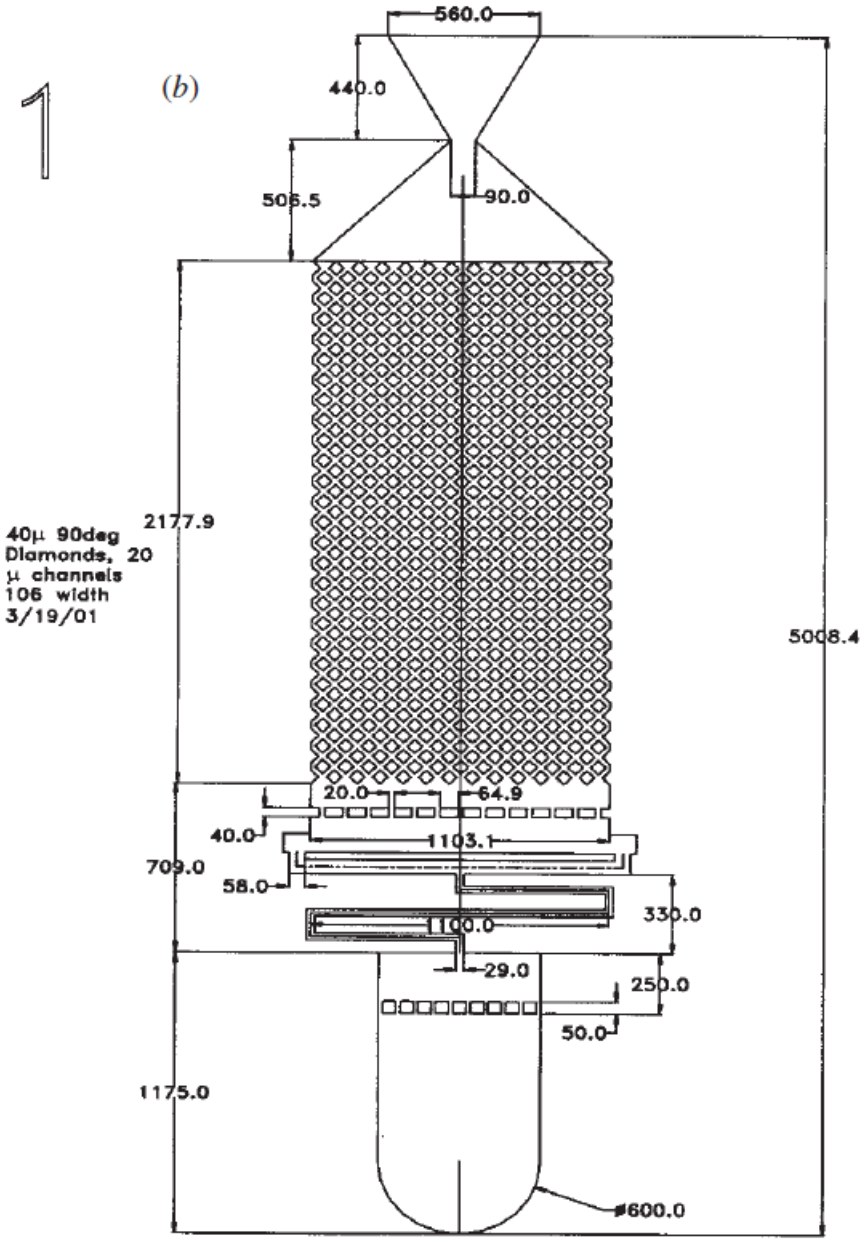

Figure 36: Mechanical drawing showing top view of the microthruster design geometry

The main design goal of the catalytic chamber it to be the right size to achieve complete decomposition of the mass flow rate of propellant. For this device, several geometries were considered. The final design featured a long channel with vertical pillars coated with the silver catalyst. The chamber is approximately 2.2 millimeters long, and between 50 and 300 micrometers high. The diamond pillars have a square cross section with 40 micrometers side and are rotated 45° with respect to the flow axis. The aim was to create a maximum silvered surface area to increase the rate of decomposition. The critical parameter was the critical residence time of the propellant. To design the chamber, empirical

catalyst length reported in the literature [46] was used, scaling them to the MEMS dimension.

Between the catalyst chamber and the propellant tank, an injector was placed, in order to avoid back-flow and to reduce the propellant pressure through viscous effects. It consists in a series of microchannels with 90° bends. They have a rectangular cross-section with a 50-300 micrometers depth and 29 micrometers width. At the inlet of the injector there is a filter to trap the particulates that might be present in the mass flow. The filter consists of vertical pillars with 50 micrometers square cross-section, and a gap of 25 micrometers from one another. Another similar filter is placed at the end of the injector, right before the inlet of the chamber. This filter consists of vertical pillars with a rectangular cross-section of 65 micrometers by 40 micrometers, with a gap of 20 micrometers. The aim of this filter is to align and distribute the flow exiting the injector.

Regarding the nozzle, a throat area of 9000 μm^2 was chosen, in order to achieve the sonic condition. Given a thruster depth of 100-300 micrometers, this corresponds to throat width of 30-90 micrometers. The divergence half-angle of expansion was chosen in the range of 30°, given the viscous considerations and the data in the literature, claiming that the low-Reynolds microscale nozzles perform better with larger angles [47]. In table 2 there is a summary of the design and operating parameter of the nozzle.

Table 2: Nozzle parameters

Nozzle Parameter	**Value**
Thrust level	500 μN
Maximum specific impulse	180 s
Specific impulse efficiency	80%
Mass flow rate	400 g s^{-1}
Throat area	9000 μm^2
Inlet pressure	5-6 psia
Outlet pressure	$\sim$ 0 psia
Inlet Mach number	0.05
Exit Mach number	3.3
Reynolds number (throat)	4.50

The fabrication of this thruster consisted of three main steps:

- The first was to create a photographic mask design which contained the thruster design, and to patterned it onto the silicon substrate using standard photolithographic. Then, the substrate was etched by DRIE (Deep Reactive Ion Etching).
- The second was to deposit a 1 micrometer layer of high purity silver (>99.99%) on the surface, in order to create the catalytic chamber surface. In order to avoid the silver covering unwanted surfaces, an aluminum shadow mask was used to cover them. To achieve good adherence of the silver to the substrate, a 1 micrometer thick layer of titanium was deposited onto the surface before applying the silver.
- The last step consisted in the anodically bonding of a Pyrex glass cover plate on the silicon wafer, to seal the thruster. The glass was used only in this prototype in order to see the decomposition process inside the catalytic chamber. The final design will not include the glass, but silicon instead.

3. Propellant

3.1 Properties of studied propellants

In order to achieve the best and more suitable performances for the MEMS thruster in developing, the choice of the right propellant is fundamental. It has to be easy to storage, not requiring too much power to be heated, not be dangerous and toxic, and must be able to achieve the thrust needed. The propellants studied for this work are:

- Nitrogen
- Helium
- Water
- N_2O
- N_2O + Propane with O/F = 7
- Ammonia
- Nitromethane
- H_2O_2 90%
- Propane
- H_2O_2 50% + Ethanol (8.7:1)

In table 3 are listed the storage conditions of the studied propellants. It also shows the calculated ΔH from liquid condition to vapour condition for the propellants stored in saturation condition. Data are collected from the NIST archive [48].

Table 3: Storage conditions of studied propellants

Propellant	**T [K]**	**p [bar]**	**Vapor density [kg/m^3]**	**Liquid density [kg/m^3]**	**ΔH liq-vap [kJ/kg]**
Nitrogen	298.15	300	296.81	/	/
Helium	289.15	300	42.538	/	/
Water	298.15	/	/	1000	/
N_2O	298.15	56.518	188.77	742.93	147.57
N_2O + Propane (O/F = 7)	298.15	56.518	/	701.686	/
Ammonia	298.15	10.027	7.801	602.96	1165.83
Nitromethane	298.15	/	/	1137	/
H_2O_2 90%	298.15	/	/	1387.7	/
Propane	298.15	9.521	20.618	492.36	335.73
H_2O_2 50% + ethanol (8.7:1)	298.15	/	/	1131.9	/

The second step to evaluate the performances of the propellants considered, is to find the combustion parameters like the chamber temperature T_{cc}, the characteristic velocity c*, the specific impulse Isp and the impulse density Isp_ρ. These parameters are reported in table 4 and 5 and are calculated using a thermochemistry program called "CproPEP" and the NIST databook with the following considerations:

- In CproPEP it was used a value of 70 for “supersonic exit to throat area”.
- To calculate the ΔH of Nitrogen, Helium and Water the starting temperature is 298.15 K.
- To calculate the ΔH of Ammonia the starting temperature is 277.30 K at 5 bar pressure, and 331.32 K at 25 bar of pressure, both in liquid state. The NIST databook for Ammonia reach the maximum temperature of 725 K.
- To calculate the ΔH of the decomposed ammonia was used a weighted average between N_2 and H_2 to find the c_p, and were used the same initial conditions of the ammonia.
- To calculate the c* of the decomposed ammonia was used a weighted average between N_2 and H_2 to find k and the molar mass M_m.

- The decomposed ammonia was considered already decomposed in the initial condition.

Table 4: Isp and c* of some propellants by CproPEPShell

Propellant	**T chamber [K]**	**c* [m/s]**	**Isp [s]**	$\boldsymbol{Isp_\rho[10^3 kg \cdot s/m^3]}$
N_2O	1676.038	1033.719	187.61	139.381
N_2O + propane (O/F = 7)	3035.889	1590.082	307.55	215.803
Nitromethane	2440.274	1530.360	292.65	337.788
H_2O_2 90%	1019.59	935.282	172.02	238.540
H_2O_2 90% + propane (O/F = 7)	2624.78	1615.790	318.90	360.390
H_2O_2 50% + ethanol (8.7:1)	1450.17	1183.017	224.46	254.066

The last step is to find the thrust and the mass flow achievable with the propellants. In order to calculate that, two different throat diameters were used, of 30 μm and 800 μm respectively, and two different operative pressures, 5 and 25 bar. Tables 7, 8, 9 and 10 also show the power needed to heat up the propellants that require it.

Table 5: Properties of some propellants calculated using NIST data and CproPEPShell

Propellant	**T [K]**	**p [bar]**	**c* [m/s]**	**Isp [s]**	ΔH [kJ/kg]	$\boldsymbol{Isp_\rho}$ $10^3[kgs/m^3]$	**p [bar]**	ΔH [kJ/kg]
Nitrogen	298.15	5	434.438	77.162	/	22.902	25	/
	373.15	5	486.018	86.323	78.53	25.621	25	80.4
	573.15	5	602.344	106.984	289.77	31.753	25	293.94
	773.15	5	699.588	124.256	508.37	36.880	25	513.53
	1073.15	5	824.216	146.392	853.62	43.450	25	859.47
	1273.15	5	897.740	159.451	1093.52	47.326	25	1099.67
Helium	298.15	5	1083.7	179.420	/	7.632	25	/
	373.15	5	1212.4	200.723	389.5	8.538	25	389.5
	573.15	5	1502.6	248.765	1428.1	10.581	25	1428
	773.15	5	1745.1	288.926	2466.7	12.290	25	2466.3
	1073.15	5	2056.0	340.396	4024.5	14.473	25	4023.8
	1273.15	5	2239.4	370.762	5063.1	15.771	25	5062.2
Water	573.15	5	771.184	143.152	2959.31	143.152	25	2902.16
	673.15	5	835.757	155.139	3167.01	155.139	25	3132.96
	873.15	5	951.850	176.689	3597.21	176.686	25	3579.66
	1073.15	5	1055.2	195.882	4053.1	195.882	25	4042.06
	1273.15	5	1149.4	213.356	4536.11	213.356	25	4528.46
Ammonia	298.15	5	571.746	106.132	1301.61	63.993	25	/
	373.15	5	639.631	118.733	1480.01	71.591	25	1150.06
	573.15	5	792.724	147.151	1971.61	88.726	25	1688.26
	725	5	891.573	165.500	2388.81	99.789	25	2114.06
	1073.15	5	1084.7	201.353	/	121.407	25	/
	1273.15	5	1181.5	219.315	/	132.238	25	/
Decomposed Ammonia N_2 14/17 - H_2 3/17	298.15	5	790.215	141.428	73.329	85.275	25	/
	473.15	5	995.468	178.163	688.804	107.425	25	501.511
	673.15	5	1187.4	212.508	1392.204	128.133	25	1208.711
	873.15	5	1352.3	242.027	2095.604	145.932	25	1915.911
	1073.15	5	1499.2	268.318	2799.004	161.785	25	2623.111
	1273.15	5	1632.9	292.253	3502.405	176.216	25	3330.311

Table 6: Thrust and $\dot{m}$ of the propellants with different pressures and throat diameters (D_g)

Propellant	**p [bar]**	$\boldsymbol{D_g[\mu m]}$	$\boldsymbol{\dot{m}}$ **[mg/s]**	**Thrust [N]**
N_2O	5	30	0.342	629e-04
	5	800	243	0.447
	25	30	1.71	3.14e-03
	25	800	1215	2.235
N_2O + Propane (O/F = 7)	5	30	0.222	6.70e-04
	5	800	158	0.476
	25	30	1.11	3.35e-03
	25	800	790	2.383
Nitromethane	5	30	0.231	6.63e-04
	5	800	164	0.471
	25	30	1.15	3.31e-03
	25	800	820	2.355
H_2O_2 90%	5	30	0.378	6.37e-04
	5	800	269	0.453
	25	30	1.89	3.18e-03
	25	800	1345	2.266
H_2O_2 90% + Propane (O/F = 7)	5	30	0.219	6.84e-04
	5	800	156	0.486
	25	30	1.09	3.42e-03
	25	800	750	2.432
H_2O_2 50% + Ethanol (8.7:1)	5	30	0.299	6.58e-04
	5	800	212	0.467
	25	30	1.49	3.29e-03
	25	800	1060	2.335

Table 7: Thrust, $\dot{m}$ and power for Nitrogen, Helium and Water at 5 bar pressure with different D_g

Propellant	**p [bar]**	**T [K]**	$\boldsymbol{D_g[\mu m]}$	$\boldsymbol{\dot{m}}$ **[mg/s]**	**Thrust [N]**	**Power [W]**
Nitrogen	5	298.15	30	0.814	6.155e-04	/
		373.15	30	0.727	6.155e-04	0.057
		773.15	30	0.505	6.155e-04	0.257
		1273.15	30	0.394	6.155e-04	0.431
		298.15	800	578.51	0.437	/
		373.15	800	517.12	0.437	40.609
		773.15	800	359.25	0.437	182.631
		1273.15	800	273.93	0.437	306.141
Helium	5	298.15	30	0.326	5.737e-04	/
		373.15	30	0.292	5.737e-04	0.113
		773.15	30	0.203	5.737e-04	0.499
		1273.15	30	0.158	5.737e-04	0.799
		298.15	800	231.91	0.408	/
		373.15	800	207.30	0.408	80.743
		773.15	800	144.02	0.408	355.254
		1273.15	800	112.23	0.408	568.231
Water	5	573.15	30	0.458	6.433e-04	1.356
		873.15	30	0.371	6.433e-04	1.336
		1273.15	30	0.307	6.433e-04	1.395
		578.15	800	325.90	0.457	964.439
		873.15	800	264.04	0.457	949.807
		1273.15	800	218.66	0.457	991.865

Table 8: Thrust, $\dot{m}$ and power for Ammonia and decomposed Ammonia at 5 bar pressure with different D_g

Propellant	**p [bar]**	**T [K]**	$\boldsymbol{D_g[\mu m]}$	$\boldsymbol{\dot{m}}$ **[mg/s]**	**Thrust [N]**	**Power [W]**
Ammonia	5	298.15	30	0.618	6.433e-04	0.804
		373.15	30	0.553	6.433e-04	0.818
		573.15	30	0.446	6.433e-04	0.879
		725	30	0.396	6.433e-04	0.946
		298.15	800	439.58	0.457	572.162
		373.15	800	392.93	0.457	581.540
		573.15	800	317.04	0.457	625.079
		725	800	281.89	0.457	673.382
Decomposed ammonia N_2 14/17 - H_2 3/17	5	298.15	30	0.447	6.203e-04	0.033
		473.15	30	0.355	6.203e-04	0.245
		873.15	30	0.261	6.203e-04	0.547
		1273.15	30	0.216	6.203e-04	0.757
		298.15	800	318.05	0.441	23.322
		473.15	800	252.47	0.441	173.902
		873.15	800	185.85	0.441	389.468
		1273.15	800	153.91	0.441	539.055

Table 9: Thrust, $\dot{m}$ and power for Nitrogen, Helium and Water at 25 bar pressure with different D_g

Propellant	**p [bar]**	**T [K]**	$\boldsymbol{D_g[\mu m]}$	$\boldsymbol{\dot{m}}$ **[mg/s]**	**Thrust [N]**	**Power [W]**
Nitrogen	25	298.15	30	4.068	0.003	/
		373.15	30	3.636	0.003	0.270
		773.15	30	2.526	0.003	1.297
		1273.15	30	1.968	0.003	2.164
		298.15	800	2890	2.199	/
		373.15	800	2580	2.199	207.432
		773.15	800	1796	2.199	922.299
		1273.15	800	1390	2.199	1528.541
Helium	25	298.15	30	1.631	0.003	/
		373.15	30	1.458	0.003	0.568
		773.15	30	1.013	0.003	2.497
		1273.15	30	0.789	0.003	3.995
		298.15	800	1150	2.023	/
		373.15	800	1036	2.023	403.522
		773.15	800	720.08	2.023	1775.933
		1273.15	800	561.14	2.023	2840.603
Water	25	573.15	30	2.292	0.003	6.651
		873.15	30	1.857	0.003	6.646
		1273.15	30	1.538	0.003	6.963
		578.15	800	1620	2.320	4701.985
		873.15	800	1320	2.320	4725.151
		1273.15	800	1090	2.320	4936.021

Table 10: Thrust, $\dot{m}$ and power for Ammonia and decomposed Ammonia at 25 bar pressure with different D_g

Propellant	**p [bar]**	**T [K]**	$\boldsymbol{D_g[\mu m]}$	$\boldsymbol{\dot{m}}$ **[mg/s]**	**Thrust [N]**	**Power [W]**
Ammonia	25	331.32	30	2.932	0.003	/
		373.15	30	2.765	0.003	3.179
		573.15	30	2.229	0.003	3.763
		725	30	1.982	0.003	4.190
		331.32	800	2085.59	2.320	/
		373.15	800	1965.65	2.320	2260.615
		573.15	800	1585.2	2.320	2676.229
		725	800	1409.45	2.320	2979.662
Decomposed ammonia N_2 14/17 - H_2 3/17	25	331.32	30	2.121	0.003	/
		473.15	30	1.775	0.003	0.890
		873.15	30	1.307	0.003	2.504
		1273.15	30	1.082	0.003	3.603
		331.32	800	1508.54	2.220	/
		473.15	800	1262.35	2.220	633.082
		873.15	800	929.26	2.220	1780.379
		1273.15	800	769.56	2.220	2562.874

The propellant chosen for our work was Nitromethane, due to its suitable properties. As it is possible to see from the tables, Nitromethane achieve with combustion a high c*, I_{sp}, and, more important, a great value of $Isp_{denisty}$, with a chamber temperature lower than its closest competitors (N_2O + propane, H_2O_2 90% + propane). With these properties is possible to achieve great performances in terms of thrust, as we can see in table 6, ranging from $6.63e^{-4}$ to 2.355 N, depending on the pressure in the chamber and the throat diameter.

In the following table is shown a summary of nitromethane properties:

Table 11: Nitromethane summary

Property	Value	Unit
ρ_{liq}	1137	kg/m^3
T_c	2440.274	K
c^*	1530.360	m/s
I_{sp}	292.65	s
I_{sp_ρ}	337.788	$10^3(kg \cdot s/m^3)$
S=f(p, D_g)	$6.63e^{-4}$ - 2.355	N
p	5, 25	bar
D_g	30, 800	μm

3.2 Nitromethane

Nitromethane is a liquid propellant that offers high performances with a relatively non-toxic nature. Its chemical formula is CH_3NO_2. The molecule is essentially methane with one of the four hydrogens replaced by a nitro group, and is the simplest of possible energetic CHON molecules that contain nitro groups group [49]. In figure 37 it is shown its molecular structure.

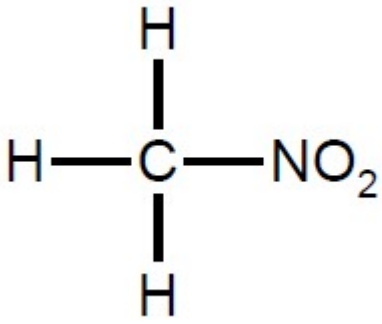

Figure 37: Nitromethane molecular structure

Its primary use is as a chemical intermediate in the synthesis of biocides, chemicals, and agricultural products and intermediates. It can also be used as a fuel for professional racing and rockets, as explosive in mining, oil-well drilling, and seismic exploration [50].

Nitromethane is a clear, mobile, and colorless liquid at room temperature with a mod-

erately strong characteristic odor. It's classified as a "flammable liquid" for storage and shipping, and it may detonate when shocked with sufficient energy. When contaminated with amines, strong acids, or alkalis it can be explosion sensitized. Some metals ions like lead, copper, and alloys containing these metals, are incompatible with nitromethane, and can promote its decomposition. Materials such rubbers, coating and some plastics instead can react directly with it [49].

During its production and use as a solvent and fuel additive, it may be release in the environment and the atmosphere. Its potential for mobility in the soil depends on the vapor pressure, and it's not considered biodegradable, although this does not mean that under some environmental conditions it cannot be considered biodegradable. Regarding the damages it can cause on humans, pure nitromethane has low acute toxicity following accidentally ingestion or dermal exposure where small amounts of substance are not likely to cause injury; it's a mild eye irritant and is not likely to cause significant irritation to the skin. Even though in small quantities is not dangerous, excessive exposure to nitromethane vapors can cause irritation in the upper respiratory tract and lungs, and can also cause headache, dizziness, drowsiness, unconsciousness and, in serious cases, even death. However, in the published scientific literature there are no epidemiological evidence or case reports specific to human exposure. Regarding its carcinogenicity, there are no epidemiological data suggesting that, but the results of a 2-year chronic inhalation study in rats conducted by the U.S. National Toxicology Program (NTP) reported evidence of carcinogenic activity in female rats, male and female mice. For this reason, nitromethane is listed as a potential carcinogen to humans in Group 2B by the International Agency for Research on Cancer (IARC) and in Group A3 by American Conference of Governmental Industrial Hygienists (ACGIH) [50]. Physical and chemical safety data for nitromethane are shown in table 12 from [51]

Table 12: Physical and chemical safety data for Nitromethane

Property	Value	Unit	Notes
Physical State	Liquid	/	at 20 °C
Color	Colorless	/	
Odor	Fruity, disagreeable	/	
pH	6.4	/	at 0.01 g/l at 20 °C
Flash point - close cup	35	°C	
Flash point - open cup	44.44	°C	
Auto-Ignition Temperature	418	°C	
Lower Explosion Limit	7.3	% Volumetric	
Decomposition Temperature	315	°C	
Water Solubility	ca. 100	g/l	at 20 °C
Evaporation Rate	1.39	/	butyl acetate = 1

In table 13 and 14 are presented some properties of nitromethane at one atmosphere.

Table 13: Properties of Nitromethane at one atmosphere

Property	Value	Unit	Notes
Molecular Weight	61.040	g/mol	
Liquid Density, ρ	1.1371	g/cm^3	at 20 °C
Boiling Point	374.35	K	
Freezing Point	244.60	K	
Specific Heat, c_p	105.98	J/mol-K	at 25 °C
Enthalpy of Fusion, ΔH_{fus}	9.703	kJ/mol	at f.p.
Enthalpy of Vaporization, ΔH_{vap}	33.99	kJ/mol	at b.p.
Enthalpy of Formation (for liquid state)	-113.1	kJ/mol	
Heat of Combustion	709.188	kJ/mol	

Table 14: Critical and Triple Point of Nitromethane

Property	Temperature [K]	Pressure [kPa]
Critical Point	588.15	6312.6
Triple Point	244.60	0.14015

3.2.1 Vaporization, fusion and sublimation curves

The liquid-vapour line has a great engineering importance, and it's well documented for nitromethane. The most recent correlation between vapor pressure and temperature was developed by the DIPPR project[49], and it's based on regression analysis of six different studies over the entire temperature range where the liquid-vapor phase transition exists. The function used was:

$$P = e^{(A+\frac{B}{T}+ClnT+DT^E)} \tag{3.1}$$

With the following coefficients:

Table 15: Coefficients for nitromethane vapor pressure correlation

Temperature [K]	A	B	C	D	E
244.60 to 588.15	8.7411e1	-7.1332e3	-9.7786	7.9061e-6	2.0000

Thanks to [51] is possible to see this correlation plotted in figure 38.

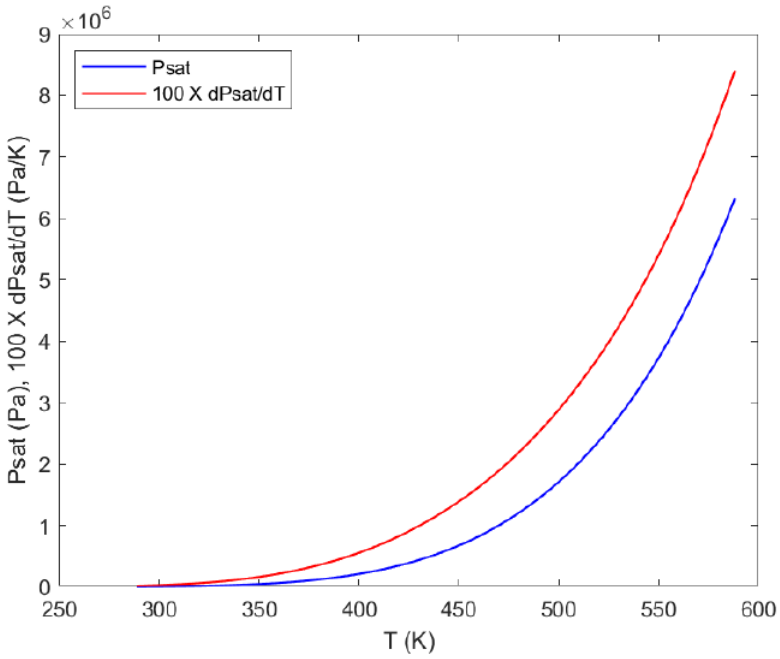

Figure 38: Saturation pressure and its derivative vs Temperature

The freezing point (solid-liquid transition) has been determined as a function of pressure in high-pressure studies. Computed values are found using the Simon-Glatzel equation [52]:

$$P = aT^b + c \tag{3.2}$$

With the coefficients illustrated in the following table:

Table 16: Coefficient for the Simon-Glatzel equation for high pressure nitromethane fusion curve

Coefficient	Value
a	1.597e-5
b	2.322
c	-6.74

For the solid-vapor phase transition, the sublimation line can be approximately calculated knowing the enthalpy of sublimation and a single equilibrium point and using the

Clausius-Clapeyron relationship:

$$ln(\frac{P}{P_0}) = \frac{\Delta H}{R}(\frac{1}{T_0} - \frac{1}{T}) \tag{3.3}$$

Where P_0 is the vapor pressure at the known temperature T_0, ΔH is the enthalpy of the phase transition, and T is the temperature at which the vapor pressure P is to be determined.

It is possible to develop a phase diagram combining the points and phase transitions. The temperature ranges from the triple and the critical points, and the pressure from 10^{-5} to 10^{7} kPa. The diagram is shown in figure 39:

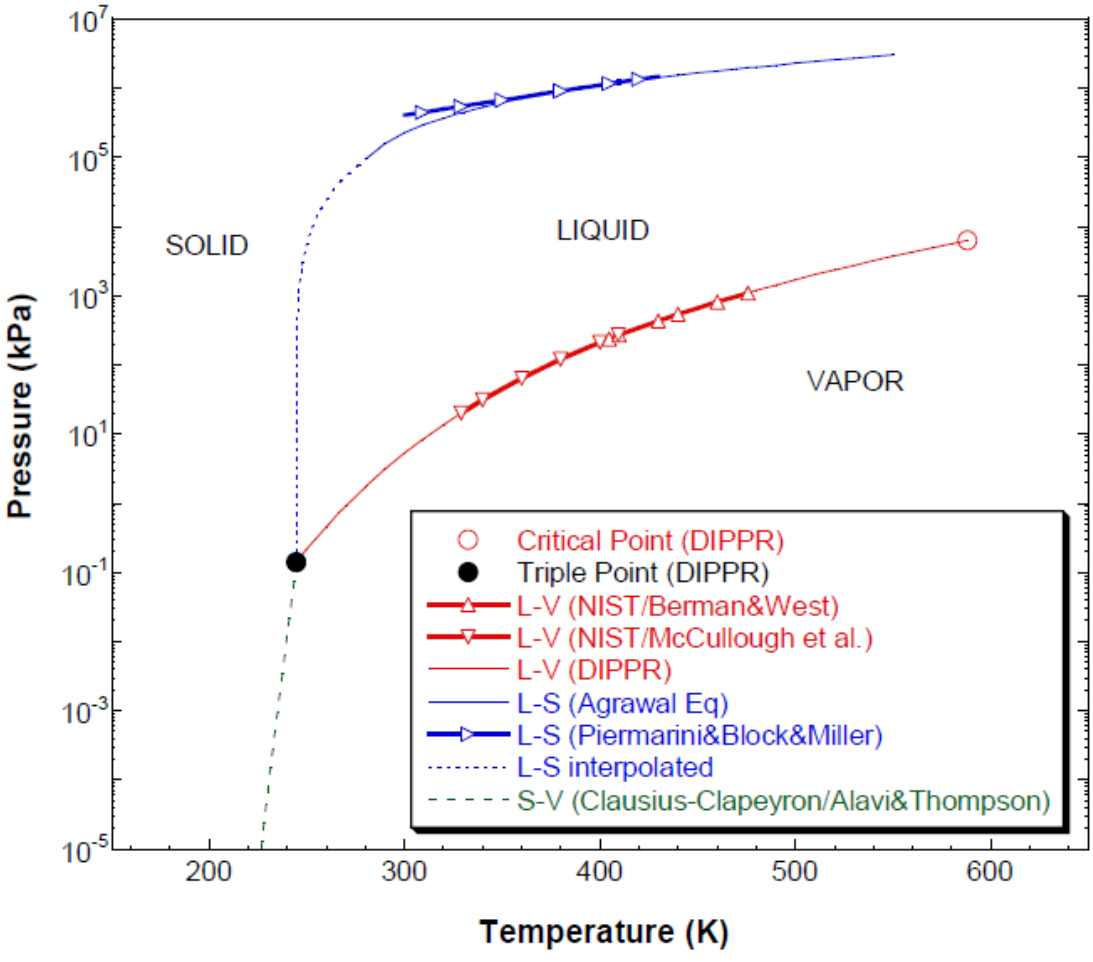

Figure 39: Phase diagram of Nitromethane

3.2.2 Condensed-phase properties

The density is calculated by a regression of data from different studies by the DIPPR project [53] using the following formula:

$$\rho = \frac{A}{B^{[1+(1-\frac{T}{C})^D]}} \tag{3.4}$$

With ρ in grams per cubic centimeter, and T in Kelvin. The coefficient and the temperature range are illustrated in table 17:

Table 17: Coefficients and temperature range for nitromethane density by DIPPR

Temperature [K]	**A**	**B**	**C**	**D**
244.60 to 588.15	1.3793	0.23918	588.15	0.29030

DIPPR project also provides a second-order polynomial for the heat capacity of the liquid in $J/kmol - K$:

$$c_p = A + BT + CT^2 \tag{3.5}$$

With the coefficients listed in the following table:

Table 18: Coefficients and temperature range for heat capacity of liquid nitromethane

Temperature [K]	**A**	**B**	**C**
244.60 to 473.15	1.1627e5	-135.30	0.34500

3.2.3 Gas-phase properties

Based on the rules refined by Kee, Coltrin, and Glarborg [54] and on rigorous kinetic theory, the molecular parameters were calculated from the the viscosity correlation given by DIPPR:

$$\propto = \frac{AT^B}{1 + \frac{C}{T}} \tag{3.6}$$

With T temperature in Kelvin, the coefficients A, B, and C listed in table 19, and the resulting viscosity given in Pa-s. In figure 40 are shown the literature viscosity data with the curve fit of equation above. The derived parameters are shown in table 20.

Table 19: Coefficients for vapor viscosity

Coefficients	**Value**
A	4.0700e-7
B	0.64850
C	367.50

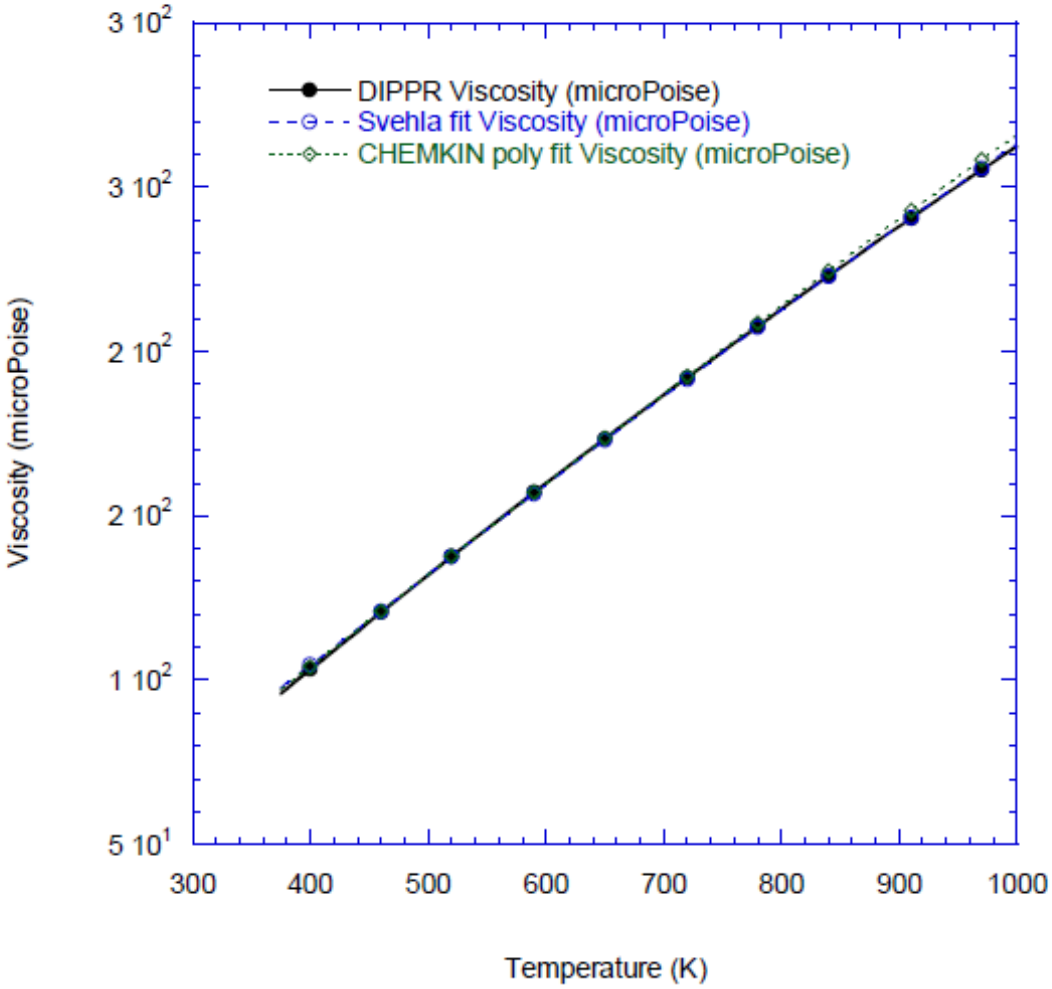

Figure 40: Comparison between literature data and polynomial approximation for vapor viscosity

Table 20: Molecular transport parameters for nitromethane

Species	**Geometry**	ϵ/k_B	σ	$\overline{\alpha}$	α	Z_{rot}
CH_3NO_2	2	486.076	4.271	3.46	0.000	2.000

Where:

- ϵ/k_B is the Lennard-Jones potential well depth, in Kelvin.
- σ is the Lennard-Jones collision diameter, in Angstroms.
- $\overline{\propto}$ is the dipole moment, in Debye.
- α is the polarizability, cubic Angstroms.
- Z_{rot} is the rotational relaxation collision number.

Another important property in combustion modeling is the gas-phase thermal conductivity. DIPPR project provides the following function in order to calculate it:

$$\lambda = \frac{AT^B}{1 + \frac{C}{T} + \frac{D}{T^2}} \tag{3.7}$$

Where T is the temperature in Kelvin, the coefficients A, B, C, and D are illustrated in table 21, and the thermal conductivity is given in W/m-K.

Table 21: Coefficients for the gas-phase thermal conductivity of nitromethane

Coefficient	**Value**
A	3.1350e-05
B	1.1119
C	-91.600
D	1.2800e05

3.3 Nitromethane combustion

A detailed kinetic model developed by Melius [55] was used in a model simulation to understand the processes occurring in the nitromethane combustion. In particular, it was used the Chemkin-II code [56] developed at Sandia National Laboratories with the PREMIX program [57] to calculate the gas-phase species and temperature profiles for steady, laminar, premixed flames. In figure 41 is shown the reaction mechanism diagram of Melius for carbon-containing and nitrogen-containing species during the ignition of nitromethane [58].

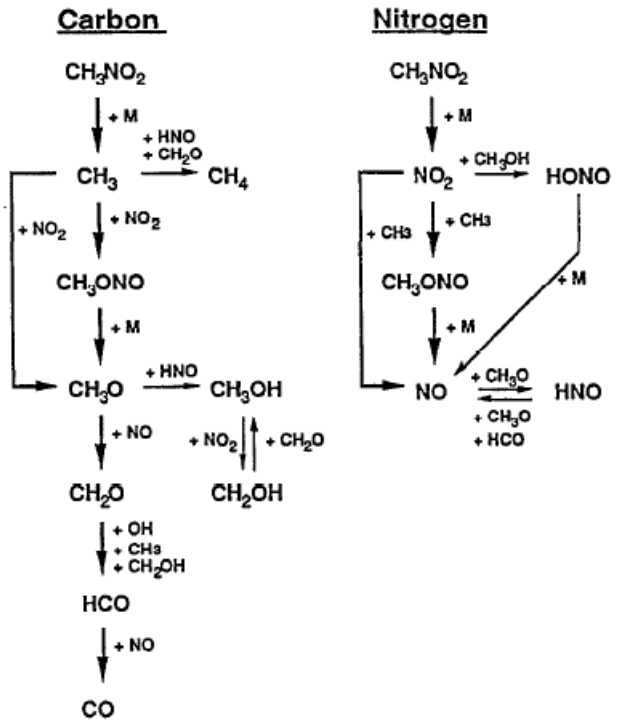

Figure 41: Reaction mechanism diagram of Melius

The results of the model simulation show that the major species in the final product are H_2O and CO at mole fractions of 0.28. H_2 is about 0.22, N_2 0.16, and CO_2 is 0.05. The minor species show up as reaction intermediates, appearing in the concentrated reaction region, then disappear. In the minor species, the most present is NO with a mole fraction of 0.19, followed by HCN with 0.05.

In the beginning, with the nitromethane decomposition a large amount of NO is formed, along with the formation and rapid depletion of CH_2O and NO. Then, in order to provide further heat release and bring the flame to the final temperature, HCN is

formed and consumed with the remaining NO to N_2 conversion. The species in this phase of the simulation are slightly different from the ones found by Melius at low pressures. The difference is that Melius found CH_2O to be an important intermediate product, but here instead was found in low concentrations, with NO and HCN the most prevalent species. These results are illustrated in figure 42 [58].

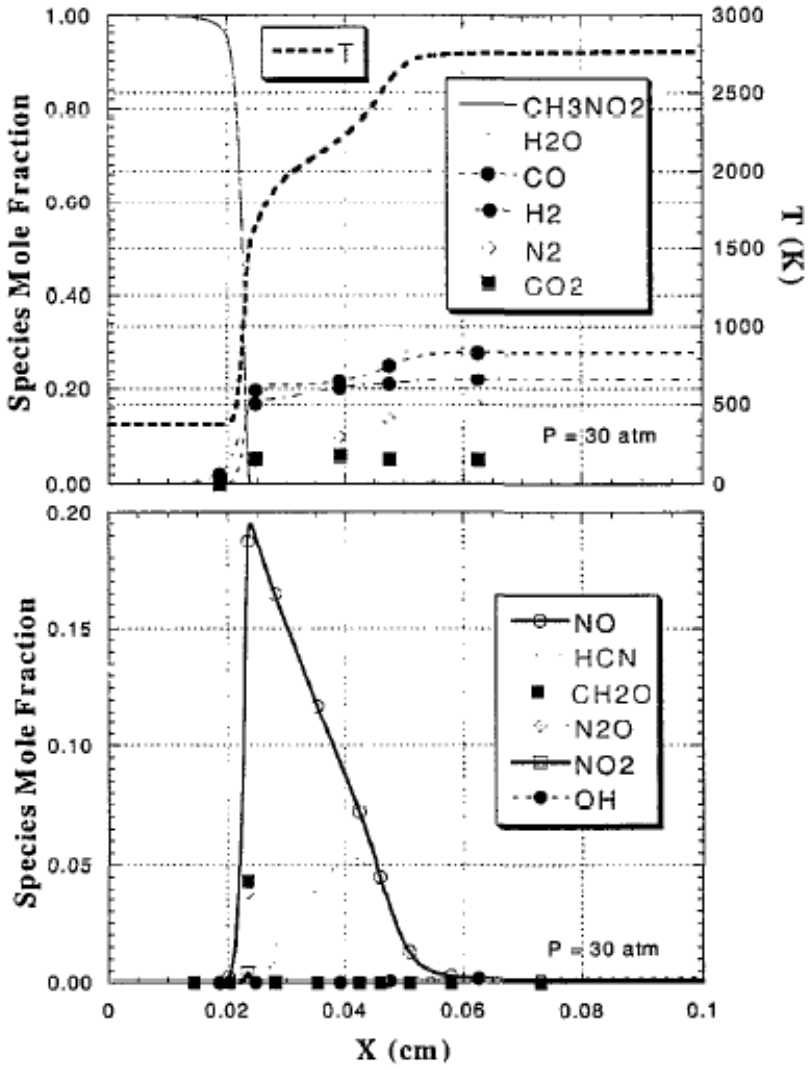

Figure 42: Calculated temperature and mole fraction profiles of major and minor species in the nitromethane flame

Based on different studies, burning rate measurements were made over a range of conditions for static and feeding tests, and three pressure regimes were found [49]:

$$r_b(mm/s) = 0.173[P(MPa)]^{1.17} \qquad (3 < P \leq 15MPa) \tag{3.8}$$

$$r_b(mm/s) = 0.009[P(MPa)]^{2.33} \qquad (15 < P \leq 70MPa) \tag{3.9}$$

$$r_b(mm/s) = 4.153[P(MPa]^{0.86} \qquad (70 < P \leq 170MPa) \tag{3.10}$$

A detailed model for linear regression was developed and presented in [49]: it considers a one-dimensional behavior with surface vaporization and detailed gas-phase kinetics based on the mechanism of Yetter [59] combined with the nitromethane decomposition of Glarborg, Bendtsen, and Miller [60]. In figure 43 is possible to see the predicted burning rates having a good agreement with measured rates up to the change in burning rate exponent at 15 MPa.

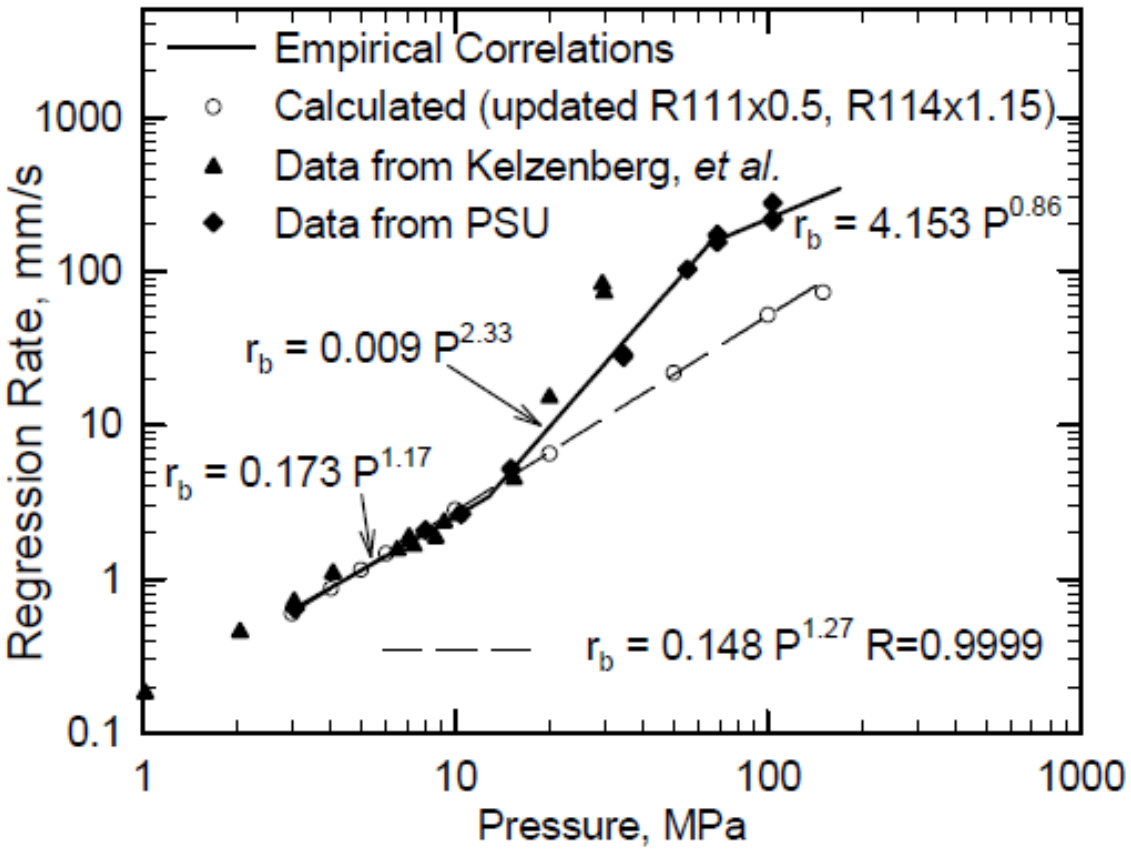

Figure 43: Calculated burning rate over a range of pressures

3.4 Nitromethane in rocket propulsion

Thanks to the work made by Federico Berto in his thesis [51], we can see a panoramic on nitromethane in rocket propulsion in figure 44.

Source	Date	Oxidizer	Additives	Catalyst	Pressure	Sizes	Notes
Zwicky et al. [46]	1944	Oxygen	Nitroethane	Cerium oxide	20 bar		Spark plug or auxiliary flame evaluated as ignition mechanism
Kindsvater [91]	1951	(self-decomposition)			< 27 atm		Too slow
Kindsvater [91]			di-tert-butyl peroxide (DTBP) or chloral				2X increase in decomp rate
Kindsvater [91]				Stainless steel			40X increase in decomp rate
Neofuel mix [66]	1954		79 % nitromethane, 19 % ethylene oxide, and 2 % chromium acetyl acetonate				
Benziger [82]	1982			NiO and Cr2O3 nanoparticles			Enhanced comb at low pressure
Solid rocket patent, Carden [94]	1998		methanol				Methanol employed only in pilot flame
Wu at al. [84]	2009		pilot flame using oxygen and methane or hydrogen		> 20 atm for 99% chemical efficiency	< 1 cm	Chem eff. > 99% if p > 20 atm
Top fuel dragster [96]		1.7 kg of ambient air per 1 kg of NM	Methanol to reduce knocking		~ 34 atm		90% NM max concentration; rest is methanol
Yang et al. [85]	2019	Air			~ 15 atm		Auto-ignition after rapid compression
Zhang et al. [77]	2011	Air					Minimum Ignition energy (MIE) = 0.7 mJ
Yetter at al.[5]	2007	Oxygen		Methane/Air auxiliary flame	1 atm	~ 10 mm	Min. 6% O_2 vol. to maintain combustion

Figure 44: Panoramic of nitromethane applications and studies

The first test of nitromethane as rocket monopropellant was made by Crocco in the '30s in Italy. The experiment showed good results in determining decomposition and sensitivity at both atmospheric and high pressures (60-90 atm) until an explosion and lack of founds ended it. Until the end of World War II no other experiments were recorded, then the Aerojet Corporation, the Jet Propulsion Laboratory (JPL), and the Navy Engineering Experiment Station (EES) at Annapolis started to investigate its use as monopropellant, recognizing its potential as relatively non-toxic, high-energy and storable propellant [49]. In 1944 Zwicky et al. [61] developed a monopropellant nitromethane-fueled rocket, with a chamber pressure of 20 bar, using nitroethane as additive up to 0.5 molar fraction in order to reduce the chamber temperature from 2640 K to 1570 K, and at the same time lowering the achievable specific impulse from 216.5 to 179 seconds. The system used a catalytic material, cerium oxide, covering the walls of the chamber and the nozzle, in order to achieve self-combustion of the nitromethane.

The U.S. Army conducted post-war investigations to use nitromethane in rockets to launch buzz bombs. In order to overcome the ignition difficulties, a torch-type igniter was used. A big issue was the unwanted initiation in the injector system under certain condi-

tions, even using certain additives to reduce the detonation sensitivity. Rocket testing was extensive, with over 200 runs made at chamber pressures ranging from approximately 700 to 1000 psi [49]. The U.S. Navy conducted some tests in 1951 [62]. The main issue was the slow decomposition rate at low pressures (<400 psia), needing a longer characteristic length of the chamber for stable operations. In order to avoid that, the addition of di-tert-butyl peroxide (DTBP) or chloral, and the use of stainless steel as catalyst achieved a 40-fold increase in the decomposition rate.
Other works at Aerojet in 1954, with the goal of solve ignition and combustion stability issues, developed a mixture called "Neofuel" containing 79 % nitromethane, 19 % ethylene oxide, and 2 % chromium acetyl acetonate [49]. A NM/ethylene oxide blend, with a 3 to 50% volume fraction of ethylene oxide was studied by Milton Wilson in 1962 [63]. This blend should keep the positive propulsive benefits of nitromethane, while reducing its explosivity, with a 5% ethylene oxide sufficient to inhibit any sensitivity to shock or propagation of detonation.

To achieve nitromethane stable combustion two ways were used: the use of Neofuel, and the use of an ammonium perchlorate and P-BAN polymer binder as solid fuel, presented in 1998 [64]. In this work, a mixture of liquid nitromethane and methanol was injected in a sustainer motor. The aim of the methanol is to reduce the sensitivity level of nitromethane, in order to prevent the detonation in the injection nozzle or into the fuel tank. The pressure in the combustion chamber could be adjusted controlling the flow rate of the blend, helping to regulate the burn rate of the main fuel. A subcentimeter-size range combustion chamber using nitromethane as monopropellant was tested by Wu et al. [65]. Because the specific area of the wall film increases as the combustor volume decreases, a liquid film can offer a surface area for vaporization that is as large as that of a vaporizing spray [51]. It is possible to use the heat transferred to the wall for fuel film vaporization, thus the use of atomizer to produce submicron-scale droplets could not be needed for liquid-fueled combustion in meso and microscale combustors.

4. Designing procedures of the thruster

In the following chapter are presented the initial parameters, the steps and the considerations made in order to design the nitromethane MEMS thruster. The main goal of this work was to design a micro thruster made of Silicon and operating with nitromethane as monopropellant, capable of delivering a certain thrust at a certain pressure, both predetermined.

The first step of the designing was to choose these two parameters and the expansion ratio of the nozzle ϵ. The choice of the thrust is completely arbitrary, but it will influence every aspect of the thruster. The choice of the pressure is also arbitrary but limited due to the difficulties of the ignition of nitromethane at low pressure. The expansion ratio was chosen based on the experimental results presented in [66], indicating that for micronozzles there are no benefits in increasing the ratio over a certain value, unlike the macroscale counterpart. This results came from the fact that MEMS nozzles are planar, with a fixed height, so the cross section only grows linearly with nozzle width, not with the square as is the case for rotational nozzles, preventing the realization of high ϵ nozzles.

To evaluate the performances of a thruster and achieve an accurate design, the thrust itself is not enough, but more parameters are needed. In particular, a fundamental parameter is the effective exhaust velocity c, linked to the thrust and expressible by:

$$S = \dot{m}c \tag{4.1}$$

$$c = c^* c_F \tag{4.2}$$

where c^* expresses the quality of the combustion inside the chamber, and c_F tells how good the nozzle work. They are defined by the following expressions:

$$c^* = \frac{1}{\Gamma}\sqrt{\frac{T_c}{M_c}} \tag{4.3}$$

$$c_F = \Gamma\sqrt{\frac{2k}{k-1}[1-(\frac{p_e}{p_c})^{(\frac{k-1}{k})}]} + \frac{A_e}{A_g}(\frac{p_e}{p_c} - \frac{p_a}{p_c}) \tag{4.4}$$

with:

- Γ contains terms of the molecule constant $k = c_p/c_v$
- T_c is the temperature in the combustion chamber
- M_c is the molecular mass of the product inside the combustion chamber
- p_c is the pressure inside the combustion chamber
- p_e is the pressure just before the end of the nozzle
- p_a is the pressure in the external ambient
- A_e is the exit area of the nozzle
- A_t is the throat area of the nozzle
- $\dot{m}$ is the mass flow

Dividing c by the gravity acceleration allows to define another important parameter measured in seconds called specific impulse by:

$$I_{sp} = \frac{c}{g_0} \tag{4.5}$$

from which is possible to define more parameters that allow to have a better understanding of the system: the total impulse, the medium specific impulse, the specific system

impulse and the volumetric specific impulse:

$$I_{tot} = \int_0^{t_b} S dt \tag{4.6}$$

$$I_{sp_{medium}} = \frac{I_{tot}}{m_{prop_{tot}} g_0} \tag{4.7}$$

$$I_{ss} = \frac{I_{tot}}{m_{tot} g_0} \tag{4.8}$$

$$I_\rho = \frac{I_{tot}}{V_{prop} g_0} = I_{sp}\rho \tag{4.9}$$

Where t_b is the burning time, m_{tot} is the total mass of the propulsive system, $m_{prop_{tot}}$ is the total mass of propellent, V_{prop} is the volume of the propellent and ρ is its density.

The above parameters for this work were calculated using a thermochemistry program called "CproPEP", which requires in input the propellant, the chamber pressure and the expansion ratio of the nozzle.

4.1 Combustion chamber and converging-diverging nozzle

The first step consists in calculating the mass flow rate necessary to achieve the desired thrust with:

$$\dot{m} = \frac{S}{I_{sp} g_0} \tag{4.10}$$

From the mass flow rate is then possible to derive the throat area of the nozzle:

$$A_t = \frac{\dot{m} c^*}{p_c} \tag{4.11}$$

Since the throat area in MEMS nozzle is not axisymmetric, but has a square or rectangular shape (due to micro-fabrication limitations), the throat width w_t can be obtained simply by taking the square rooting of A_t. Another option would be to choose the w_t arbitrarily and then calculate the height of the throat h_t by:

$$h_t = \frac{A_t}{w_t} \tag{4.12}$$

Due to its planar shape, and to make the micro-fabrication easier, both the combustion chamber and the nozzle have the same height, so $h_t = h_c$. For a given expansion ratio ϵ and a fixed height is possible to define the exit area A_e of the diverging part of the nozzle and its width w_e:

$$A_e = \epsilon A_t \tag{4.13}$$

$$w_e = \frac{A_e}{h_t} \tag{4.14}$$

In figure 45 is shown a classical converging-diverging nozzle.

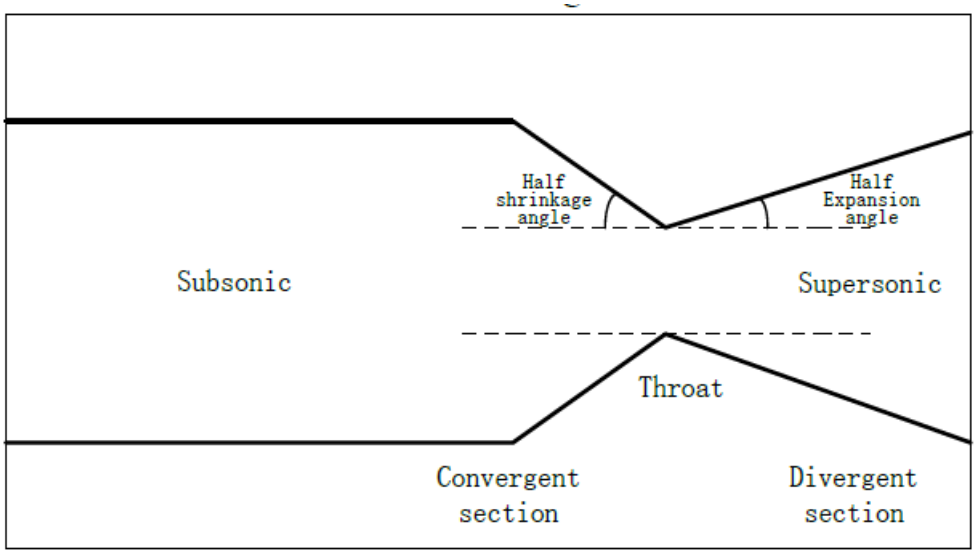

Figure 45: Schematic view of a converging-diverging nozzle

The value chosen for the half expansion angle θ_{div} was 30° due to considerations on micronozzle. In the study presented in [67] a notable reduction in thrust was recorded

as the expander half angle is increased above 30°, because the flow follows the walls in the expander and thus a sizable component of the velocity vector exits the nozzle in the transverse direction, resulting in a significant reduction of axial momentum flux and a corresponding decline in thruster performance. Instead, for smaller half angles viscous forces acting over the lengthened expander section begin to dominate nozzle performance. The results of the cited study are graphed in figure 46.

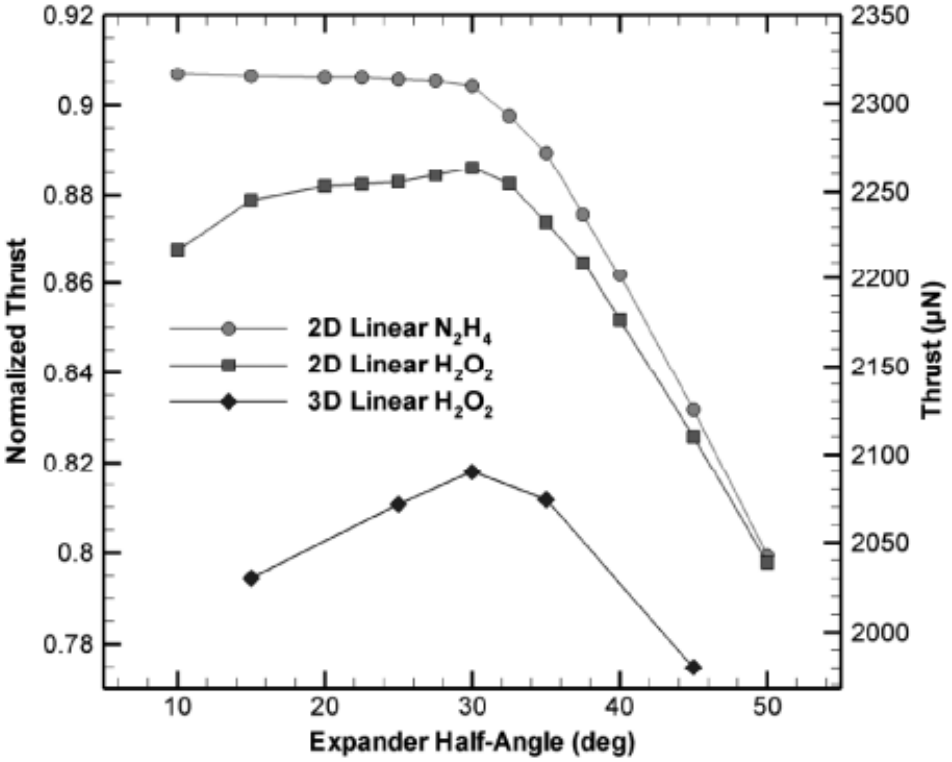

Figure 46: Performance results for 2D and 3D simulations of the NASA/GSFC microthruster nozzle operating at steady-state with adiabatic walls (cita design consid...)

The value of the converging half angle θ_{conv} was chosen to be a standard 45°. The lenght of the diverging section can be easily calculated by:

$$L_{\theta_{div}} = \frac{1}{2}\frac{w_e - w_t}{\sin\theta_{div}} \tag{4.15}$$

In order to define the size of the chamber, the chamber width w_c was put equal to the exit nozzle width w_e. This choice allows to have a compact thruster and to make the micro-fabrication of the system easier. Now is possible to calculate the length of the

converging section of the nozzle by:

$$L_{\theta_{conv}} = \frac{1}{2}\frac{w_c - w_t}{\cos\theta_{conv}} \tag{4.16}$$

To calculate the length of the straight sections are used:

$$L_{\theta_{conv\,straight}} = 0.5\frac{w_t - w_c}{\tan\theta_{conv}} \tag{4.17}$$

$$L_{\theta_{div\,straight}} = 0.5\frac{w_e - w_t}{\tan\theta_{div}} \tag{4.18}$$

The length of the chamber is a parameter defined by the characteristic length L^*, thus by the residential time t^* [68]. Since the lack of literature data for L^* of MEMS nitromethane thruster, the only option was to calculate it from the following formula [69]:

$$L^* = \frac{\dot{m}}{\rho_g A_t}t^* \tag{4.19}$$

The characteristic length L^* is also defined as the ratio between the chamber volume and the throat area. Thus, the chamber length can be easily obtained by:

$$L^* = \frac{V_c}{A_t} \tag{4.20}$$

$$V_c = A_t L^* \tag{4.21}$$

$$A_c = w_c h_t \tag{4.22}$$

$$L_c = \frac{V_c}{A_c} \tag{4.23}$$

The last step to design the chamber was to calculate the minimum thickness of the walls to sustain the chamber pressure p_c. In order to get an estimate of it, it was used a simpler model consisting in a beam wedged with uniformly distributed load, as it's shown in figure 47:

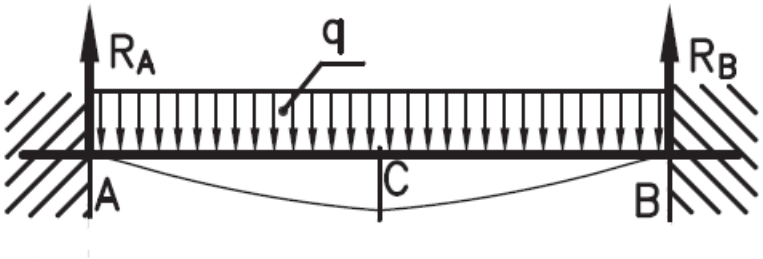

Figure 47: Beam wedged with uniformly distributed load

For the upper and below walls (the largest) we have:

$$q_{u/b} = p_c w_c \tag{4.24}$$

$$M_{C_{u/b}} = \frac{1}{24} q_{u/b} L_c^2 \tag{4.25}$$

$$t_{min_{u/b}} = \sqrt{\frac{6 M_{C_{u/b}}}{L_c Y_{strength}}} \tag{4.26}$$

Where $q_{u/b}$ is the uniformly distributed load, M_C is the momentum acting on the center of the beam, and $Y_{strength}$ is the yield strength of the material considered (Silicon in this work).
For the lateral walls the procedure is the same, but with different data:

$$q_{lat} = p_c h_t \tag{4.27}$$

$$M_{C_{lat}} = \frac{1}{24} q_{lat} L_c^2 \tag{4.28}$$

$$t_{min_{lat}} = \sqrt{\frac{6M_{C_{lat}}}{L_c Y_{strenght}}} \tag{4.29}$$

4.2 Injector

In this section are presented two possible choices for the injection of the propellant. The first one is to inject the propellant in the liquid state from the tank to the chamber; the second one is to inject the propellant in vapor state. The last one would require a heater placed in the path from the tank to the chamber in order to apply the necessary power to vaporize the liquid.
Due to the micro-fabrication of MEMS, the injector is made of the same material of the rest of the thruster (Silicon in this work), and it has a square or rectangular cross-section. Alternatively is possible to design only the exit area and use a commercially available injector.

4.2.1 Liquid state injection

In order to calculate the area of the injector, the velocity at the end of it is needed. Through the Bernoulli equation we obtain:

$$\frac{\Delta p}{\rho} = \frac{v^2}{2} \tag{4.30}$$

$$v = \sqrt{2\frac{\Delta p}{\rho}} \tag{4.31}$$

where Δp is the pressure difference across the conduit and ρ is the density of the liquid propellant.
When dealing with flows through holes, in order to assess correctly the flow rate it must be considered a discharge coefficient C_d that depends on the shape of the hole.

$$\dot{m} = C_d \rho v A_{inj} \tag{4.32}$$

From this equation is easy to calculate the exit area:

$$A_{inj} = \frac{\dot{m}}{C_d \rho v} = \frac{\dot{m}}{C_d \sqrt{2\rho \Delta p}} \tag{4.33}$$

Once the area is known, due to its square cross section, is possible to define the side l_{inj} simply by making the square root:

$$l_{inj} = \sqrt{A_{inj}} \tag{4.34}$$

4.2.2 Vapor state injection

The first step in order to design the injector for a vapor state propellant is to calculate the power needed to vaporize it. Vaporization can be achieved in two ways for this work: heating through an external power source, or heating through a regenerative cooling system.
The first simply consists in using an external source to apply the power needed to bring the propellant from the liquid state to the vapor state. The second consists in flowing some or all the propellant through tubes or channels around the combustion chamber and the nozzle to cool the system, and then injecting it into the chamber. The power needed to vaporize it will be provided by the heat released by the combustion in the combustion chamber.

The power needed to vaporize a certain mass flow $\dot{m}$ is define by:

$$P_{vap} = \dot{m} \Delta H_{tot} \tag{4.35}$$

where ΔH_{tot} is the total enthalpic jump and it can be divided in two parts, as we can

see in figure 48:

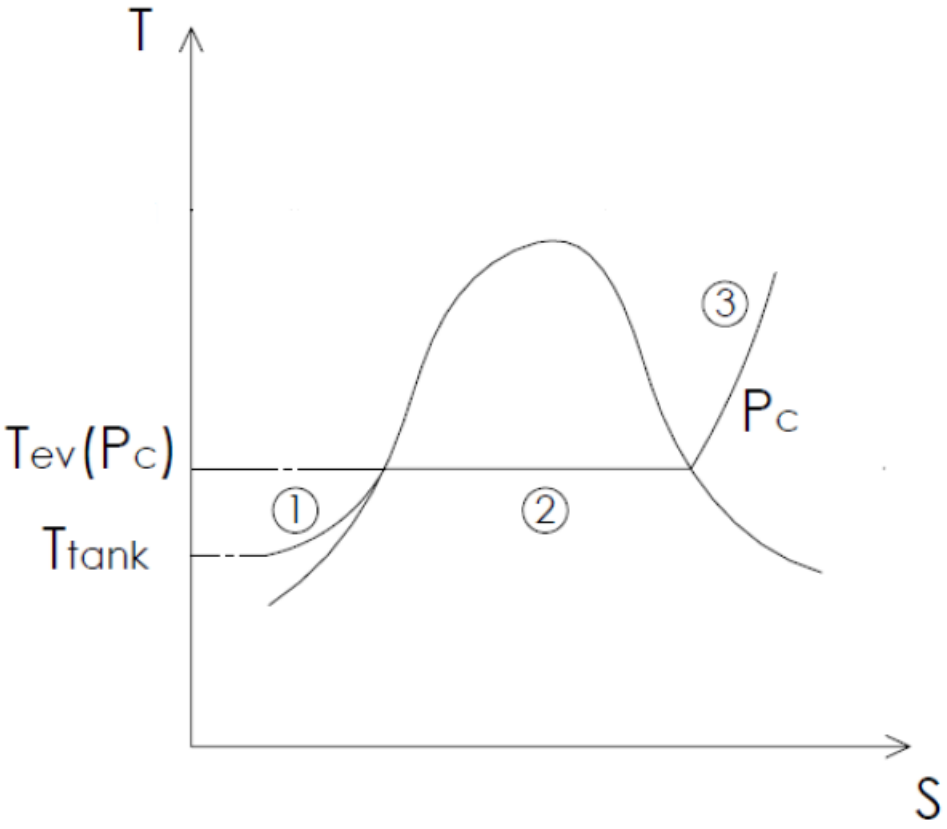

Figure 48: T-s diagram [51]

The tract number 1 in figure 48 is needed to take the propellant from its temperature in the tank T_{tank} to its saturation temperature T_{sat} at a certain pressure p_c. The enthalpic jump for this tract and the power needed are define by:

$$\Delta H_{liq} = c_p(T_{sat} - T_{tank}) \tag{4.36}$$

$$P_{liq} = \dot{m}\Delta H_{liq} \tag{4.37}$$

where c_p is the constant-pressure specific heat of liquid nitromethane, calculated as an average value between T_{tank} and T_{sat}.

The second tract is the one resposible for taking the propellant from a saturated liquid state to a saturated vapor state. The enthalpic jump ΔH_{vap} in this tract is calculated from the following formula, obtained from [51]:

$$\Delta H_{vap} = Ae^{-\beta T_r}(1 - T_r)^{\beta} \tag{4.38}$$

where A and β are two coefficients, and T_r is the reduced temperature defined by the ratio between the considered temperature and the critical temperature of the propellant.

Now is possible to obtain the total power needed to vaporize the propellant by:

$$P_{tot} = \dot{m}\Delta H_{tot} = \dot{m}(\Delta H_{liq} + \Delta H_{vap}) \tag{4.39}$$

In some cases can be useful to heat up the vapor further, into the superheated steam zone. This zone is represented by the number 3 in figure 48. This overheating can also be inevitable in the regenerative cooling if the power coming from the combustion process in the chamber is more than the power needed to vaporize the cooling liquid.
This process can be used to bring the temperature of the propellant closer to its auto-

ignition temperature. In this case, the equation 4.39 will become:

$$P_{tot} = \dot{m}(\Delta H_{liq} + \Delta H_{vap} + \Delta H_{a-i}) \tag{4.40}$$

where ΔH_{a-i} is the enthalpic jump to bring the temperature from T_{sat} to the auto-ignition temperature T_{a-i}:

$$\Delta H_{a-i} = H(T_{a-i}) - H(T_{sat}) \tag{4.41}$$

Once obtained the power needed to vaporize the propellant, is possible to define the area of the injector. The first step is, again, to calculate the velocity at the end of the injector:

$$p_0 = p_c + \Delta p \tag{4.42}$$

$$M = \sqrt{\frac{2}{k-1}[(\frac{p_0}{p_c})^{(\frac{k-1}{k})} - 1]} \tag{4.43}$$

$$v = M\sqrt{kRT} \tag{4.44}$$

with M the Mach number, and R the specific gas constant.
Now is possible to define the exit area of the injector and its side by:

$$A_{inj} = \frac{\dot{m}}{\rho_g C_d v} \tag{4.45}$$

$$l_{inj} = \sqrt{A_{inj}} \tag{4.46}$$

4.3 Heat exchanges

In order to evaluate the heat exchanges and develop a cooling system, it's needed to calculate the heat produced by the combustion and that spreads through the chamber.
The first step is to evaluate the viscosity of the products of the combustion using the Wilke mixing law:

$$\mu = \sum_i \frac{X_i \mu_i}{X_i + \sum_{j,j\neq i} X_j \Phi_{ij}} \tag{4.47}$$

where X_i are the species molar fractions, and Φ_{ij} are viscosity interaction coefficients, given by:

$$\Phi_{ij} = \frac{1}{4}[1 + (\frac{\mu_i}{\mu_j})^{(\frac{1}{2})}(\frac{M_j}{M_i})^{(\frac{1}{4})}]^2(\frac{2M_j}{M_i + M_j})^{(\frac{1}{2})} \tag{4.48}$$

where M_i and M_j are molecular weights of species i and j.

The second step is to evaluate the thermal conductivity of the combustion products by the following mixing law:

$$\lambda = \sum_i \frac{X_i \lambda_i}{X_i + \sum_{j,j\neq i} X_j \Psi_{ij}} \tag{4.49}$$

where Ψ_{ij} is the following interaction coefficient:

$$\Psi_{ij} = \Phi_{ij}[1 + \frac{2.41(M_i - M_j)(M_i - 0.142M_j)}{(M_i + M_j)^2}] \tag{4.50}$$

where Φ_{ij} is the viscosity interaction coefficient described in eq.4.48.

Now is possible to calculate the heat transfer coefficient α of the combustion products using the Nusselt number:

$$Nu = f(Re, Pr) \tag{4.51}$$

$$\alpha_{prod} = \frac{Nu\lambda}{L} \tag{4.52}$$

where Re is the Reynolds number, Pr is the Prandtl number, and L is a characteristic lenght.

Is possible to evaluate the heat exchanges considering the walls of the chamber using the global heat transfer coefficient defined by:

$$K = \frac{1}{\frac{1}{\alpha_{prod}} + \frac{s}{\lambda_{Si}}} \tag{4.53}$$

where s is the thickness of the wall, and λ_{Si} is the thermal conductivity of the walls material (in our case, Silicon).
The heat spreads through the camber is derived by:

$$Q = KA\Delta T \tag{4.54}$$

where A is the considered area, and ΔT is the difference in temperature between the considered elements.

Regenerative cooling

Regenerative cooling is a configuration in which the chamber and/or the nozzle are surrounded by channels in which the propellant flows in order to cool down the system. The heated propellant is then fed into an injector or directly into the chamber. This configuration allows at the same time to cool down the system and heat up the propel-

lant, in order to keep the system walls at a sufficiently low temperature and to save power.

If the heat through the system is high enough, the liquid in the channels may undergo state changing. If this happens, the heat transfer coefficient must be calculate for every state (liquid, boiling, vapor). It's also important for a given channel length to calculate how much of that length is necessary to bring the liquid to saturation, then to vaporize it, and then to overheat the vapor. This process is needed to understand how much heat the coolant liquid can absorb.

To calculate the channel length necessary to bring the liquid to its saturation temperature is possible to use the following equation:

$$Q_{sat} = \alpha_{liq} A (T_w - T_f) \tag{4.55}$$

where Q_{sat} is the power needed to bring the liquid to its saturation temperature, α_{liq} is the heat transfer coefficient of the liquid, A is the exchange area, T_w is the wall temperature and T_f = (T_{sat} - T_{amb})/2. From A is possible to get the length sought.

The heat transfer coefficient must be calculate again if the liquid starts to boil. To achieve that is possible to use Chen's correlation [70]:

$$h_{tp} = F h_L + S h_{FZ} \tag{4.56}$$

With:

$$h_{FZ} = 0.00122 \cdot \frac{k_L^{0.79} c_{p_L}^{0.45} \rho_L^{0.49} g_c^{0.25}}{\sigma^{0.5} \mu_L^{0.29} H_{vap}^{0.24} \rho_V^{0.24}} \cdot \Delta T \cdot \Delta P \tag{4.57}$$

$$F = (\frac{1}{X_{tt}} + 0.213)^{0.736} \tag{4.58}$$

$$\frac{1}{X_{tt}} = (\frac{x}{1-x})^{0.9} (\frac{v_v}{v_L})^{0.5} (\frac{\mu_v}{\mu_L})^{0.1} \tag{4.59}$$

$$S = \frac{1}{1 + 0.00000253 \cdot Re_{tp}^{1.17}} \tag{4.60}$$

where:

- h_{FZ} is the nucleate pool boiling heat transfer coefficient by Forster and Zuber.
- k_L is the liquid thermal conductivity.
- c_{p_L} is the heat capacity of the liquid.
- ρ_L and ρ_V are the liquid and vapor densities.
- v_v and v_L are the specific volume of the liquid and the gas.
- x is the quality vapor.
- σ is the vapor-liquid surface tension.
- μ is the viscosity of the liquid.
- g_c is the gravitational conversion factor.
- $\Delta T = T_w$ - T_{sat}.
- ΔP is the difference in vapor pressure corresponding to ΔT.
- H_{vap} is the enthalpy of vaporization.
- X_{tt} is the Lockhart-Martinelli parameter.
- $Re_{tp} = Re_L \cdot F^{1.25}$.

With the new heat transfer coefficient is possible to calculate how much length of the channel is needed for the boiling phase with the equation 4.55, just by changing α_{sat}, T_f, and Q_{sat} with h_{tp}, T_{sat}, and Q_{vap} (heat needed to vaporize the liquid).
The new heat transfer coefficient h_{tp} depends on vapor quality, so a discretization and an iterative process are needed to calculate the length.

The last step is to understand if the channel is long enough for the vapor to overheat. For a given channel length $L_{channel}$ we can derive the remaining length after boiling phase:

$$L_{o/h} = L_{channel} - L_{sat} - L_{boiling} \tag{4.61}$$

with L_{sat} the channel length in which the liquid reach the saturation, and $L_{boiling}$ the length in which boils.
Discretizing $L_{o/h}$ and using the following equations is possible to calculate the heat exchanged in the remaining length, and the final temperature of the vapor:

$$Q_{gas_i} = \alpha_{gas} A (T_w - T_{gas_i}) \tag{4.62}$$

$$T_{gas_{i+1}} = \frac{Q_{gas_i}}{\dot{m} c_{p_{gas}}} + T_{gas_i} \tag{4.63}$$

5. Results and conclusions

In the following chapter are presented the numerical results and considerations for the preliminary sizing of the MEMS thruster. The equations used are the ones illustrated in chapter 4.

5.1 Preliminary design

As discussed in the previous chapters, the main goal of this work is to realize a preliminary design of a MEMS thruster made of Silicon, operating with nitromethane as monopropellant, capable of delivering 0.1 N of thrust, with a 25 bar pressure in the combustion chamber. In table 23 are presented some properties of Silicon.

Table 22: Initial requirements for the thruster

Parameter	**Value**	**Unit**
Thrust, S	0.1	N
Pressure, p_c	25	bar

Table 23: Silicon properties

Parameter	**Value**	**Unit**
Density	2.329	g/cm^3
Young's modulus	150	GPa
Thermal conductivity	149	$W/m \cdot K$
Specific heat capacity	19.79	$J/mol \cdot K$
Melting point	1687	K
T_w	900	K

where T_w is the maximum acceptable temperature of the silicon walls.

5.1.1 Combustion chamber and nozzle

Using the equations illustrated in section 4.1, we can obtain the values presented in the following table 24:

Table 24: Combustion chamber and nozzle dimensions

Parameter	Notation	Value	Unit
Mass flow	$\dot{m}$	3.664e-05	Kg/s
Throat area	A_t	2.243e-08	m^2
Throat width	w_t	80e-6	m
Throat height	h_t	2.804e-04	m
Expansion ratio	ϵ	20	/
Exit nozzle area	A_e	4.487e-07	m^2
Exit nozzle width	w_e	0.0016	m
Diverging semi-angle	θ_{div}	30	$^\circ$
Converging semi-angle	θ_{conv}	45	$^\circ$
Diverging length	L_{div}	1.5e-03	m
Converging length	L_{conv}	1.1e-03	m
Chamber area	A_c	4.487e-07	m^2
Chamber width	w_c	0.0016	m
Characteristic length	L^*	6.56e-02	m
Chamber volume	V_c	1.472e-09	m^3
Chamber length	L_c	3.3e-03	m
Minimum thickness horizontal walls	$t_{min_{u/b}}$	1.410e-04	m
Minimum thickness vertical walls	$t_{min_{lat}}$	5.904e-05	m

Regarding the nozzle, its expansion ratio (as already discussed in the previous chapter) was chosen considering the micro-nozzle performances since planar, micro-nozzles behave different than classical, macro scale axisymmetric nozzles. A boundary layer dominated layer is found, almost choking the nozzle, making useless adapting it for expansion into vacuum, i.e., high expansion ratio realized over the required nozzle length to ensure only moderate defection [66].
For the converging semi-angle was chosen a classic 45° value, yielding a longer converging section but more gentle reduction in cross-section, which benefits the efficiency.
For the diverging semi-angle (as already discussed briefly in the previous chapter) was chosen a 30° value based on micro-nozzle performances considerations. For large diverging angles, the flow follows the walls in the diverging section and thus a sizable component of the velocity vector exits the nozzle in the transverse direction. This results in a significant reduction of axial momentum flux and a corresponding decline in thruster performance. As the diverging angle is decreased below 30°, viscous forces acting over the lengthened diverging section begin to dominate nozzle performance. The subsonic layer acts to restrict the flow and reduce the effective exit area [67].

5.1.2 Injector

In this subsection are reported the numerical values obtained by the calculation presented in 4.2. In table 25, 26, and 27 are illustrated respectively the values for the power needed to vaporize the mass flow $\dot{m}$, the dimensions of the exit port of the injector if the nitromethane is injected in liquid state, and the dimensions of the exit port of the injector if the nitromethane is injected in vapour state.

Table 25: Enthalpy and power to vaporize $\dot{m}$

Parameter	**Value**	**Unit**
$T_{sat}(p_0)$	532.525	K
ΔH_{sat}	4.532e+05	J/kg
P_{sat}	16.610	W
ΔH_{vap}	33990	kJ/kg
P_{vap}	13.126	W
P_{tot}	29.737	W

where ΔH_{sat} and P_{sat} are the enthalpy and the power in order to bring $\dot{m}$ to T_{sat}, and

ΔH_{vap} and P_{vap} are the enthalpy and the power to vaporize $\dot{m}$.

Table 26: Values of the injectors if the NM enters as liquid

Parameter	Value	Unit
Δp	375000	Pa
v_{liq}	25.683	m/s
$A_{inj_{liq}}$	2.091e-09	m^2
$l_{inj_{liq}}$	4.573e-05	m

Table 27: Values of the injectors if the NM enters as vapour

Parameter	Value	Unit
p_o	2875000	Pa
$\rho_{gas}(T_{sat})$	51.571	kg/m^3
v_{vap}	143.367	m/s
$A_{inj_{vap}}$	8.261e-09	m^2
$l_{inj_{vap}}$	9.089e-05	m

5.1.3 Heat exchanged and regenerative cooling channels

The result of the heat exchange through the chamber using equations illustrated in chapter 4.3 are shown in the following table:

Table 28: Heat exchanged between the combustion product and the chamber

Parameter	Value	Unit
$Q_{u/b}$	26.241	W

where $Q_{u/b}$ is the heat calculated considering the upper and below walls.

A regenerative cooling system was chosen to cool down the thruster. This was achieved by a channel with a rectangular cross section in a serpentine configuration, with ninety degrees curves in order to cover as much surface as possible, placed above and below the

chamber. Inside every channel flows half of the total mass flow $\dot{m}$, then is fed directly into the chamber. The dimensions of the channels are reported in table 29:

Table 29: Dimensions of the cooling channel

Parameter	**Value**	**Unit**
Width	0.1	mm
Height	0.065	mm
Length	26.55	mm

Using the equations and the process illustrated in chapter 4.3 are obtained the following results:

Table 30: Results of the cooling system

Parameter	**Value**	**Unit**
T_{sat}	525.979	K
P_{sat}	8.073	W
L_{sat}	4.4	mm
P_{vap}	6.786	W
$L_{boiling}$	0.708	mm
$L_{o/h}$	21.4	mm
$T_{gas_{fin}}$	724.741	K
$Q_{cooling_{tot}}$	22.205	W

where $T_{gas_{fin}}$ and $Q_{cooling_{tot}}$ are the final temperature and the total heat absorbed by the coolant.
In the following figures are shown the trends of the coolant's density, velocity, temperature, and pressure losses respectively inside the channel:

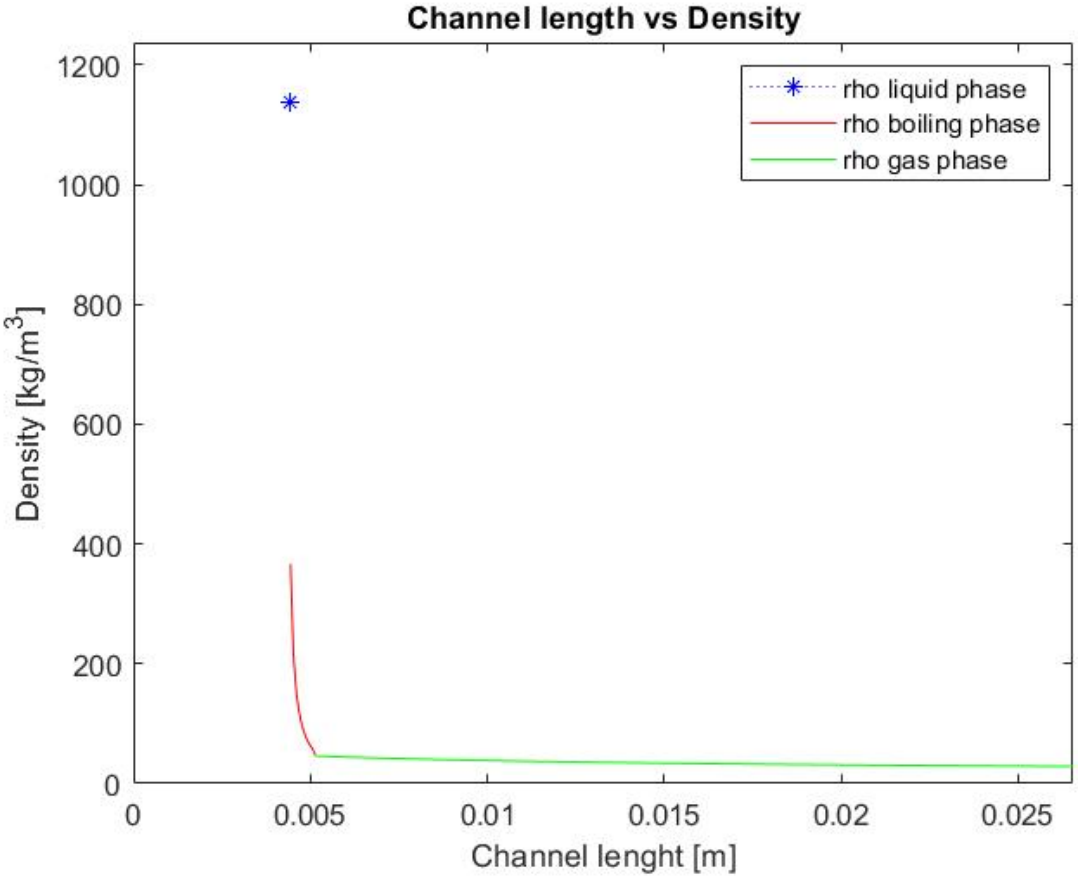

Figure 49: Coolant's density evolution inside the cooling channel

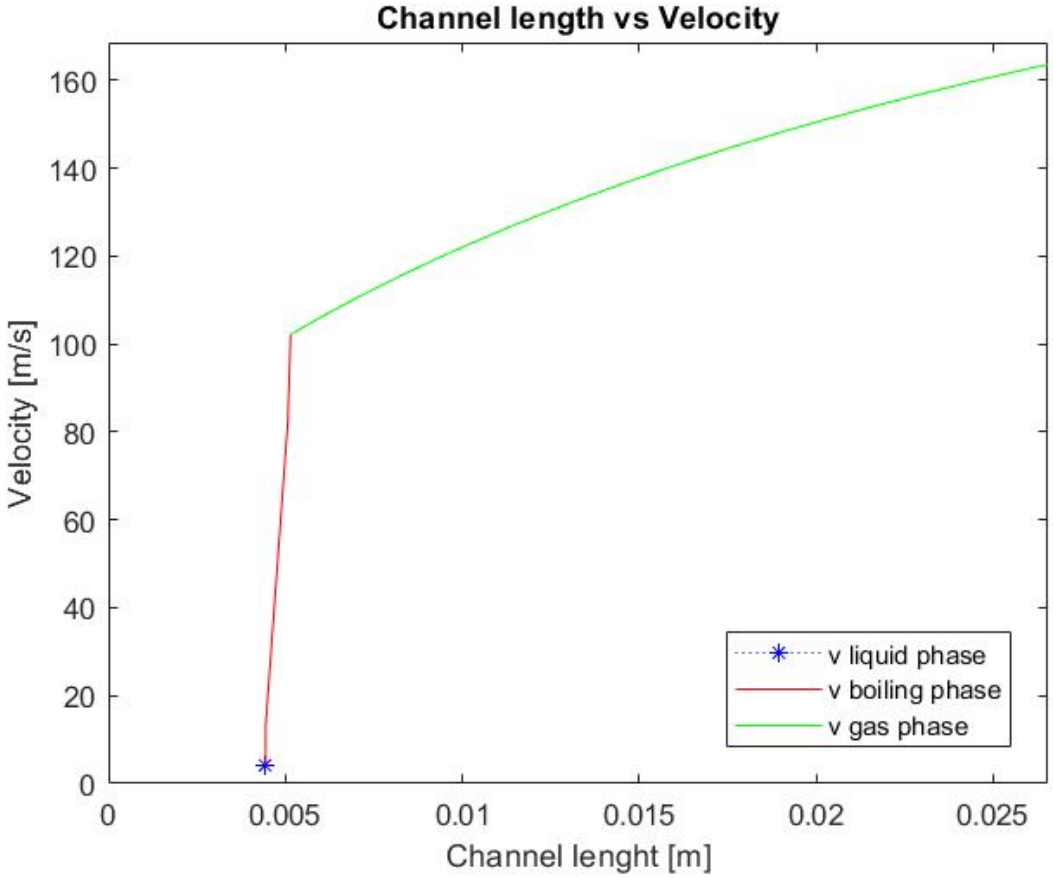

Figure 50: Coolant's velocity evolution inside the cooling channel

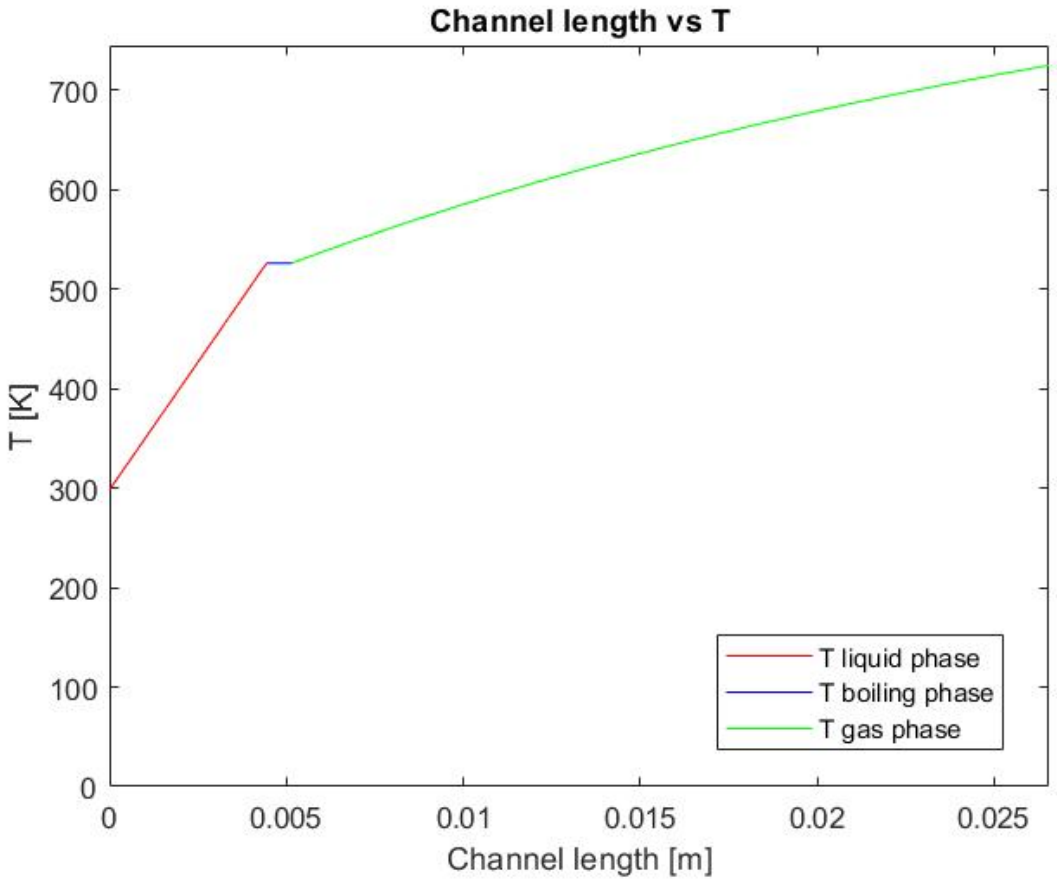

Figure 51: Coolant's temperature evolution inside the cooling channel

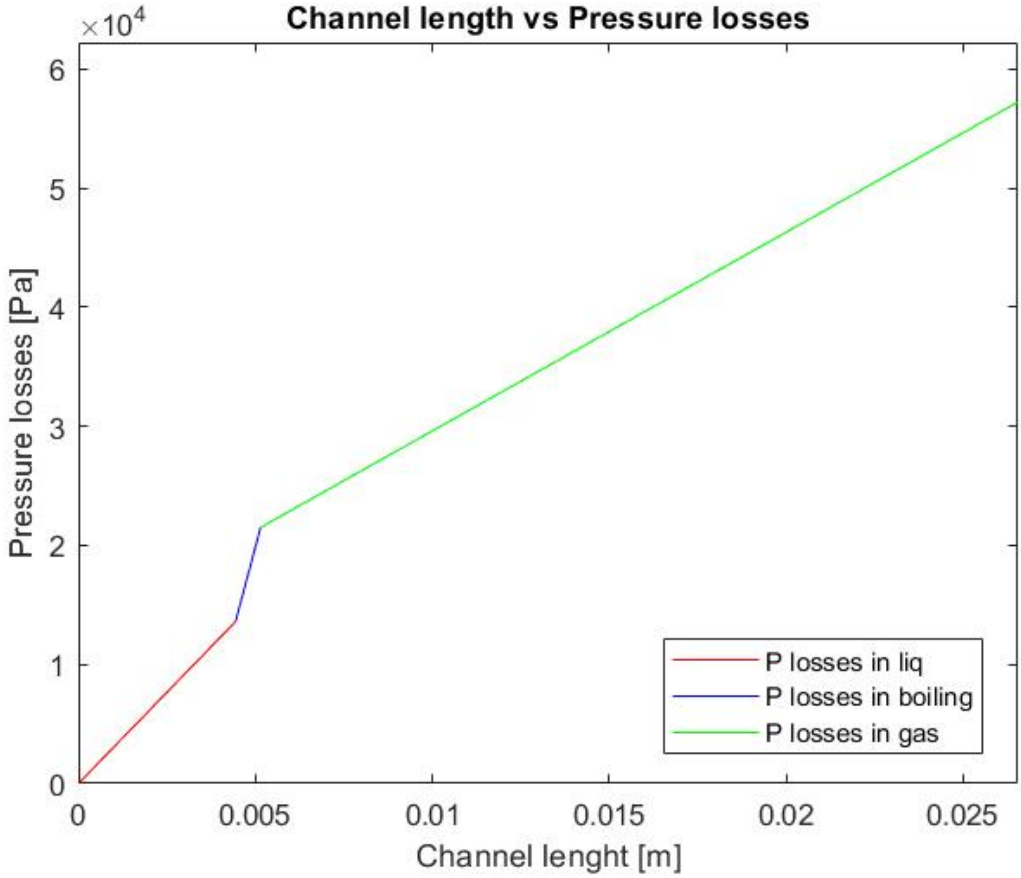

Figure 52: Pressure losses inside the cooling channel

As is possible to see from the results, there is a difference between $Q_{cooling_{tot}}$ and $Q_{u/b}$ indicating that the cooling system in this configuration is not enough to completely cool down the system. However, this is just a preliminary design, so it can and must be improved before the actual fabrication. Using a different and improved configuration of the channels and running accurate simulation of the thermal model may lead to more accurate results and to a successful cooling.

5.2 3-D model and drawings

In this section is shown the 3-D model and the technical design of the thruster realized in SolidWorks.
The thruster is made by four 0.5 millimeters Silicon wafers bounded together:

- The first wafer contains the upper cooling channel that fed the coolant directly in the chamber.
- The two wafers in the middle contain the chamber and the nozzle. Each wafer contains half of them.
- The last wafer contains the below cooling channel identical to the one above.

In figure 53 and 54 are shown the 3-D models of the wafer containing half chamber and half nozzle, and of the wafer containing the cooling channel.

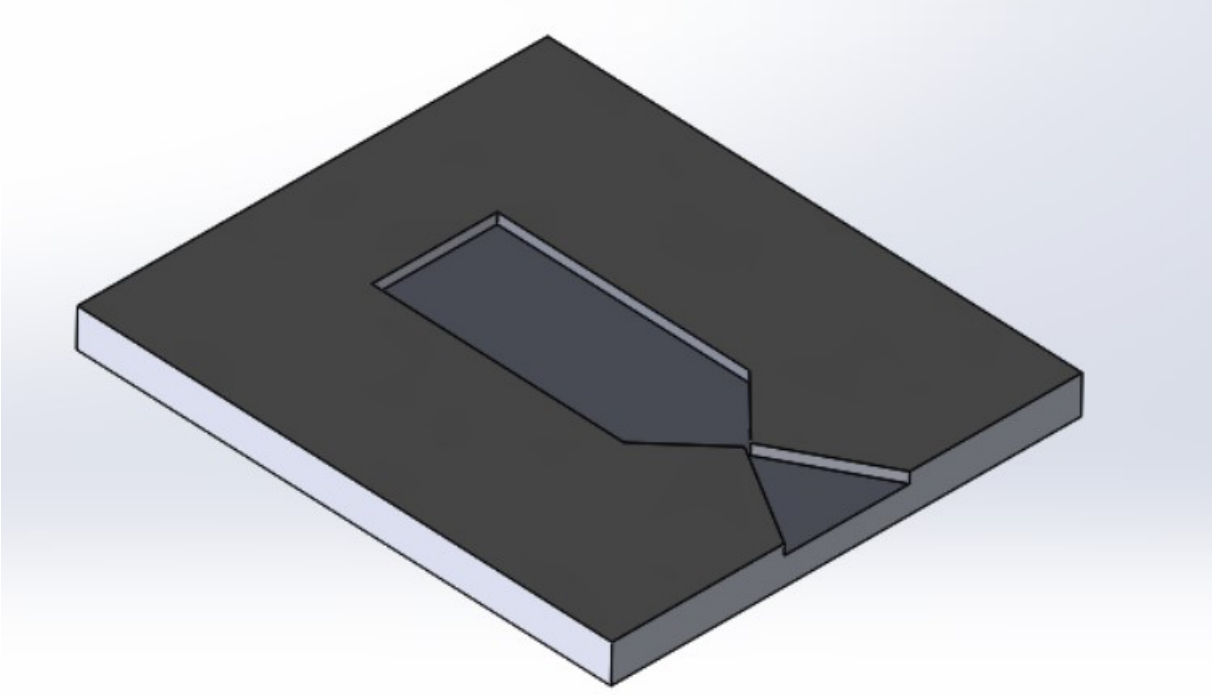

Figure 53: 3-D model of the wafer containing half chamber and half nozzle

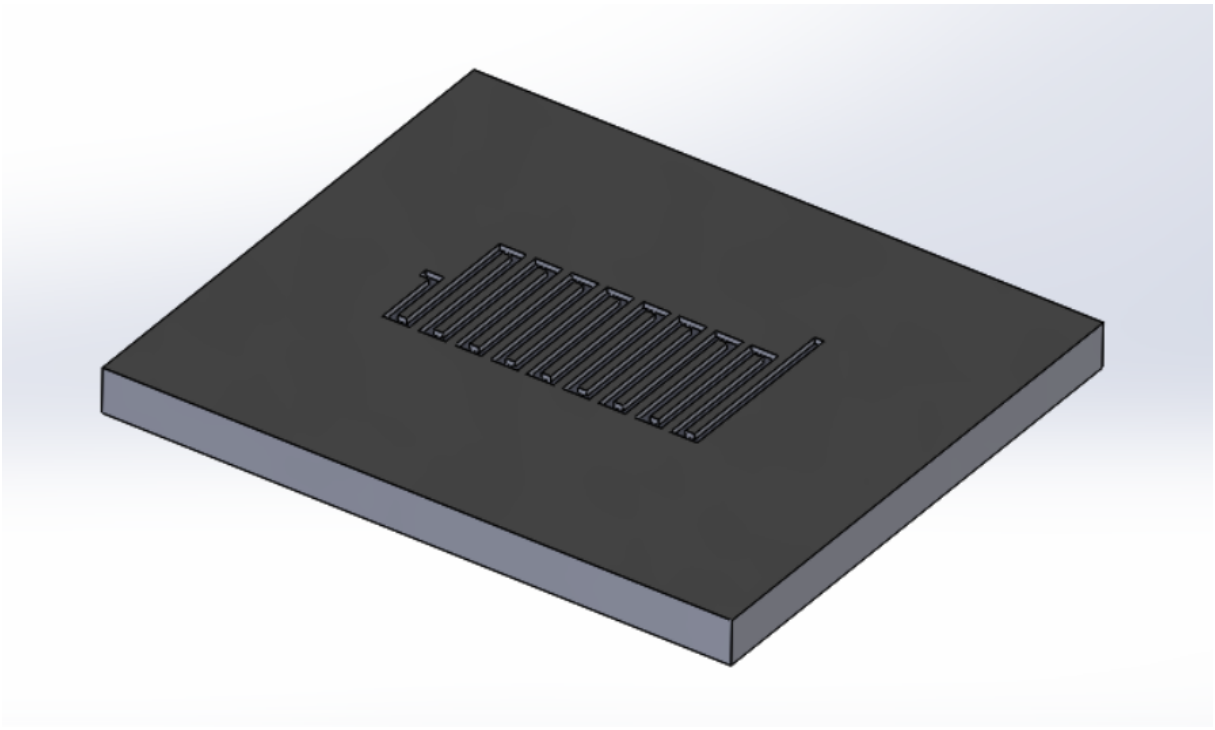

Figure 54: 3-D model of the wafer containing the cooling channel

The other two wafers are identical but specular.

In figure 55 and 56 are shown the technical drawings of the wafers above, with some dimensions (in mm) highlighted:

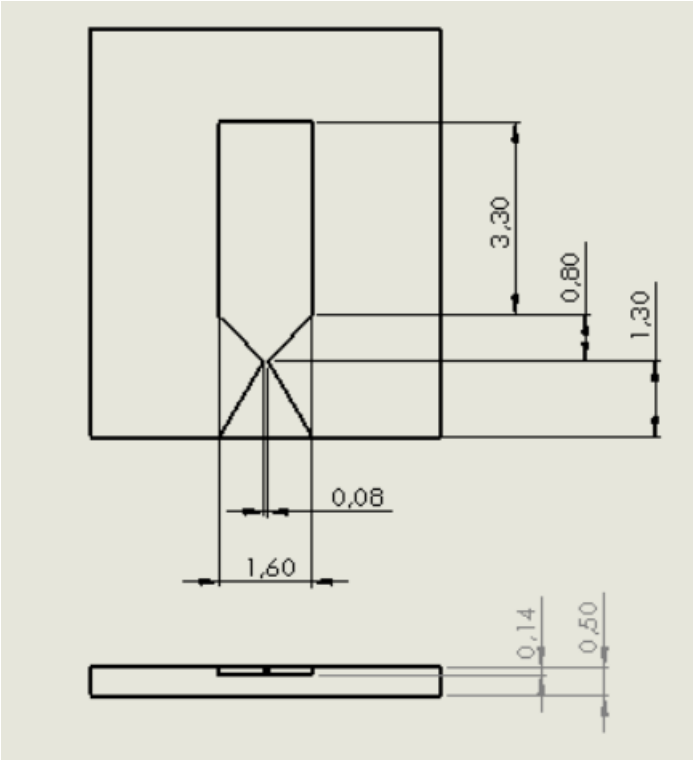

Figure 55: Technical design with dimension in mm of the wafer containing half chamber and half nozzle

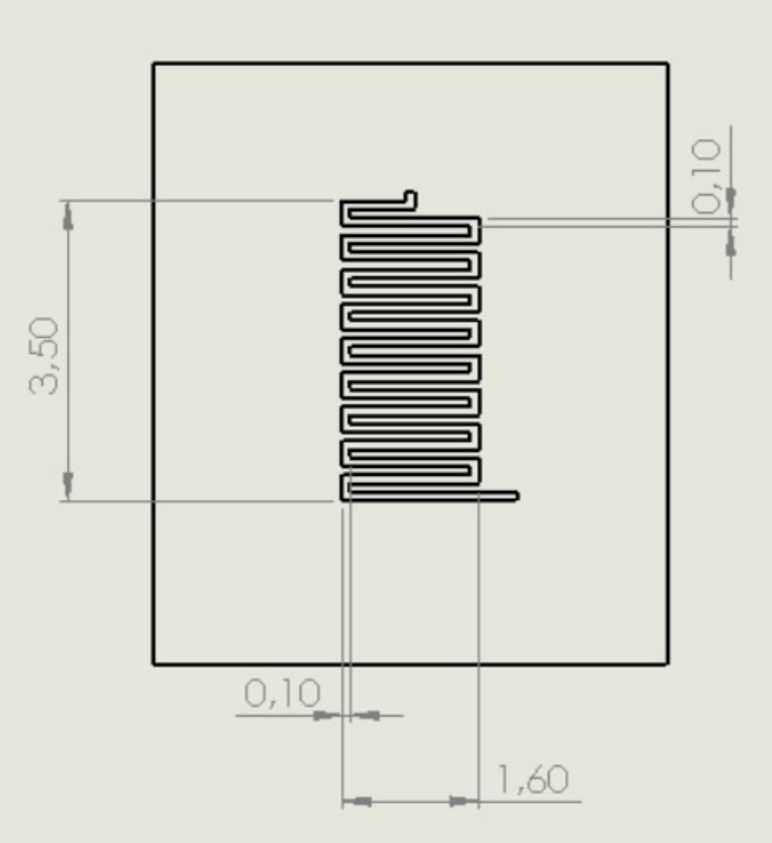

Figure 56: Technical design with dimensions in mm of the wafer containing the cooling channel

5.3 Conclusions and recommendations

The main goal of this work was to realize a preliminary design of a MEMS thruster operating with nitromethane as monopropellant. Before discussing the math and the choices made to achieve that, an overview on MEMS technology has been illustrated: in chapter 1 was presented what MEMS is, its advantages and disadvantages, the materials commonly used, and the routes of fabrications.
In chapter 2 were presented examples of MEMS devices like various actuators, sensors, and different thrusters to achieve thrust in space. The literature is full of examples of MEMS devices for the most various applications, not just space propulsion, but for obvious reasons we reported only few examples.
In chapter 3 were reported various tables with important propellant data for space applications. For this work, we created all the tables by doing research and calculations using the "NIST Chemistry WebBook" and a thermochemistry program called "CproPEP", which allowed us to derive important combustion parameters. In the same chapter was presented the propellant chosen for this work (i.e., nitromethane), the reasons behind the choice, and its properties.
Finally in chapter 4 were illustrated all the equations used in the MatLab script created to achieve the preliminary design. All the considerations and choices made are explained in the various sections of the chapter.
In the end, this work presented a MEMS thruster made of Silicon using nitromethane as monopropellant that should be able to deliver a 0.1 N thrust with a 25 bar operative pressure. The thruster is also equipped with a regenerative cooling system in order to maintain the walls of the system at an acceptable temperature. As is possible to see from subsection 5.1.3, the heat that spreads from the chamber is not completely absorbed by the coolant, leading to a potential flaw in the system. Two possible solutions for this flaw would be the designing of a new cooling channel configuration, and/or changing the material from Silicon to Silicon Nitride Si_3N_4 or Silicon Carbide SiC, due to their higher melting temperature. Resolving this problematic should be the main priority for future works.

This work is just the preliminary design, so it will need more studies, insights and improvements before the actual realization and fabrication.
Recommendations for future works are:

- Structural verifications through FEM software and CFD analyses.

- Investigate different layout and configurations for both the thruster and the cooling system.
- More accurate analysis of the heat exchanges in order to improve the regenerative cooling system.
- The manufacturing and testing of a prototype.

Bibliography

[1] Wolfson School of Mechanical and Manufacturing Engineering Loughborough University. *An introduction to MEMS*. 2002.

[2] Ioan Raicu. "MEMS Technology Overview and Limitations". In: (2004).

[3] Ying Jian Chen. "Advantages of MEMS and its Distinct New Applications". In: *Advanced Materials Research* 813 (2013), pp. 205–209.

[4] Mohamed Gad-el-Hak. *MEMS: Design and Fabrication.*

[5] W N Sharpe; Jr J J Hemker. "Mechanical Properties of MEMS materials". In: (2004).

[6] F Schneider; T Fellner; J Wilde; U Wallrabe. "Mechanical Properties of Silicones for MEMS". In: (2008).

[7] *Mechanical Properties of Monocrystalline Silicon.* URL: `https://www.universitywafer.com/mechanical-properties-monocrystalline-silicon.html`.

[8] Joel K. Kearns. "Silicon single crystals". In: ().

[9] Phillips S M; Heuer A H Yang J; Kahn H; He A Q. "A new technique for producing large-area as-deposited zero-stress LPCVD polysilicon films: the MultiPoly process". In: (2000).

[10] Hemker K J Jayaraman S Edwards R L. "Relating mechanical testing and microstructural features of polysilicon thin films". In: (1999).

[11] Vaidyanathan R Sharpe W N Yuan B. "Measurements of Young's modulus, Poisson's ratio, and tensile strenght of polysilicon". In: *Proc. Micro Electro Mechanical Systems Workshop, MEMS 97* (1997).

[12] Kahn H; Ballarini R; Mullen R L; Heuer A H. "Electrostatically actuated failure of microfabricated polysilicon fracture mechanics specimens". In: (1999).

[13] Zhang X; Ghodssi R; Chen K S; Ayon A A; Spearing S M. "Residual Stress Characterization of Thick PECVD TEOS Film for Power MEMS Applications". In: (2000).

[14] Petzow G; Hermann M. “Silicon Nitride Ceramics in High Performance Non-Oxide Ceramics”. In: (2002).

[15] Zorman C A; Roy S; Wu C H; Fleischman A J; Mehregany M. “Characterization of Polycrystalline Silicon Carbide Films Grown by Atmospheric Pressure Chemical Vapor Deposition on Polycrystalline Silicon”. In: *J. Mater. Res.* 13 (1996), pp. 406–412.

[16] Rajan W A. “Fabrication and Testing of Micromachined Silicon Carbide and Nickel Fuel Atomizers for Gas Turbine Engines”. In: *J. MEMS* 8 (1999), pp. 251–257.

[17] Schmidt M A; Howe R T; Senturia S D; Haritonidis J H. “Design and Calibration of a Microfabricated Floating-Element Shear$_S tressSensor$”. In: (1988).

[18] Chen L Y; MacDonald N. “A Selective CVD Tungsten Process for Micromotors”. In: *Technical Digest: 6th Int. Conf. on Solid-State Sensors and Actuators* (1991), pp. 739–742.

[19] K R Williams; R S Muller. “Etch rates for micromachining process”. In: *J. Microelectromech. Syst.* 5 (1996).

[20] Kurt E Peterson. “Silicon as a Mechanical Material”. In: *Proceedings of the ISEE* 70 (1982).

[21] Jack W Judy. “Microelectromechanical systems (MEMS): fabrication, design and applications”. In: (2001).

[22] Christina Leinenbach; Hannu Kattelus; Roy Knechtel. “Surface Micromachining”. In: (2010).

[23] Christine Harendt; Heinz-Gerd Graf; Bernd Hofflinger; Elisabeth Penteker. “Silicon fusion bonding and its characterization”. In: (1992).

[24] Yoshihiro Hirata. “LIGA process - micromachining technique using synchrotron radiation lithography - and some industrial applciations”. In: (2003).

[25] Bryzek J; Peterson K; McCulley W. “Micromachines on the March”. In: (1994), pp. 20–31.

[26] Udo Klotzbach; Andrés Fabian Lasagni; Michael Panzner; Volker Franke. “laser micromachining”. In: *Fabrication and Characterization in the Micro-Nano Range* (2011).

[27] N F de Rooij; S Gautsch; D Briand; C Marxer; G Mileti; W Noell; H Shea; U Staufer; B van der Shoot. In: (2009).

[28] W C Tang. “Micromechanical devices at JPL for space exploration”. In: (1988).

[29] A M De Aragon. "Space application for micro/nano-technolgies". In: *J Micromechanics and microengineering* 2 (1988).

[30] H Helvajiian; S Janson; E Y Robinson. "Big benefits from tiny technolgies: Micro-Nanotechnology applications in future space systems". In: *Advancement of Photonics for space* (1997).

[31] Nelismar Vandelli; Donald Wroblewski; Margo Velonis; Thomas Bifano. "Development of a MEMS Microvalve Array for Fluid Flow Control". In: *Journal of Microelectromechanical systems* (1998).

[32] T Bifano. "Micro-electro-mechanical actuators array for deformable mirrors". In: (1994).

[33] G Leal. "Laminar Flow and Convective Transport Processes". In: (1992).

[34] P Hosterberg; H Yie; X Cai; J White; S Senturia. "Self-consistent simulation of electrostatically deformed diaphragm". In: *IEEE Micro Electro Mechanical Systems Workshop* (1994).

[35] I Chakraborty; W C Tang; D P Bame; T K Tang. "MEMS micro-valve for space applications". In: (1999).

[36] J Mueller. "Thruster options for Microspacecraft: A Review and Evaluation of Existing Hardware and emerging Technologies". In: (1997).

[37] Donald Wroblewski; Thomas Bifano John Collier. "Development of a Rapid-Response Flow-Control System using MEMS Microvalve Array". In: (2004).

[38] K Srinivasa Rao; B Mohitha reddy; V Bala Teja; G V S Krishnateja; P Ashok Kumar; K S Ramesh. "Design and simulation of MEMS based capacitive pressure sensor for harsh environment". In: (2019).

[39] Y Zhang; R Howver; B Gogoi; N Yadzi. "A High-Sensitive Ultra-Thin MEMS Capacitive Pressure Sensor". In: (2011).

[40] Kyung Il Lee; M M Nayak; Hidekumi Takao; Kazuaki Sawada; Makoto Ishida; K Rajanna. "MEMS based High Dose Radiation Resistant SOI Pressure Sensor for Aerospace Applications". In: (2004).

[41] Xiaohao Wang; Zhaoying Zhou; Xiongying Ye; Yong Li; Wendong Zang. "A PZT-driven Micropump". In: (1996).

[42] B Pramanick; S Das; T K Bhattacharyya. "MEMS based normally closed silicon microregulator for gas and water". In: (2014).

[43] C Rossi; T Do Conto; D Estève; B Larangot. "Design, fabrication and modelling of MEMS-based microthrusters for space application". In: (2001).

[44] M Mihailovic; T V Mathew; J F Creemer; B T C Zandbergen; P M Sarro. "MEMS Silicon-based Resistojet Micro-Thruster for Attitude Control of Nano-satellite". In: (2011).

[45] Darren L Hitt; Charles M Zakrzwski; Michael A Thomas. "MEMS-based satellite micropropulsion via catalyzed hydrogen peroxide decomposition". In: (2001).

[46] Humble R Bettner M. "Polyethylene and hydrogen peroxide hybrid testing". In: (1998).

[47] Bayt R L; Ayon A A; Breuer K S. "A performance evaluation of MEMS-based micronozzles". In: (1997).

[48] *Thermophysical properties of fluid systems.* URL: `https://webbook.nist.gov/chemistry/fluid/`.

[49] Eric Boyer; Kenneth K Kuo. "Characteristic of Nitromethane for Propulsion Applications". In: (2006).

[50] J Lord Garcia. "Nitromethane". In: (2014).

[51] Federico Berto. "Preliminary Design of a Nitromethane Rocket Engine". In: (2021).

[52] Simon F; Glatzel G. "Bemurkungen zur Schmelzdruckkurve". In: (1929).

[53] Anon. "CH_3NO_2". In: *Physical and thermodynamic properties of pure chemicals: data compilation* (1997).

[54] Kee R J; Coltrin M E; Glarborg P. "Chemically reacting flow: theory and practice". In: (2003).

[55] Melius C F. "Thermochemical modeling: II. Applications to ignition and combustion of energetic materials". In: (1990).

[56] Kee R J; Rupley F M; Miller J A. "Chemkin-II: a Fortran chemical kinetics package for the analysis of gas-phase chemical kinetics". In: (1989).

[57] Kee R J. "A Fortran program for modeling steady laminar one-dimensional premixed flame". In: (1985).

[58] K K Kuo E Boyer. "High-Pressure Combustion Behavior of Nitromethane". In: (1999).

[59] Yetter R A; Dryer F L; Allen M T; Gatto J L. "Development of gas-phase reaction mechanism for nitramine combustion". In: (1995).

[60] Glarbog P; Bendtsen A B; Miller J A. "Nitromethane dissociation: implication for the CH_3 + NO_2 reaction". In: (1999).

[61] Zwicky F; Ewing F; Carter J M. "Operation of jet propulsion motors with nitroparaffins". In: (1948).

[62] Kindsvater H M; Kendall K K; Mueller K H; Datner P P. "Reseaerch on Nitromethane". In: (1951).

[63] Milton W E. "United State patent office". In: (1962).

[64] Carden M J. "Monopropellent assisted solid rocket engine". In: (2001).

[65] Wu M H; Wang Y; Yetter R A; Yang V. "Liquid monopropellent combustion in mesoscale vortex chamber". In: (2009).

[66] Daniel T Banuti; Martin Grabe; Klaus Hannemann. "Flow Characteristics of Micro-Scale Planar Nozzles". In: (2014).

[67] W F Louisos; A A Alexeenko; D L Hitt; A Zilic. "Design Considerations for Supersonic Micronozzles". In: (2008).

[68] C Melius. "Thermochemistry and Reaction Mechanism of Nitromethane Ignition". In: (1995).

[69] Taj Wali Khan; Ihtzaz Qamar. "Factors Affecting Characteristic Length of the Combustion Chamber of Liquid Propellant Rocket Engines". In: (2018).

[70] John C Chen. "A Correlation for Boiling Heat Transfer to Saturated Fluids in Convective Flow". In: (1962).